



저작자표시-비영리-변경금지 2.0 대한민국

이용자는 아래의 조건을 따르는 경우에 한하여 자유롭게

- 이 저작물을 복제, 배포, 전송, 전시, 공연 및 방송할 수 있습니다.

다음과 같은 조건을 따라야 합니다:



저작자표시. 귀하는 원저작자를 표시하여야 합니다.



비영리. 귀하는 이 저작물을 영리 목적으로 이용할 수 없습니다.



변경금지. 귀하는 이 저작물을 개작, 변형 또는 가공할 수 없습니다.

- 귀하는, 이 저작물의 재이용이나 배포의 경우, 이 저작물에 적용된 이용허락조건을 명확하게 나타내어야 합니다.
- 저작권자로부터 별도의 허가를 받으면 이러한 조건들은 적용되지 않습니다.

저작권법에 따른 이용자의 권리는 위의 내용에 의하여 영향을 받지 않습니다.

이것은 [이용허락규약\(Legal Code\)](#)을 이해하기 쉽게 요약한 것입니다.

[Disclaimer](#)

공학박사 학위논문

Strategies for High-Fidelity
Pin-Homogenized Two-Step
Core Calculation Based on
Systematic Error Analysis and
Leakage Correction

체계적 오차 분석과 누설 보정을 통한
고신뢰도 2단계 봉단위 노심 계산 전략

2021년 8월

서울대학교 대학원

에너지시스템공학부

홍 현 식

Abstract

The conventional two-step core calculation (TSCC) procedure employing the assembly-homogenized few group constants (GCs) has been widely used for commercial core design and analysis. Remarkably low computing cost is its undeniable advantage, but it is hard to incorporate actual core environment in the assemblywise few group cross sections (XSs) so that nontrivial errors in reactivity and power distributions are observed for highly heterogeneous core problems. In order to improve the accuracy with manageable computing cost, Yoon employed the multigroup (MG) pin-homogenized XSs (PHXSs) and the superhomogenization (SPH) factors to capture the errors which originate from the pin-cell homogenization and the coarse mesh (CM) finite difference method (FDM) solver combined with the diffusion theory. Following this, Cho combined the simplified P_3 (SP_3) theory with the FDM solver and demonstrated feasibility of the pinwise SP_3 core calculation.

The diffusion and SP_3 FDM solvers employed for the previous studies yielded satisfactory results for typical cores. However, notable increase of the errors was observed for specific cores, such as the GEN-III+ reactor cores and small cores loaded with mixed oxide (MOX) fuels. For this reason, the work aims to facilitate the high-fidelity pinwise TSCC by employing the optimal solution method through systematic analysis of the errors involved in the pin-homogenized MG calculation (PHMGC), and by applying a leakage correction to MG PHXSs.

The errors due to the use of PHXSs with the SPH factors based on single assembly (SA) configuration are investigated first for various core benchmark problems. It is to clarify the need for the SPH factors in TSCC and to reveal that the optimal solution method, which is a proper lower order approximation of the neutron transport equation (NTE) combined with an elaborated spatial discretization method, can effectively mitigate inconsistency of the SA based SPH factors in the core. It firstly reveals that the reaction rate error due to the loss of pin-cell internal geometry, namely the spatial homogenization error, predominates the errors of the PHXSs, and

it can be captured by the SPH factors. After that, the solution methods that are the simplified P_N (SP_N) and the discrete ordinate (S_N) method solvers with different degrees of the spatial discretization are examined. The results turn out that the diffusion calculations involve significant error cancellation which would result in seemingly good results; the SP_5 is not any better than SP_3 ; and S_N yields intolerable errors due to the inconsistency of SA based SPH factors especially noted in the fast energy range. Based on the results, the source expansion nodal method (SENM) solver of the SP_3 equation is selected as the optimal. For the KAIST 1A ARO core with sever local heterogeneity, the maximum (MAX) pin power error (ΔP) due to the SA based SPH factors are only about 1.1% for the 8G SP_3 SENM. It is far smaller than 4.6% and 8.5% errors of the 8G CM diffusion and SP_3 FDM.

The spectral error of the SA based MG PHXSs is then analyzed. It originates from the boundary spectral error due to the use of inconsistent boundary condition for the pin-cell homogenization and the group condensation error. The sensitivity analysis on the number of groups reveals that about 8 energy groups are required at least to reduce the root-mean-square (RMS) of the resulting pin ΔP less than 1.0%. However, the MAX pin ΔP can be still significant if the core is highly heterogeneous so that employment of the pinwise Leakage Feedback Method (LFM) is determined. The pinwise LFM functionalizes the PHXSs on leakage parameters in that the spectral error is determined by the leakage between neighboring nodes.

Accuracy of the SP_3 SENM and applicability the pinwise LFM are validated by TSCCs following the general procedure, with the PHXSs and the SPH factors based on SA configurations. The results are compared with reference solutions obtained from the nTRACER direct whole core calculation (DWCC). The code is also employed for the PHXS generations for the consistent code-to-code comparisons. The CM diffusion and SP_3 FDM results are yielded by SPHINCS, while the SENM results are yielded by VANGARD. The SP_3 SENM results agree well with the reference and those are remarkably improved by the pinwise LFM. In case of the KAIST 1A ARO core, for example, the reactivity ($\Delta\rho$) and MAX pin ΔP errors of the diffusion and SP_3 FDM are about 48 pcm and 11.4% and 74 pcm and 14.8% even

with the 8G PHXSs. However, the errors of the SP₃ SENM are 74 pcm and 7.3% and those are dropped to 9 pcm and 1.1% with the LFM. It is also noted that the error reductions are relatively smaller with the FDM solvers due to their inaccuracy. In case of the AP1000 PWR representing the GEN-III+ reactor cores, on the other hand, applicability of the LFM for various core states is also validated by the calculations up to the 3D hot-full-power core depletion, and practicality of the SP₃ SENM with LFM is estimated. For the partially rodded three-dimensional (3D) hot-zero-power core, the MAX 2D pin ΔP , and the computing times of the 8G calculations with 20 CPU cores are 1.7% and 66 seconds (s) for the diffusion FDM, 1.8% and 120 s for the SP₃ SENM, and 0.7% and 159 s for the SP₃ SENM plus LFM. The results show that the accurate core calculations require not too demanding cost. For the computing time, it should be noted that a previous study with VANGARD demonstrated more than 20 times speedup of the SP₃ SENM by the acceleration with a consumer grade GPU, due to inherent parallelism of the nodal kernel.

Through the study, it is shown that the SP₃ SENM solver with the pinwise LFM can accurately reproduce the heterogeneous reference, even though the SA based PHXSs and the SPH factors are used. The value of this work is that the TSCC results are not depending on the error cancellation so that the accuracy is less affected by the core heterogeneity, compared to the previous studies. The outcomes of the study are fully reflected to VANGARD so that the code is capable to perform the high-fidelity TSCC. Considering that the high-fidelity TSCC is getting more required due to advanced core designs and enforced safety regulations, this work can also provide a guideline for users and developers of the advanced TSCC codes.

Keyword: VANGARD, Simplified P_N, Source Expansion Nodal Method, Pin-by-pin core calculation, two-step core analysis, Leakage feedback correction

Student Number: 2015-22949

Contents

Abstract	i
Contents	iv
List of Figures	v
List of Tables	x
Chapter 1. Introduction	1
1.1. Purpose and Scope of the Research	5
1.2. nTRACER/VANGARD Code System	7
Chapter 2. Systematic Analysis of Errors in Pin-Homogenized Multigroup Core Calculation	9
2.1. Error Analysis Based on the Two-step Procedure.....	12
2.2. Errors due to Pin-Homogenized Multigroup Cross Sections.....	18
2.3. Errors due to Lower Order Solution Methods.....	28
2.3.1. Assessment of the transport error and the discretization error.....	38
2.3.2. Employment of the SENM for the SP_N equation	52
2.3.3. Inconsistency of the SPH Factors due to the Solution Methods	65
Chapter 3. Development of the Pinwise Leakage Feedback Method.....	72
3.1. Functionalization of PHXSs to Leakage Parameters	73
3.1.1. Three group LTRRs as the fitting parameters.....	75
3.1.2. Energy group definition for the intermediate range LTRR.....	79
3.1.3. Core calculation with the pinwise LFM.....	86
3.2. Considerations for the SPH Factors	89
3.3. Coefficient Generations for Branch Calculations	97
Chapter 4. Validation of the Solution Methods.....	102
4.1. KAIST 1A Benchmark.....	104
4.2. AP1000 PWR Initial Core.....	110
4.2.1. Results of the 2D HZP core calculations	114
4.2.2. Results of the 3D single assembly calculations	120
4.2.3. Results of the 3D mini-core calculations	129
4.2.4. Results of the 3D HZP and HFP core calculations	133
4.2.5. Results of the 3D HFP core depletions	140
4.3. APR1400 PWR Initial Core	143
Chapter 5. Summary and Conclusions.....	148
References.....	152
초 록	156

List of Figures

Figure 1.1. Schematic diagram of the PHXS generations employing the nTRACER GCGEN module and nTIG.....	8
Figure 1.2. Hierarchical data group structure of a GC file in HDF.....	8
Figure 2.1. Radial configuration of the modified KAIST 1A ARI core	10
Figure 2.2. Assembly loading patterns of the KAIST 1A benchmark.....	10
Figure 2.3. Configurations of the fuel-reflector local problems noted by EDGE (left), NOOK (center), and CORNER (right).....	11
Figure 2.4. Examples of the sub pin-cell discretization for a fuel (left), Gadolinia BP (center), and control rod inserted guide tube (right) pin-cell in MOC calculations.....	13
Figure 2.5. Burnable absorber loading patterns for an octant of the VERA FAs	14
Figure 2.6. Total reactivity error (pcm) obtained from the <i>SPN-8G-M</i> vs. <i>MOC-Het</i> comparisons for the VERA 2D fuel assemblies	15
Figure 2.7. Pinwise 1G absorption rate error (%) due to the four error sources in the <i>SP3-8G-1</i> result for the 2.918% 24BA assembly	16
Figure 2.8. G2 (top) and G7 (bottom) flux distributions of the 1D pin array obtained from the heterogeneous (black) and the pin-homogenized (red) MOC calculations.....	19
Figure 2.9. Radial pin power distribution of <i>MOC-Het</i> (left) and the relative pin power error (%) distributions of <i>MOC-47G</i> (right).....	20
Figure 2.10. Configuration of the KAIST 1A based 1D pin array	20
Figure 2.11. Pinwise 47G net current spectra for the 1D pin array	21
Figure 2.12. 47G nu-fission PHXS for a single UO ₂ pin-cell (black) and the relative difference (%) of the XSs obtained from the 1D pin array	21
Figure 2.13. Pinwise 47G flux spectra for the 1D pin array	22
Figure 2.14. Relative pin power error (%) distributions due to the total spectral error (top), group condensation error (middle), and boundary spectral error (bottom).....	26
Figure 2.15. Thermal range flux distributions of <i>MOC-2G</i> with the assembly-and pin-homogenized XSs (top) and <i>MOC-7G</i> with the PHXSs (bottom)	28
Figure 2.16. Iterative process for the generation of the SPH factors	29
Figure 2.17. Results of the 8G FDM calculations employing the core PHXS set	30
Figure 2.18. Radial core configuration (left) and the pin power distribution (right) of the C5G7 2D Rodded-B case.....	31
Figure 2.19. Comparison of the SP _N results without the SPH factors to <i>MOC-Het</i> for the C5G7 2D Rodded-B (Ref. k-eff: 0.963586)	34
Figure 2.20. Comparison of the SP _N results without the SPH factors to <i>MOC-7G</i> for the C5G7 2D Rodded-B (Ref. k-eff: 0.959933)	35
Figure 2.21. Comparison of the SP _N results with the SPH factors to <i>MOC-Het</i> for	

the C5G7 2D Rodded-B (Ref. k-eff: 0.963586).....	36
Figure 2.22. Relative pin power error (%) distributions originate from the transport error of the 8G FM calculations for KAIST 1A.....	40
Figure 2.23. Discretization errors obtained with various solution methods.....	41
Figure 2.24. Relative pin power error (%) distributions originate from the discretization error of the 8G SP ₃ FDM calculations for KAIST 1A..	43
Figure 2.25. G7 flux distributions obtained by different solvers	44
Figure 2.26. G7 flux distributions obtained by the SP ₃ (left) and the diffusion (right) solvers with different mesh sizes	44
Figure 2.27. G7 scalar flux (left) and net current (right) distributions obtained by the 2nd and 4th order diffusion NEM calculations	47
Figure 2.28. G7 scalar flux (left) and source (right) distributions obtained by the S ₂ calculations based on the short characteristics	49
Figure 2.29. Relative pin power error (%) distributions due to the two errors determined by selected solvers for the KAIST 1A ARO core calculations.....	51
Figure 2.30. G7 scalar flux and the 2nd angular moment distributions for the C5G7 1D pin array obtained from the SP ₃ FDM and SENM calculations	59
Figure 2.31. Relative difference (%) of the normalized core SPH factors to the SA SPH factors in G3 (top) and G8 (bottom) of the 8G for the KAIST 1A ARI core	67
Figure 2.32. Reactivity and the maximum pin power errors for the KAIST 1A ARO and ARI core calculations with the SA PHXSs and the various SPH factor sets.....	68
Figure 2.33. Radial pin power error (%) distributions for the KAIST 1A ARO and ARI core calculations with the SA PHXSs and the various SPH factor sets.....	69
Figure 2.34. Radial pin power error (%) distributions obtained with the core PHXSs and the SA SPH factors	70
Figure 3.1. 47G current spectrum for a UO ₂ fuel pin-cell.....	75
Figure 3.2. Fitting result for the G2 LTRRs of the 4G calculations obtained for a corner pin-cell of the APR1400 B2 FA with the 2G LTRRs	77
Figure 3.3. Fitting results for the G2 out scattering XS of the 4G obtained for a corner pin-cell of the APR1400 B2 FA with the 2G (left) and 3G (right) LTRRs	78
Figure 3.4. 2x2 CB configurations used to obtain the LFM coefficients for a target FA with a certain burnup exposure.....	80
Figure 3.5. The GOF obtained by fitting the 47G delta LTRRs with the 2G LTRRs for a corner pin-cell of the AP1000 Region 4 FA with 5GWD/tHM burnup	81
Figure 3.6. The RMS error obtained by fitting the 47G delta LTRRs with the 2G LTRRs for a corner pin-cell of the AP1000 Region 4FA with 5 GWD/tHM burnup	81
Figure 3.7. The 47G delta LTRRs obtained from the Sample 1 configurations for a	

corner pin-cell of the AP1000 Region 4 FA with 5 GWD/tHM burnup	82
Figure 3.8. The 47G delta LTRRs obtained from the Sample 2 configurations for a corner pin-cell of the AP1000 Region FA with 5 GWD/tHM burnup.	82
Figure 3.9. The U-235 and Pu-239 inventory changes for the corner pin-cells of the AP1000 PWR FAs during the depletion.....	83
Figure 3.10. Microscopic total XS of U-235 (red) and Pu-239 (blue) in the whole fast energy range higher than 0.625 eV cut-off.....	84
Figure 3.11. Fitting results based on the simple 3G for G3 nu-fission PHXS of the 4G obtained from a corner pin-cell of the AP1000 Region 4 FA	85
Figure 3.12. Fitting results based on the modified 3G for G3 nu-fission PHXS of the 4G obtained from a corner pin-cell of the AP1000 Region 4 FA ..	85
Figure 3.13. Sample CB configuration for a normal FA (left) and a rodged FA (right).....	87
Figure 3.14. Switching reflectors to assess the error of using a single reflector XS set	88
Figure 3.15. Iterative calculation scheme of the pinwise LFM.....	89
Figure 3.16. Radial pin power distribution of the 2x2 CB loaded with the AP1000 Region 2 and 4 FAs (Ref. k-eff: 1.01355)	91
Figure 3.17. Radial pin power error (%) distributions for the R2/R4 CB obtained from the 4G SP ₃ FDM calculations with different options	92
Figure 3.18. The GOF for the SPH corrected G3 removal and nu-fission PHXSs of the 4G obtained from the AP1000 Region 4 FA.....	93
Figure 3.19. Relative difference (%) between the CB and SA SPH factors obtained from the AP1000 Region 4 FA with the SP ₃ FDM solver	94
Figure 3.20. Radial pin power error (%) distributions for the R2/R4 CB obtained from the 4G SP ₃ SENM calculations with different options	96
Figure 3.21. Functionalization of the PHXS to the T/H and leakage effects	97
Figure 3.22. LFM coefficients of G1 (top) and G4 (bottom) diffusion coefficients for the 4G obtained from a corner pin-cell of the AP1000 Region 4 FA	100
Figure 3.23. LFM coefficients of G1 (top) and G4 (bottom) nu-fission PHXSs for the 4G obtained from a corner pin-cell of the AP1000 Region 4 FA	101
Figure 4.1. Error cancellation of the diffusion calculations for the KAIST 1A ARI	105
Figure 4.2. Consistent error reduction of the SP ₃ calculations for the KAIST 1A ARI.....	106
Figure 4.3. Pin power error (%) distributions for the KAIST 1A ARI core	107
Figure 4.4. Radial pin power error (%) distributions for the KAIST 1A ARO core obtained by different solvers without and with the pinwise LFM.....	109
Figure 4.5. Heterogeneous axial configurations of the AP1000 PWR initial core	111
Figure 4.6. Region 4 FA specification (left), core loading pattern (center), and the RCCA map (right) of the AP1000 PWR initial core	112
Figure 4.7. Relative pin power error (%) distributions for the AP1000 PWR 2D	

	HZP core due to the total spectral error (top), group condensation error (middle), and boundary spectral error (bottom)	113
Figure 4.8.	Radially averaged axial 1D power distributions of the AP1000 PWR assemblies at the HZP (left) and the HFP (right) states.....	113
Figure 4.9.	Radial pin power error (%) distributions for the AP1000 PWR 2D HZP ARO core obtained by different solvers.....	115
Figure 4.10.	Depletion results for the AP1000 Region 2 FA.....	117
Figure 4.11.	Depletion results of the AP1000 Region 4 FA	117
Figure 4.12.	The k-eff curve and the reactivity error (pcm) for the AP1000 PWR 2D HZP ARO core depletions obtained with the SP ₃ SENM solver.	118
Figure 4.13.	The MAX pin ΔP errors (%) for the AP1000 PWR 2D HZP ARO core depletions obtained with the SP ₃ SENM solver	118
Figure 4.14.	Radial pin power error (%) distributions for the AP1000 PWR 2D HZP ARO core depletions obtained with the SP ₃ SENM solver.....	119
Figure 4.15.	Axial 1D power and ΔP (%) distributions of the HZP Region 4 FA with the diffusion (top) and SP ₃ (bottom) FDM and SENM solvers.	121
Figure 4.16.	Effect of the axial reflector discontinuity factor on the axial ΔP error for the HZP Region 5A (top) and Region 5B (bottom) FAs	122
Figure 4.17.	Axial 1D power distributions at the different power levels	124
Figure 4.18.	Reactivity error (pcm) obtained from Region 3 (top) and 4 (bottom) FAs at different power levels with the three formulas.....	126
Figure 4.19.	Axial ΔP (%) obtained from Region 3 (top) and 4 (bottom) FAs at different power levels with NEA (left) and Studsvik (right) formulas	127
Figure 4.20.	Reactivity error (pcm) obtained with different Studsvik factors	128
Figure 4.21.	Radial configuration of the 3x3 mini-core.....	129
Figure 4.22.	Radial pin power error (%) distributions for the 3x3 HZP mini-core obtained by the SP ₃ SENM without (top) and with (bottom) the LFM	131
Figure 4.23.	Axial 1D power and ΔP (%) distributions obtained from the 3x3 HZP mini-core by the 4G SP ₃ SENM without (red) and with (blue) the LFM	131
Figure 4.24.	Axial 1D power and ΔP (%) distributions obtained from the 3x3 HFP mini-core by the 4G SP ₃ SENM without (red) and with (blue) the LFM	132
Figure 4.25.	Radial pin power error (%) distributions for the 3x3 HZP mini-core obtained by the SP ₃ SENM without (left) and with (right) the LFM	133
Figure 4.26.	Radial pin power error (%) distributions for the AP1000 PWR 3D HZP core with partially inserted AO bank	135
Figure 4.27.	Axial 1D power shape and ΔP error (%) distributions obtained by the 4G SP ₃ calculations for the AP1000 PWR 3D HZP core with partially inserted AO bank	135
Figure 4.28.	Radial pin power error (%) distributions for the AP1000 PWR 3D HFP rodged core with partially inserted AO bank.....	139

Figure 4.29. Axial 1D power shape and ΔP error (%) distributions obtained by the 4G SP ₃ calculations for the AP1000 PWR 3D HFP core with partially inserted AO bank.....	139
Figure 4.30. The CBC curve and the errors (ppm) for the AP1000 PWR 3D HFP ARO core depletions obtained with the SP ₃ SENM solver	140
Figure 4.31. The MAX pin ΔP errors (%) for the AP1000 PWR 3D HFP ARO core depletions obtained with the SP ₃ SENM solver	141
Figure 4.32. The MAX axial ΔP errors (%) for the AP1000 PWR 3D HFP ARO core depletions obtained with the SP ₃ SENM solver	141
Figure 4.33. Assembly (left) and core loading pattern (center) and the control element assembly (CEA) map (right) of the APR1400 PWR initial core	143
Figure 4.34. Relative pin power error (%) distributions for the APR1400 PWR 2D HZP core due to the total spectral error (top), group condensation error (middle), and boundary spectral error (bottom)	144
Figure 4.35. Radial pin power error (%) distributions for the APR1400 PWR 3D HZP ARO core obtained by the 4G SP ₁ SENM (left), SP ₃ SENM (center), and SP ₃ SENM + LFM (right) calculations	145
Figure 4.36. Radial pin power error (%) distributions for the APR1400 PWR 3D HZP ARO core obtained by the 4G SP ₁ SENM (left), SP ₃ SENM (center), and SP ₃ SENM + LFM (right) calculations	147

List of Tables

Table 2.1. Reactivity errors (pcm) due to the four error sources in <i>SPN-8G-M</i> results for the 2.619% 24BA assembly (Ref. k_{inf} : 0.925460)	16
Table 2.2. Spatial homogenization error of the KAIST 1A cores.....	19
Table 2.3. Energy group structures for the group condensation.....	25
Table 2.4. Dependence of the spectral error components on the number of energy groups for the KAIST 1A cores.....	26
Table 2.5. Summary of the C5G7 2D Rodded-B core calculation results (Ref. k_{eff} : 0.963586 for <i>MOC-Het</i> / 0.959933 for <i>MOC-7G</i>).....	33
Table 2.6. Transport errors obtained by the 4G FM calculations for KAIST 1A	39
Table 2.7. Transport errors obtained by the 8G FM calculations for KAIST 1A	39
Table 2.8. Discretization errors obtained by the 8G SP3 FDM and S8 DD calculations for KAIST 1A.....	42
Table 2.9. Results of the diffusion (SP ₁) and SP ₃ FDM calculations for the three-pin problem with the different mesh options (for G7).....	46
Table 2.10. Results of the 2nd and 4th order diffusion NEM calculations for the three-pin problem (for G7)	48
Table 2.11. Results of the S ₂ SC calculations for the three-pin problem with the different mesh options (for G7).....	50
Table 2.12. Total errors and contributions of the two error sources obtained from the 8G KAIST 1A ARO core calculations with the specific solvers ...	52
Table 2.13. Descriptions of the selected VERA 2D FAs	59
Table 2.14. Discretization error in the reactivity (pcm) obtained by the SP ₃ FDM and SENM calculations for the VERA 2D FAs.....	60
Table 2.15. Discretization error of the reactivity (pcm) obtained by the SP ₃ SENM calculations for the VERA 2D FAs with the different source expansion orders.....	61
Table 2.16. Relative difference (%) of the normalized core SPH factors to the SA SPH factors for each group of the 8G obtained from the KAIST 1A ARI core (<i>SA ONLY</i>)	66
Table 2.17. Results of the 8G KAIST ARO core calculations with the core PHXSs and the SA SPH factors	70
Table 3.1. Improvement of the fitting performance for out scattering XS obtained from a corner pin-cell of the APR1400 B2 FA.....	79
Table 3.2. Fitting results for G3 PHXSs of the 4G obtained from a corner pin-cell of the AP1000 Region 4 FA with 5 GWD/tHM burnup	86
Table 3.3. Results of the 4G SP ₃ FDM calculations for the R2/R4 CB.....	92
Table 3.4. Comparison of the 4G AA-SPHs obtained with the SP ₃ SENM solver for the AP1000 R2/R4 CB	95
Table 3.5. Results of the 4G SP ₃ SENM calculations for the R2/R4 CB	96
Table 3.6. The leakage and T/H condition applied to the target pin-cell.....	99

Table 3.7. Deviations of the 4G PHXSs due to the leakage, T/H, and cross effect obtained from a corner pin-cell of the APR1400 B2 FA	99
Table 4.1. Results of the KAIST 1A ARO core calculations (Ref. k-eff: 1.132102)	104
Table 4.2. Results of the KAIST 1A ARI core calculations (Ref. k-eff: 0.976441)	105
Table 4.3. Results of the KAIST 1A ARO core calculations without and with the pinwise LFM (Ref. k-eff: 1.132102)	108
Table 4.4. Fuel assembly specifications of the AP1000 PWR initial core	111
Table 4.5. Results of the AP1000 PWR 2D HZP ARO core calculations without and with the pinwise LFM (Ref. k-eff: 1.000014)	114
Table 4.6. Results of the AP1000 Region 4 3D HZP FA calculations	120
Table 4.7. Reactivity errors (pcm) obtained with different Studsvik factors	128
Table 4.8. Results of the 3x3 HZP mini-core calculations	130
Table 4.9. Results of the 3x3 HFP mini-core calculations	132
Table 4.10. Results for the AP1000 PWR 3D HZP core with partially inserted AO bank	134
Table 4.11. Computing time (sec) comparisons for the AP1000 PWR 3D HZP core with partially inserted AO bank.....	136
Table 4.12. ITC and boron worth (BW) of the AP1000 PWR 3D HZP ARO core	137
Table 4.13. Critical boron concentration of the AP1000 PWR 3D ARO core	137
Table 4.14. Results for the AP1000 PWR 3D HFP core with partially inserted AO bank	138
Table 4.15. Results of the AP1000 PWR 3D HFP ARO core depletions obtained with the SP ₃ SENM solver	142
Table 4.16. Results for the APR1400 PWR 3D HZP ARO core	145
Table 4.17. ITC and boron worth (BW) of the APR1400 PWR 3D HZP core.....	146
Table 4.18. Critical boron concentration of the APR1400 PWR 3D core	146
Table 4.19. Results for the APR1400 PWR 3D HFP ARO core	147

Chapter 1. Introduction

The conventional two-step core analysis systems such as CASMO/SIMULATE [1] [2] [3] of Studsvik, DeCART/MASTER [4] [5] of Korea Atomic Energy Research Institute (KAERI), and nTRACER/RENUS [6] [7] of Seoul National University (SNU) have been widely used for commercial core design and analysis. Since the two-step core calculation (TSCC) codes normally perform the diffusion calculations employing the assembly-homogenized few-group constants (few GCs) to obtain the three-dimensional (3D) core flux distributions and reconstruct the pin power using the pre-generated form functions, the computing costs is remarkably low. In spite of this undeniable advantage, however, the conventional TSCC yields nontrivial errors in the reactivity and the pin power distributions for highly heterogeneous problems [8], in that the few GCs hardly incorporate the actual core environment.

As a practical solution of the difficulty, advanced TSCC codes including SCOPE2 [9], DYN3D [10], and NECP-Bamboo2.0 [11] employ the multigroup (MG) pin-homogenized cross sections (PHXSs) to take account the pin-level heterogeneity while reducing the errors due to the group condensation. The pin-homogenized MG calculation (PHMGC) is normally carried out by nodal solvers based on the simplified P_N (SP_N) theory [12]. The solution methods are to faithfully represent the steep flux gradients and the neutron streaming effect which originate from severe local heterogeneity due to the pinwise geometry representation. The use of lower order solution method is feasible in that the pinwise equivalence factors (EFs) such as the discontinuity factor (DF) [13] [14] and the superhomogenization (SPH) factor [15] [16] correct the errors resulted from the lower order transport approximation and spatial discretization methods as well as the pin-cell homogenization. Compared to the direct whole core calculation (DWCC) which is getting more attention from research groups in the worldwide, the PHMGC requires notably less computing cost which is affordable for the industries. In this regard, the PHMGC fills the gap between the conventional TSCC and the DWCC.

The pinwise TSCC codes are also developed at Seoul National University Reactor

Physics Laboratory (SNURPL). In order to improve the accuracy while minimizing the increase of computing cost, Yoon [17] employed the finite difference method (FDM) solver of the diffusion equation taking each pin-cell as the base mesh and adopted the SPH factors to capture the errors associated with the diffusion theory and the coarse mesh size in addition to the pin-homogenization error. For various test problems ranging from small checkerboards (CBs) to commercial reactor cores, the pinwise diffusion FDM yielded notable improvement of the solution agreements. Following that, Cho [18] developed the SPHINCS (Simplified P₃ Pin-Homogenized Innovative Neutronics Core Simulator) code by combining the FDM solver with the SP₃ theory and demonstrated feasibility of the pinwise SP₃ core calculation.

The diffusion and SP₃ FDM solvers employed for the previous studies yielded accurate results for typical core problems. However, the agreements were notably degenerated for specific problems such as the GEN-III+ reactor cores with advanced heterogeneous designs and benchmark cores loaded with mixed oxide (MOX) fuels. Therefore, the errors in PHMGCs from various origins are systematically analyzed, and it is shown that the errors that originate from the single assembly (SA) based PHXSs and SPH factors for the core calculation are the key to the accuracy. It is also shown that the errors should be differently handled. For the inconsistency of the SA based SPH factors, a proper lower order approximation of the neutron transport equation (NTE) combined with an elaborated spatial discretization method, such as the source expansion nodal method (SENM) solver of the SP₃ equation [19], is needed. For the errors of the SA based MG PHXSs, on the other hand, employment of the sufficient number of energy groups or a leakage correction technique, such as the pinwise Leakage Feedback Method (LFM) [20], is required.

The thesis aims to present details of the error analysis and the pinwise LFM as follows. In **Chapter 2**, the analysis employing various core problems such as C5G7 [21], KAIST 1A [22], AP1000 PWR [23], and APR1400 PWR [24] is described. Note that the results for KAIST 1A are mainly discussed because it features the most highly heterogeneous core configuration including MOX fuel assemblies (FAs) and the findings from different cores are similar. In addition to the cores, small 1D arrays

loaded with the C5G7 or KAIST 1A pin-cells are also used as the supplement.

In this chapter, the errors due to the MG PHXSs are investigated first based on the general TSCC procedure. It aims to show that the reaction rate error due to the loss of pin-cell internal geometry, namely the spatial homogenization error, predominates the PHXS error and it can be corrected by the proper SPH factors. After that, the origin of the spectral error is detailed, and its significance is noted. It is shown that the spectral error is severe if the number of energy groups is insufficient and core configurations are highly heterogeneous. Based on the analysis, the need for using more energy group in PHMGCs is clarified and employment of the pinwise LFM, an extension of the original method [25] developed for the assemblywise few group core calculation, is determined.

The errors which originate from the lower order transport approximation and the spatial discretization methods, namely the transport error and the discretization error, are then examined. It is to find a solution method which can minimize the two errors as much as practically possible. In that the SPH factors correct the two errors which are sensitive to the core environment, the inconsistency of the SA based SPH factors can be decreased by a solver depending less on the SPH factors. The transport approximations include the highly rigorous discrete ordinate (S_N) method in addition to the diffusion and SP_N methods, considering the rapid growth of computing power in these days. Since the two errors simultaneously appears, different degrees of the spatial discretization methods are combined with the transport approximations. The results indicate that the SP_3 SENM is the optimal solution method.

Chapter 3 is dedicated for the pinwise LFM. By reflecting the fact that the spectral error is proportional to the leakage, the pinwise LFM employs three group (3G) leakage to removal ratios (LTRRs) for functionalization of PHXSs. The 3G LTRRs represent the fast, intermediate, and thermal energy ranges and independent of the actual number of groups used for the core calculation. Rationale of the 3G LTRRs, generation of the functionalization coefficients, considerations for the SPH factors, and application of the pinwise LFM for various core states up to the hot-full-power

(HFP) core depletion are detailed in this chapter.

In **Chapter 4**, numerical test calculations based on the general TSCC procedure are performed to validate the accuracy of SP₃ SENM and to observe the solution improvement by the pinwise LFM correction. The target problems are ranging from various 2D hot-zero-power (HZP) cores to 3D HFP core depletions. The diffusion and SP₃ solvers combined with FDM and SENM are employed for the comparison. Note that the formulas to determine the effective fuel temperature are also compared for the HFP calculations. The nTRACER code is employed to obtain not only the MG PHXSs but also the reference solutions, for the consistent code-to-code comparisons. The SPH factor generations and the pinwise core calculations are carried out by two codes, SPHINCS for the FDM and VANGARD [26] for the SENM. The results presented in this chapter are satisfactory. For example, the SP₃ SENM successfully reproduces the reference reaction rates with the SA based SPH factors, and the 4G core calculation results with the pinwise LFM are comparable to the 16G results. It is also noted that the additional computing cost for the use the SP₃ SENM instead of the diffusion and SP₃ FDM is not too demanding.

The value of this work is that the high-fidelity pinwise TSCC is facilitated by combining the SP₃ SENM solver, which is determined as the optimal solution method, with the pinwise LFM for the spectral leakage correction. Compared to the previous studies, the results based on the calculation strategy of this work are not depending on the error cancellation so that the good agreements are maintained for highly heterogeneous cores. The outcomes of the study are reflected to VANGARD so that the code is capable to perform the high-fidelity TSCC.

1.1. Purpose and Scope of the Research

Previous studies for the errors involved in PHMGC commonly focused on a specific part of the overall TSCC procedure. For example, Tatsumi [27] presented the effects of pin-cell homogenization using various PWR core configurations. The study showed significant errors especially due to Gadolinia (Gd) burnable poisons (BPs) and feasibility of PHMGC employing the pinwise SPH factors. Kozlowski [13] identified possible error sources which can deteriorate the TSCC results. However, the study is dedicated to extension of the cell discontinuity factor (CDF) method to the SP_3 calculations, and the target test problems are limited to SAs and 2x2 CBs. Thus the individual error sources are not analyzed in detail although the diffusion and SP_3 solvers are employed for the calculations with 2 and 7G PHXSs. Tada [28] performed the diffusion and SP_3 calculations with different sub pin-cell mesh discretization options for 2x2 CB problems consist of BWR FAs. The study shows applicability of the SPH factors for the SP_3 calculation as well as error cancellation associated with the transport approximation and the number of meshes per pin. Nonetheless, the target problems are still small, and the energy group effect is not considered. Compared to the studies which have own limits but the analyses themselves are rigorous performed, Litskevich [29] revealed lack of systematic approach. By comparing 2G diffusion, SP_3 , and S_N calculation results directly to the heterogeneous 47G references without a consideration for the cell homogenization technique and the mesh size, the authors arrived at a misled conclusion that the need for the SP_3 calculation over the diffusion is questionable.

Motivated by the previous studies, various error sources involved in PHMGC are systematically analyzed in Ref. [30] and in this work with more details by employing well-known, realistic, and notably difficult problems. These are to clarify the need for reduction of the spectral error from MG PHXSs by using a sufficient number of energy groups and a leakage correction, as well as a proper lower order solver to minimize the degree of correction for the transport and discretization errors which is introduced by the SPH factors. Each of the error sources represent the TSCC

procedure, therefore, the investigations of the spatial homogenization error and the spectral error are for the first step carried out by the lattice physics code, and those of the transport error and the discretization error are for the homogeneous core calculation with a specific solver. In order to keep the consistency of the analysis, the DWCC code nTRACER is employed for the reference calculations as well as the PHXS generations. The core calculations based on the given PHXSs are performed with VANGARD and SPHINCS codes.

As noted by Ban [25], however, other factors including the thermal hydraulic (T/H) effect and the simplified deletion chain also affect the core calculation results so that their impacts are examined. For the T/H effect, the pinwise TSCC codes employ the 1D simple T/H solver [18] which is also used in nTRACER so that non-uniformity of the pinwise moderator temperature distribution can be neglected. In contrast, the need for consideration of the intra-pellet fuel temperature distribution still remains so the NEA [31], CEA [32], and Studsvik [33] formulas are compared to select the Studsvik formula as the best option. The empirical weighting factor for the Studsvik formula, which is called *Studsvik factor*, is also determined as done by Hursin [34]. For the depletion chain, test calculations are performed in the lattice level to observe the reactivity error due to the increase of burnup exposure.

This work presents the SP_3 SENM solver as the optimal lower order solution method. It is based on the results of the error analysis employing the diffusion, higher order SP_N , and S_N solvers based on different sub pin-cell mesh discretization options. However, the pinwise SENM is essentially similar to nodal solvers described in previous studies, such as Beckert [35], so that this work does not pay much attention to the method itself. Instead, the pinwise LFM for further improvement of the solutions is mainly discussed. Compared to previous studies including Fujita [36] and Yu [37] where the target problems are limited to small CBs and HZP 2D cores, this work demonstrates applicability of the leakage correction for the practical core calculations. In this regard, the pinwise LFM is applied for various problems ranging from 2D HZP cores to 3D HFP core depletions.

1.2. nTRACER/VANGARD Code System

The nTRACER/VANGARD system is newly established for this work. In this system, the GCGEN (GC Generation) module of nTRACER specified for the PHXS generations is used. When a user runs the lattice depletion calculations with a fixed base condition, the nTRACER GCGEN module generates PGL (Pinwise GC Library) files in the ASCII format and nTIG (nTRACER Input Generator) [38] restart files at each depletion point. The nTIG restart files consist of GEO file which defines the explicitly modeled problem geometry and MAT file which contains isotopic mixture information for each flat-XS-region (FXR). By using the auxiliary code nTIG, the user can build the nTRACER input files for branch calculations at selected depletion points. The use of nTIG provides a clear advantage. Once the MAT and GEO files are obtained, the number of branch points and the branch conditions can be easily changed without an additional lattice depletion calculation. The procedure is outlined in **Figure 1.1** for one branch point. Note that the nTIG restart function is also used for CB calculations required for the LFM coefficient generations. It allows the use of various sample set by arranging GEO and MAT files.

In contrast to the nTRACER/SPHINCS system which reads PGL files directly, the PGL files are rearranged to HDF (Hierarchical Data Format) [39] file for the use in the nTRACER/VANGARD system. The LFM coefficient sets obtained by external MATLAB scripts are also included in the HDF GC file. The HDF GC file generations are carried out by a small auxiliary code REARGARD (Rearrangement PGL files for VANGARD) written in the C++ language. It would be worthwhile to note that revision of REARGARD is being carried out and the language is changed to the MATLAB and Python languages, in order to enhance user convenience. **Figure 1.2** shows an example of the hierarchical data group structure of a HDF GC file. All the data such as the pinwise burnup exposure, isotope inventory, branch types and conditions, and base and branched PHXSs are arranged in order. The advantage of using HDF GC is clear. It requires less storage and can be read remarkably faster. It is because HDF stores the data in binary and allows random access.

The pinwise SPH factor generations and the core calculations are carried out by a GPU-specific pinwise TSCC code VANGARD (Versatile Advanced Neutronics code for GPU-Accelerated Reactor Designs). Regarding the efficiency, VANGARD can perform the SPH iterations for all the depletion points and the branch points with a single input file. As a next generation pinwise code in SNURPL, VANGARD can perform the high-fidelity pinwise TSCC within the practical computing wall time. Although the VANGARD calculation results presented in the paper are obtained with CPU based solvers, because this work is also a preliminary part of the VANGARD development, the acceleration capability employing a General-Purpose Graphics Processing Unit (GPGPU) is already implemented and being tested currently. The GPU based solvers, which demonstrated more than 20 times speed up over the CPU solver [26], will be employed in follow up studies.

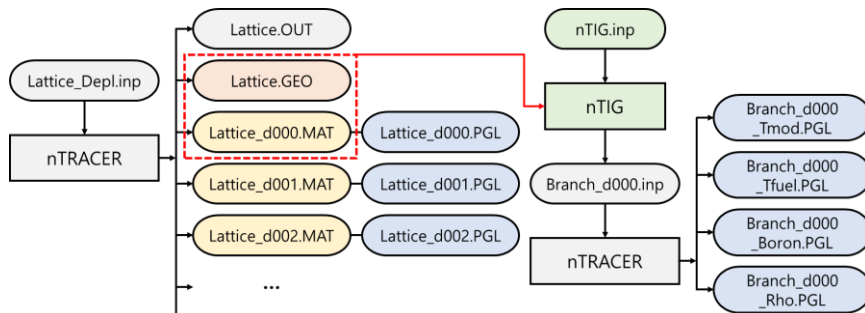


Figure 1.1. Schematic diagram of the PHXS generations employing the nTRACER GCGEN module and nTIG

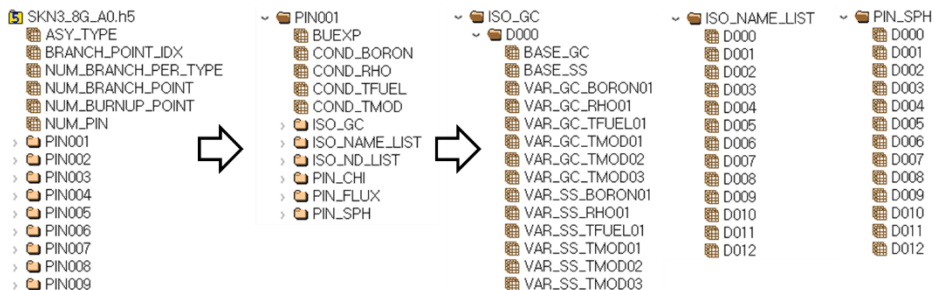


Figure 1.2. Hierarchical data group structure of a GC file in HDF

Chapter 2. Systematic Analysis of Errors in Pin-Homogenized Multigroup Core Calculation

The general procedure of the pinwise TSCC [40] is essentially the same as the well-established assemblywise TSCC [25]. The explicitly modeled lattice geometry is homogenized into 0D XSs and the fine energy groups are condensed into a specific MG, based on the solutions of the lattice calculation. Then the pin-homogenized core calculations are carried out by a lower order solver. The procedure provides a fundamental idea of the analyses that the entire errors can be separated into two parts, one due to the use of PHXSs and the other determined by a solver.

For systematic analysis of the errors, various core benchmark problems are employed. Selection of the target problem is based on their publicity, difficulty, and realism. The KAIST 1A benchmark, which is mainly discussed in this chapter, for example, the core includes MOX FAs as well as UO₂ FAs with and without Gd BPs and control rods (CRs). The MOX FAs feature very high thermal absorption, and the UO₂ and MOX FAs are arranged in CB shape. The significantly heterogeneous configuration renders the core quite appropriate to be employed for the analyses. Since the MG PHXSs and the corresponding SPH factors used for the PHMGCs are commonly obtained from SAs with all reflective BC, the associated errors can be clearly revealed in this kind of problems where the core and SA environments are remarkably different. In addition, the noticeably large local heterogeneity results in severe neutron streaming effect and thermal flux gradients which should be faithfully represented by a sufficiently high order solver. Note that the radial core configuration is presented in **Figure 2.1**, and the pin-cell loading patterns for one eighth of the 17x17 FAs are given in **Figure 2.2**. The vacuum BC at the core outer boundaries is replaced with the reflective BC for the convenience without essentially affecting the core flux profiles. The reactivity and pin power differences due to the changed BC are sufficiently small to neglect.

In this chapter, the nTRACER code is used for generations of the PHXSs as well as the heterogeneous reference solutions. Unless otherwise noted, the nTRACER flat

source MOC calculations are performed with the 47G transport corrected P_0 (TCP₀) XS library and the ray parameter set characterized by 0.01cm ray spacing and 32 azimuthal and 4 polar angles per octant sphere.

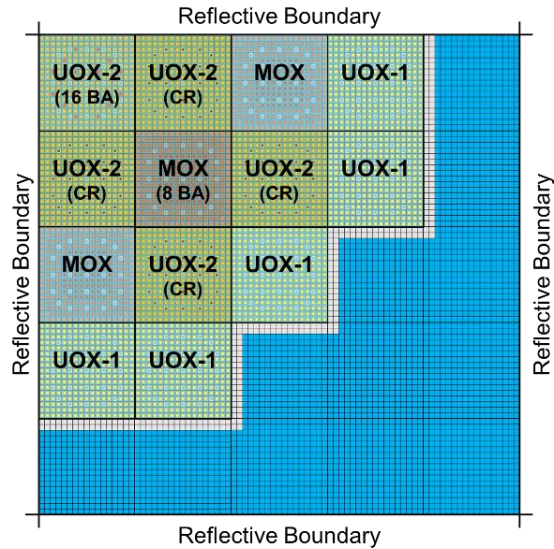


Figure 2.1. Radial configuration of the modified KAIST 1A ARI core

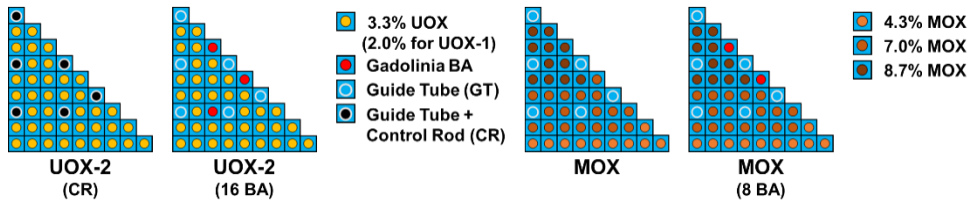


Figure 2.2. Assembly loading patterns of the KAIST 1A benchmark

Two sets of PHXSs, one from the DWCCs and the other from SA calculations, are generated. For each of the lower order solvers which are combinations of the SP_N and S_N transport approximations and various degrees of the spatial discretization methods, the SPH factors corresponding to the core and SA PHXSs are obtained by following the standard procedure. The calculation results based on the two sets are denoted by *core* and *SA*, respectively. The fuel-reflector geometry [20] shown in **Figure 2.3** are employed in addition to the SA configurations for FA to obtain the

PHXS and SPH factor sets for peripheral FA (PA) and reflectors. The reflective BC is applied to the outer boundaries of the local problems.

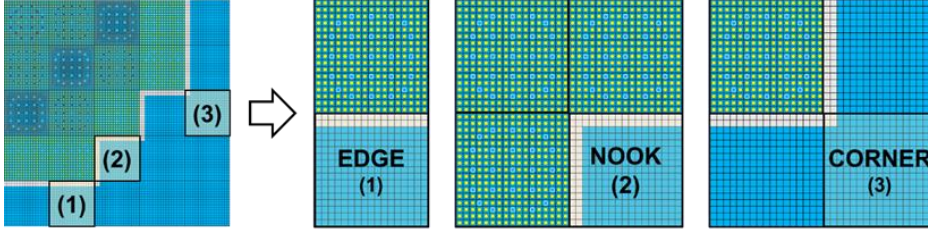


Figure 2.3. Configurations of the fuel-reflector local problems noted by EDGE (left), NOOK (center), and CORNER (right)

For the SP_N calculations, the SPH factors are directly multiplied to the even order angular moments as previously done by Tada [28] and Grundmann [41]. For the SN calculation with the SPH factors, the following simultaneous correction proposed by Chiba [42] are used:

$$\bar{\Omega} \cdot \nabla \phi_G^{(n)} + \frac{\Sigma_{tr,G}}{\mu_G} \phi_G^{(n)} = \frac{1}{4\pi} \left(\mu_G \Sigma_{GG} + \left(\frac{1}{\mu_G} - \mu_G \right) \Sigma_{tr,G} \right) \phi_G + Q_G, \quad (2.1)$$

where n is the discrete angle index and μ_G is the SPH factor in G -group.

The outline of this chapter is as follows. **Chapter 2.1** is to detail the error analyses strategy based on the general TSCC procedure. It also presents a review for the pinwise TSCC procedure and a preceding research for investigation of the errors using 2D FAs whose configurations are taken from VERA [43] HZP core problem. **Chapter 2.2** is to identify the origins of the spatial homogenization error and the spectral error. After showing the need for the SPH factors for PHMGCs, significance of the spectral error in terms of the pin power is quantified in this chapter by employing core based PHXSs and associated fluxes. **Chapter 2.3** is to examine the degree of the transport error and the discretization error determined by a specific solver. In this work, the discretization error is defined as the deviation of the coarse

mesh (CM) calculation result from the fine mesh (FM) reference based on the same transport approximation, therefore, the discretization error is depending on it. The chapter also presents the one-node SENM solver for the SP₃ equation as a practical substitute of very fine mesh FDM solver. After that, it is shown that the inconsistency of the SA based SPH factors in the core calculations is reduced by a proper solver, and the SP₃ SENM is selected as the optimal.

2.1. Error Analysis Based on the Two-step Procedure

The pinwise TSCC starts from the transport calculation for a heterogeneous lattice. Each of the pin-cells are explicitly modeled, as shown in **Figure 2.4**, in order to obtain the intra-pin level fine group flux distributions, and the fluxes are used as weighting functions to preserve the pinwise and groupwise reaction rates after the spatial homogenization. The pinwise reaction rate ($\tau_{i,g}$) can be written as:

$$\tau_{i,g} = \bar{\Sigma}_{i,g} \bar{\phi}_{i,g} V_i = \sum_{m \in i} \Sigma_{m,g} \phi_{m,g} V_m, \quad (2.2)$$

where i and m are the pin-cell and sub-pin region indices; g is the fine group index; V is volume; Σ is XS; ϕ is scalar flux; and the bar sign indicates the XS or flux is averaged over the pin-cell. By rearranging the equation, a fine group PHXS can be obtained as the follow:

$$\bar{\Sigma}_{i,g} = \frac{\tau_{i,g}}{\bar{\phi}_{i,g} V_i} = \frac{\sum_{m \in i} \Sigma_{m,g} \phi_{m,g} V_m}{\sum_{m \in i} \phi_{m,g} V_m}. \quad (2.3)$$

The neutron emission ($\bar{\nu}$) and the energy release ($\bar{\kappa}$) per fission are obtained by dividing the pin-homogenized nu-fission ($\nu \bar{\Sigma}_{f,i,g}$) and kappa-fission ($\kappa \bar{\Sigma}_{f,i,g}$) XSs with fission XS ($\bar{\Sigma}_{f,i,g}$). The fission spectrum is obtained as Eq. (2.4), by using the

intra-pin level fission source distribution as the weighting functions:

$$\bar{\chi}_{i,g} = \frac{\sum_{m \in i} \chi_{m,g} \psi_m}{\bar{\psi}_{i,g}} = \frac{\sum_{m \in i} \chi_{m,g} \sum_{g'} \nu \Sigma_{f,m,g} \phi_{m,g'} V_m}{\sum_{m \in i} \sum_{g'} \nu \Sigma_{f,m,g} \phi_{m,g'} V_m}. \quad (2.4)$$

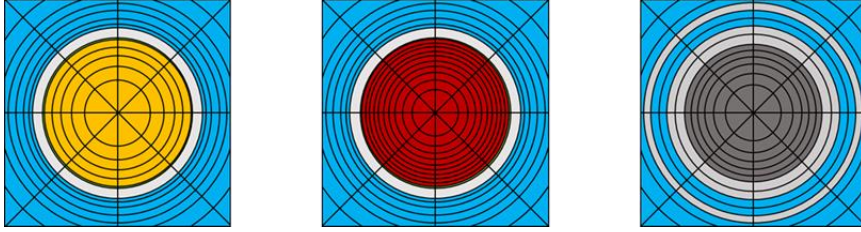


Figure 2.4. Examples of the sub pin-cell discretization for a fuel (left), Gadolinia BP (center), and control rod inserted guide tube (right) pin-cell in MOC calculations

The group condensation is performed with the fine group PHXSs and associated fluxes. It should be noted that the diffusion coefficient itself, which is the inverse of transport XS divided by 3 [44], is condensed like other XSs. The MG PHXSs and fluxes are also used to generate the SPH factors, which are to take account the effect of pin-cell homogenization. The pin-homogenized core calculation is then performed by employing the MG PHXSs and the SPH factors.

For a single FA problem, the total error yielded by a lower order solver without the aid of an equivalence factor can be separated into four elements, namely spatial homogenization error, group condensation error, lower order transport error, and spatial discretization error. Based on the fact that the spatial homogenization error and the group condensation error are determined by given PHXSs and the transport error and the discretization error are added by the solver, the preceding study [45] quantified the four error sources employing 2D FAs presented in **Figure 2.5**. The FA specifications were taken from the VERA HZP core, but the assembly gap is omitted for convenience. The enrichment of UO₂ fuels is the uniform 2.11%, 2.619%, and 3.10%, and only the number of Pyrex burnable absorber (BA) is changed. In that the degree of the heterogeneity is directly determined by the number of BA, the problem

is quite adequate for the test calculations.

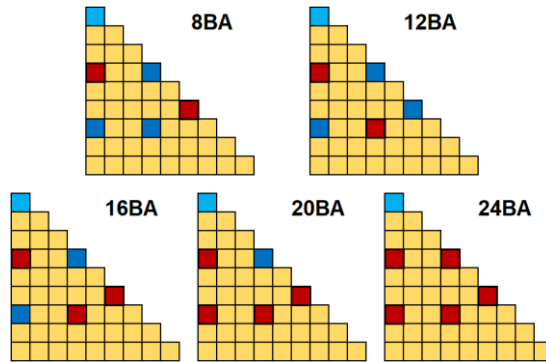


Figure 2.5. Burnable absorber loading patterns for an octant of the VERA FAs

The quantifications were performed by the following steps based on the general pinwise TSCC procedure: (1) the pin-homogenized 47G MOC result (*MOC-47G*) vs. the heterogeneous 47G MOC reference (*MOC-Het*) comparison for the spatial homogenization effect; (2) the *X*-group pin-homogenized MOC result (*MOC-XG*) vs. *MOC-47G* for the group-condensation effect; (3) the *X*-group SP_N FM FDM result (*SPN-XG-FM*) vs. *MOC-XG* for the transport effect; and (4) the *X*-group SP_N FDM result based on *M*-by-*M* mesh per pin (*SPN-XG-M*) vs. *SPN-XG-FM* for the spatial discretization effect. The TCP_0 MOC calculations were carried out by nTRACER, with tight ray parameters as aforesaid. Each pin-cell was divided into 32x32 meshes for *MOC-XG* and *SPN-XG-FM*, in order to sufficiently reduce the discretization effect. Note that the diffusion theory solvers and corresponding calculation results are denoted by SP_1 in figures and tables for convenience.

The results show that there exists error cancellation between the transport error and the discretization error. The reactivity error ($\Delta\rho$) of the 8G diffusion and SP_3 FDM calculations based on 1x1 and 2x2 meshes per pin are the example. It shown in **Figure 2.6**. Thus the references were obtained by the *MOC-Het* calculations, the $\Delta\rho$ errors are the total errors in which all the error sources are combined. It is undeniable that the SP_3 theory is more accurate than the diffusion in representation of the neutron streaming effect and the smaller mesh size guarantees less spatial discretization error in that the steep flux gradients in the pinwise geometry can be

faithfully represented. However, as noted in **Figure 2.6**, the *SP1-8G-1* results are apparently better than the *SP1-8G-2* and *SP3-8G-1* results, and for most of the BA inserted FAs, those are even better than *SP3-8G-2*.

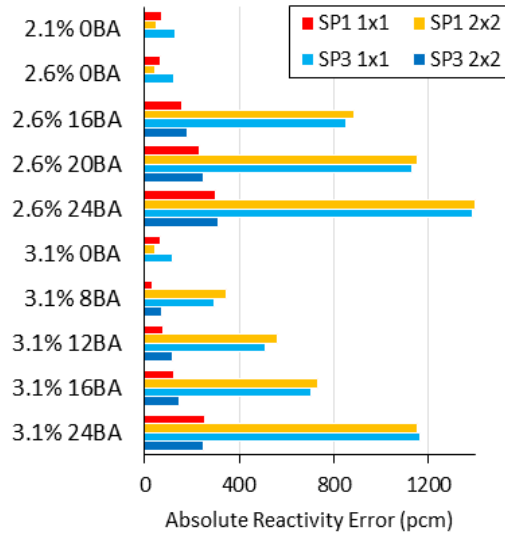


Figure 2.6. Total reactivity error (pcm) obtained from the *SPN-8G-M* vs. *MOC-Het* comparisons for the VERA 2D fuel assemblies

The error cancellation can be investigated more in detail. **Table 2.1** presents the $\Delta\rho$ errors yielded by *SPN-8G-M* vs. *MOC-Het* comparisons for the 2.619% 24BA FA with $N = 1$ and 3 and $M = 1$ and 2 . Since the same PHXSs are used, the spatial homogenization (*Hom.*) and the group condensation (*Con.*) errors are identical. The group condensation error appears even in this SA case in that the pinwise leakage obtained with the PHXSs is different to the heterogeneous reference.

In **Table 2.1**, it is clearly shown that the agreement of *SP1-8G-1* is resulted by the error cancellation. The diffusion solver severely underestimates the reactivity due to the transport error (*Tran.*), but the remarkable large discretization error (*Disc.*) in the positive direction cancels out the transport error as well as the homogenization error. However, the *SP3-8G-2* presents remarkable error reductions. The transport error is decreased about 900 pcm by employing the SP_3 theory and the spatial discretization

error is decreased about 1700 pcm by halving the mesh size.

Table 2.1. Reactivity errors (pcm) due to the four error sources in SPN-8G-M results for the 2.619% 24BA assembly (Ref. k-inf: 0.925460)

Source	Specification	SP1		SP3	
		1x1	2x2	1x1	2x2
Hom.	MOC-47G vs. MOC-Het	-708			
Con.	MOC-8G vs. MOC-47G	34.8			
Tran.	SPN-8G-FM vs. MOC-8G	-1529.6		-595.3	
Disc.	SPN-8G-M vs. SPN-8G-FM	2505.7	806	2654.7	956.8
Sum of the errors		302.9	-1396.8	1386.2	-311.8
(vs. total error)		(0.0)	(0.0)	(0.0)	(0.0)

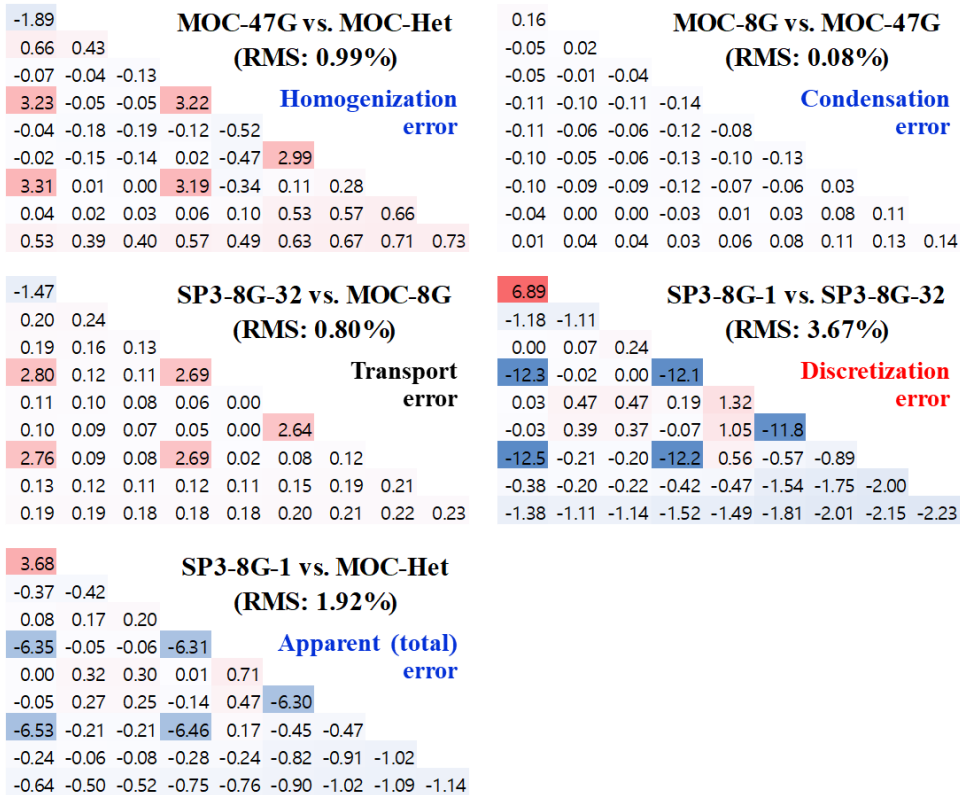


Figure 2.7. Pinwise 1G absorption rate error (%) due to the four error sources in the SP3-8G-1 result for the 2.918% 24BA assembly

The error cancellation is also observed from the pinwise reaction rate errors. The results presented in **Figure 2.7** are the errors of the 1G absorption rate normalized to unit fission source. In that the errors are relative values to the reference reaction rate obtained from the *MOC-Het*, the total error is a summation of each error. For example, -1.14% of the total reaction rate error for a corner pin-cell is the sum of 0.73% of the homogenization error, 0.14% of the condensation error, 0.23% of the transport error, and -2.23% of the discretization error.

The study provides a motivation for this work. It shows that the error sources can be identified by following the TSCC procedure and their contributions to the total error can be quantified. It also clarifies that the additional correction is to be introduced by the SPH factors for the transport error and the discretization error, and the degree of this correction can be estimated by comparing the lower order result to the pin-homogenized reference solution without using the SPH factors.

Therefore, the analyses performed in this work is essentially similar with the study, but five major changes are made. First of all, scale of the target problem is increased to a core size for the realism. Secondly, the group condensation error is not obtained by merely comparing *MOC-XG* with *MOC-47G* anymore. It is because the group condensation error within assembly is captured by the SPH factors in PHMGC and the spectral errors due to the inter-assembly leakage effect appears in the core calculations. Instead, the spectral error and its dependence to the number of energy groups are investigated and it leads to development of the pinwise LFM. Thirdly, in order to extend the range of the analysis, more elaborated transport approximations including the higher order SP_N and the S_N methods and the spatial discretization methods are examined. Fourthly, the origin of the error cancellation is investigated by employing small pin array problems. Lastly, the errors due to the inconsistency of the SA based SPH factors in the core calculation is investigated.

2.2. Errors due to Pin-Homogenized Multigroup Cross Sections

In order to show the origin of the spatial homogenization error, **Figure 2.8** presents the 1D pin array consisting of the C5G7 pin-cells and the flux distributions of Group 2 (G2) and G7 for heterogeneous and homogeneous configurations. G2 and G7 are the groups where the flux levels are highest in the fast and thermal ranges. The MOC solution for the heterogeneous problem, which is in fact a 2D problem with circular pellet regions, is obtained first and it is used to generate PHXSs for the homogenized problem. The 7G structure is retained in the homogenized problems for which the same MOC solver is used with 32 flat source regions per pin cell. In order to obtain the 1D averaged flux distribution from the 2D heterogeneous solution, the intra-pin flux shape was approximated in terms of a quartic polynomial as:

$$\phi_G(u) = \bar{\phi}_G + \alpha_{G,1}P_1(u) + \alpha_{G,2}P_2(u) + \alpha_{G,3}P_3(u) + \alpha_{G,4}P_4(u), \quad (2.5)$$

$$J_G(u) = -\frac{2D_G}{h} \frac{d\phi_G(u)}{du}, \quad (2.6)$$

where P_N is the N -th Legendre polynomial; G is the group index; D_G is the pinwise diffusion coefficient; h is the pin pitch. In order to determine the four coefficients, the constraints on surface-averaged fluxes and net currents at the pin left (L) and right (R) surfaces are imposed as follow:

$$\phi_G(-1) = \phi_G^L, \quad \phi_G(1) = \phi_G^R, \quad J_G(-1) = J_G^L, \quad \text{and} \quad J_G(1) = J_G^R, \quad (2.7)$$

The difference between the red (homogenized) and black (heterogeneous) lines is caused only by the pin-homogenization, and it is quite large in G7. For a fuel pin-cell, for example, the black line in G7 is notably low at the pin-cell center due to the large XS of the fuel and high at the left and right surfaces. On the other hand, the red line which is not affected by the intra-pin level heterogeneity is much smoother. It is also seen that the two flux distributions are quite different at the UO₂/MOX interface, and the G7 fluxes of the homogenized model are underestimated in the guide tubes (GTs). The resulting spatial homogenization error is 343 pcm for $\Delta\rho$ and 0.8% for

the root-mean-square (RMS) error in pin power. The maximum (MAX) pin power error (ΔP) that occurs at the UO_2 /MOX interface is 1.7%.

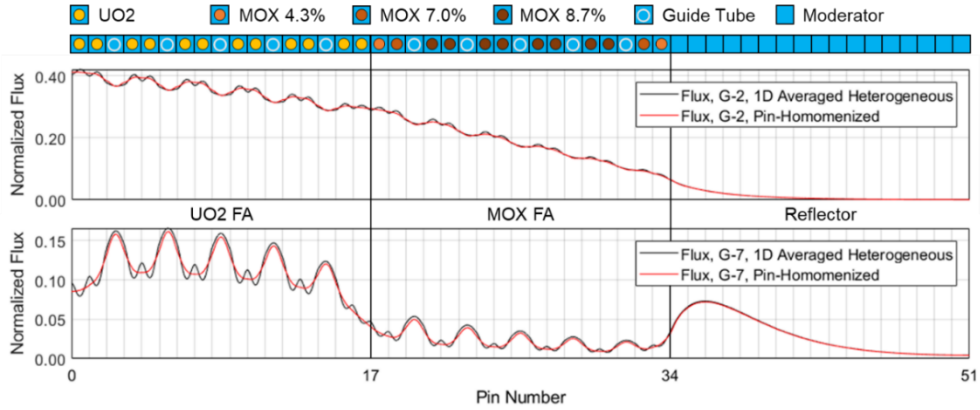


Figure 2.8. G2 (top) and G7 (bottom) flux distributions of the 1D pin array obtained from the heterogeneous (black) and the pin-homogenized (red) MOC calculations

In order to examine the spatial homogenization error in core calculations, the 47G pin-homogenized MOC results (*MOC-47G*) were obtained for the KAIST 1A cores. The error of *MOC-47G* to the 47G heterogeneous MOC reference solution (*MOC-Het*) in terms of the $\Delta\rho$ and the RMS/MAX pin ΔP are given in **Table 2.2**. For *MOC-47G*, only the core PHXSs were used without the SPH factors. The radial pin power and the relative (Rel.) pin ΔP distributions are shown in **Figure 2.9**. It is clearly noted that the spatial homogenization error is quite large. The RMS and MAX absolute (Abs.) pin ΔP are 6.3 % and 18.2% for the ARI case, and those are not tolerable for the All-Rods-Out (ARO) case either. Although this error can be mitigated by the use of proper EFs such as the SPH factors, it should be noted that this much large error is caused solely by the geometry loss.

Table 2.2. Spatial homogenization error of the KAIST 1A cores

State	k-eff	$\Delta\rho$ (pcm)	Absolute Pin ΔP (%)		Relative Pin ΔP (%)	
			RMS	MAX	RMS	MAX
ARO	1.130070	-160.4	2.13	10.12	1.85	7.74
ARI	0.969743	-714.3	6.25	18.15	5.64	12.61

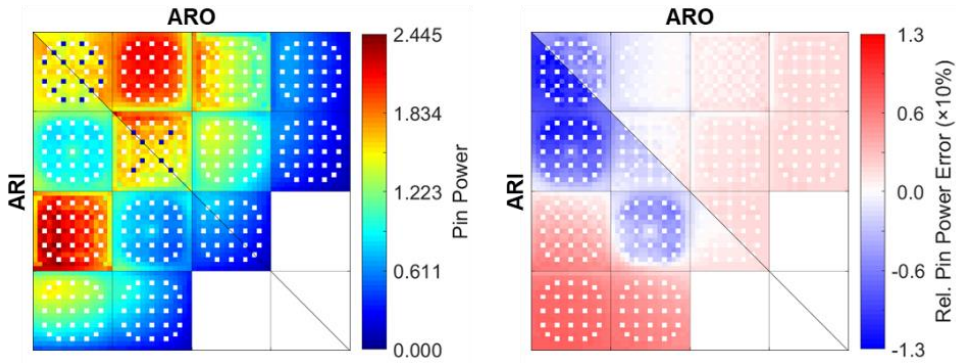


Figure 2.9. Radial pin power distribution of *MOC-Het* (left) and the relative pin power error (%) distributions of *MOC-47G* (right)

In the core calculation, the spectral error is additionally appearing because the SA SPH factors cannot correct the error introduced by neighboring nodes. The spectral error originates from two sources. One is the assembly BC employed for the PHXS generations is inconsistent to the core environment, and the other is the flux spectrum used for the group condensation is different to the core based flux spectrum. In order to clarify the two errors, the 47G heterogeneous MOC calculations were performed for a KAIST 1A based 1D pin array detailed in **Figure 2.10**, and the 47G spectra of pin-averaged fluxes and net currents and nu-fission PHXSs were obtained for each fuel pin. The spectra are normalized to yield unit fission source for each pin.

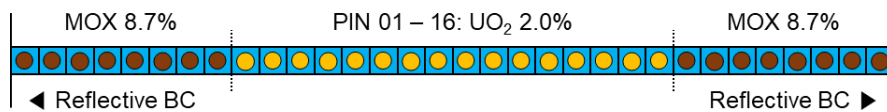


Figure 2.10. Configuration of the KAIST 1A based 1D pin array

The pinwise net current spectra are shown in **Figure 2.11**. The net currents are obtained at the left hand surface of each pin-cell. For Pin 01 which is the UO₂ pin neighboring the MOX pins, the remarkably large incoming and outgoing currents are formed at the fast and thermal energy ranges, while Pin 08 shows the negligibly small currents. It is obvious that the intra-pin flux distributions are perturbed by the

currents so that the resulting PHXSs are changed, and the effect would decrease as the distance between the pin-cell and the assembly boundary increases.

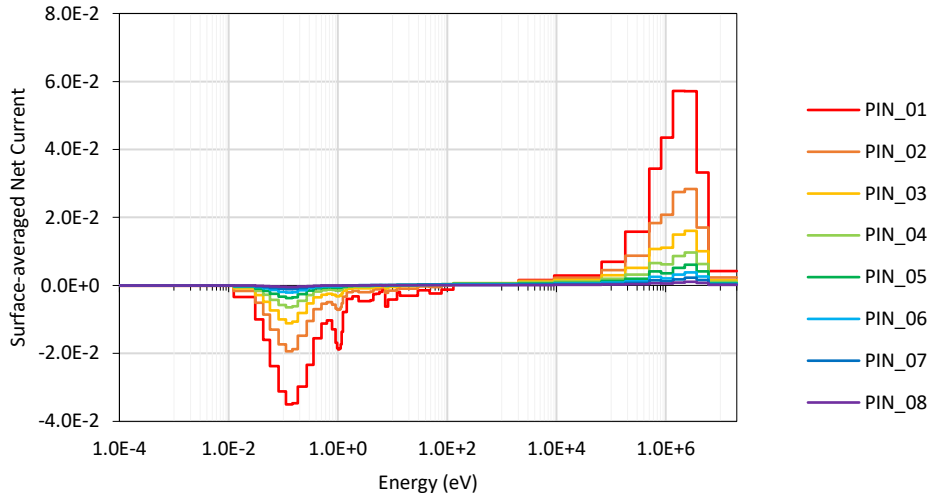


Figure 2.11. Pinwise 47G net current spectra for the 1D pin array

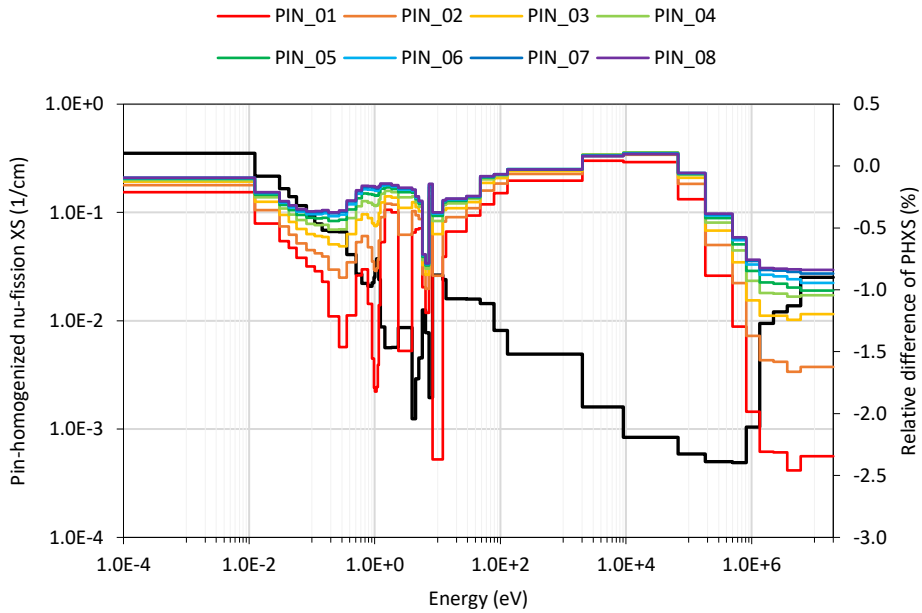


Figure 2.12. 47G nu-fission PHXS for a single UO₂ pin-cell (black) and the relative

difference (%) of the XSs obtained from the 1D pin array

As the example, **Figure 2.12** presents the reference 47G nu-fission PHXSs and the relative differences to the reference obtained from each pin-cell. The reference 47G PHXSs are for a pin-cell with no leakage. It is clearly noted that the 47G PHXSs of the pin array is significantly underestimated in the fast and thermal ranges because the flux level in the moderator is increased by the current. This PHXS deviation is defined as the boundary spectral effect in this work. The results indicate the boundary spectral error would be notable mostly at the assembly peripheral pin-cells.

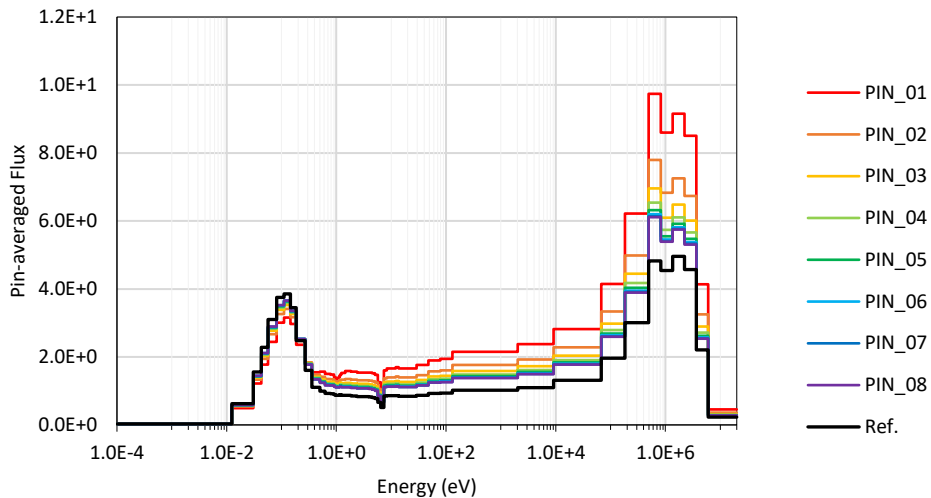


Figure 2.13. Pinwise 47G flux spectra for the 1D pin array

The surface currents change the flux spectra as well, as shown in **Figure 2.13**. The reference UO_2 spectrum is for a single pin-cell which would reveal the asymptotic spectrum determined with no leakage. For Pin 01, the flux spectrum is quite different from the reference due to the significantly large current formed by the neighboring MOX pin. As the net current decreases as the distance from the UO_2/MOX interface increases, the pinwise flux spectrum asymptotically approaches to the reference. The difference of the flux spectrum is the origin of the group condensation error which

actually appears in PHMGCs. The analysis indicate that the group condensation error would depend on the distance from the assembly boundary, as well as the number of energy groups and the condensed group structures.

Significance of the two errors in the core calculation results can be estimated by using the core PHXSs and associated fluxes in addition to the corresponding SA based PHXSs. Consider the standard flux-volume weighted averaging process based on the heterogeneous core calculation result as:

$$\bar{\Sigma}_{G,i}^{Core} = \frac{\sum_{g \in G} \sum_{m \in i} \Sigma_{g,m} \phi_{g,m}^{Core} V_m}{\sum_{g \in G} \sum_{m \in i} \phi_{g,m}^{Core} V_m} = \frac{\sum_{g \in G} \bar{\Sigma}_{g,i}^{Core} \bar{\phi}_{g,i}^{Core}}{\sum_{g \in G} \bar{\phi}_{g,i}^{Core}} = \sum_{g \in G} \bar{\Sigma}_{g,i}^{Core} \tilde{\phi}_{g,i}^{Core}, \quad (2.8)$$

where i and m are the pin-cell and sub-pin region indices; g and G are the fine and condensed group indices; ϕ^{Core} is the flux obtained from the heterogeneous core calculation; and the bar sign indicates the value is averaged over the pin while the tilde sign indicates the normalized weighting spectrum for the homogenized pin. Since the fine group core PHXS and flux can be represented by their SA counterparts and the perturbations (Δ) [25] [30] as:

$$\bar{\Sigma}_{g,i}^{Core} = \bar{\Sigma}_{g,i}^{SA} + \Delta \bar{\Sigma}_{g,i}, \quad \tilde{\phi}_{g,i}^{Core} = \tilde{\phi}_{g,i}^{SA} + \Delta \tilde{\phi}_{g,i}, \quad (2.9)$$

Eq. (2.8) can be re-written as the follow:

$$\begin{aligned} \bar{\Sigma}_{G,i}^{Core} &= \sum_{g \in G} \bar{\Sigma}_{g,i}^{Core} \tilde{\phi}_{g,i}^{Core} = \sum_{g \in G} (\bar{\Sigma}_{g,i}^{SA} + \Delta \bar{\Sigma}_{g,i}) (\tilde{\phi}_{g,i}^{SA} + \Delta \tilde{\phi}_{g,i}) \\ &= \sum_{g \in G} (\bar{\Sigma}_{g,i}^{SA} \tilde{\phi}_{g,i}^{SA} + \Delta \bar{\Sigma}_{g,i} \tilde{\phi}_{g,i}^{SA} + \bar{\Sigma}_{g,i}^{SA} \Delta \tilde{\phi}_{g,i} + \Delta \bar{\Sigma}_{g,i} \Delta \tilde{\phi}_{g,i}) \\ &= \bar{\Sigma}_{G,i}^{SA} + \mathbf{E}_{G,i}^{BND} + \mathbf{E}_{G,i}^{CON} + O(E^2) \approx \bar{\Sigma}_{G,i}^{SA} + \mathbf{E}_{G,i}^{BND} + \mathbf{E}_{G,i}^{CON}. \end{aligned} \quad (2.10)$$

The higher order error term is small enough to neglect, therefore, a core PHXS can be represented by the sum of the corresponding SA PHXS and the two error terms associated with the spectral error, namely the boundary spectral error and the group

condensation error denoted by E^{BND} and E^{CON} , respectively. Note that E^{BND} originates from the perturbation of fine-group PHXS ($\Delta\bar{\Sigma}_{g,i}$) exists even without the group condensation, while E^{CON} is caused by the difference of normalized spectrum. Based on Eq. (2.10), a G group macroscopic reaction rate of a pin-cell obtained from the reference heterogeneous calculation can be written as:

$$\tau_{G,i}^{Core} = \bar{\Sigma}_{G,i}^{Core} \bar{\phi}_{G,i}^{Core} = \left(\bar{\Sigma}_{G,i}^{SA} + E_{G,i}^{BND} + E_{G,i}^{CON} \right) \bar{\phi}_{G,i}^{Core}, \quad (2.11)$$

so that the effect of each error term can be quantified.

For the KAIST 1A cores, the quantification was performed as follows: (1) the 47G PHXSs and pin-averaged fluxes were obtained from *MOC-Het* for the core and SAs; (2) the condensed group PHXSs ($\bar{\Sigma}_{G,i}^{Core}$, $\bar{\Sigma}_{G,i}^{SA}$), error terms ($E_{G,i}^{BND}$, $E_{G,i}^{CON}$), and flux ($\bar{\phi}_{G,i}^{Core}$) were obtained by employing various group structures given in **Table 2.3**; and (3) the pinwise 1G reaction rate errors due to the SA PHXSs were determined. Specifically, the following three reaction rate error terms were obtained:

$$\begin{aligned} \text{Total Spectral Error: } & \sum_G \left(\bar{\Sigma}_{G,i}^{SA} \bar{\phi}_{G,i}^{Core} - \tau_{G,i}^{Core} \right) / \sum_G \tau_{G,i}^{Core}, \\ \text{Boundary Spectral Error } (E_i^{BND}): & -\sum_G E_{G,i}^{BND} \bar{\phi}_{G,i}^{Core} / \sum_G \tau_{G,i}^{Core}, \\ \text{Group Condensation Error } (E_i^{CON}): & -\sum_G E_{G,i}^{CON} \bar{\phi}_{G,i}^{Core} / \sum_G \tau_{G,i}^{Core}. \end{aligned} \quad (2.12)$$

Table 2.3. Energy group structures for the group condensation

#. Groups	2	4	8	16
			2.23E+06	2.23E+06
			8.21E+05	8.21E+05
		9.12E+03	9.12E+03	9.12E+03
			1.30E+02	1.30E+02
				1.37E+01
				6.48E+00
		3.93E+00	3.93E+00	3.93E+00
				1.46E+00
				1.07E+00
Lower energy boundary (eV)	6.25E-01	6.25E-01	6.25E-01	6.25E-01
				3.58E-01
			1.46E-01	1.46E-01
				8.20E-02
				4.28E-02
				1.24E-02
	1.00E-04	1.00E-04	1.00E-04	1.00E-04

The minus signs in Eq. (2.12) for E^{BND} and E^{CON} are intended to make the sum of E^{BND} and E^{CON} is the total error, while the definitions in Ref. [30] are to make the sum of three errors is zero. For **Table 2.3**, it would be worthwhile to note that the 2G structure is determined with the well-known thermal cut-off energy of 0.625 eV. The 4G structure is determined by refining the fast energy group into three fine groups. One group is assigned to the near 1eV resonance peak of U-235 and the other groups are obtained with the boundary energy of 9.12 keV from which the resolved resonance starts. The 8G structure is determined by dividing the thermal group into two and the first and second groups of the 4G structure into 3 and 2 groups, respectively. The 16G structure was determined by further dividing the 8G structure so that 6 groups are assigned in the thermal energy range.

The RMS and MAX errors of the pinwise 1G kappa-fission reaction rate, which are directly related with the relative pin ΔP , are presented in **Table 2.4** and the radial

reaction rate error distributions for the ARI case are shown in **Figure 2.14**. The ARO results are highly similar with the ARI so that the figures are not included.

Table 2.4. Dependence of the spectral error components on the number of energy groups for the KAIST 1A cores

Case	NG	Total Error (%)		E^{BND} (%)		E^{CON} (%)	
		RMS	MAX	RMS	MAX	RMS	MAX
ARO	2	1.13	3.85	0.40	2.21	0.89	4.06
	4	1.14	4.38	0.40	2.21	0.91	4.70
	8	0.84	4.80	0.38	2.04	0.47	2.63
	16	0.30	1.52	0.40	2.22	0.11	0.67
ARI	2	1.12	4.14	0.34	2.17	0.96	4.26
	4	1.13	4.45	0.34	2.17	0.94	4.79
	8	0.73	4.70	0.33	2.02	0.42	2.57
	16	0.27	1.50	0.35	2.19	0.09	0.66

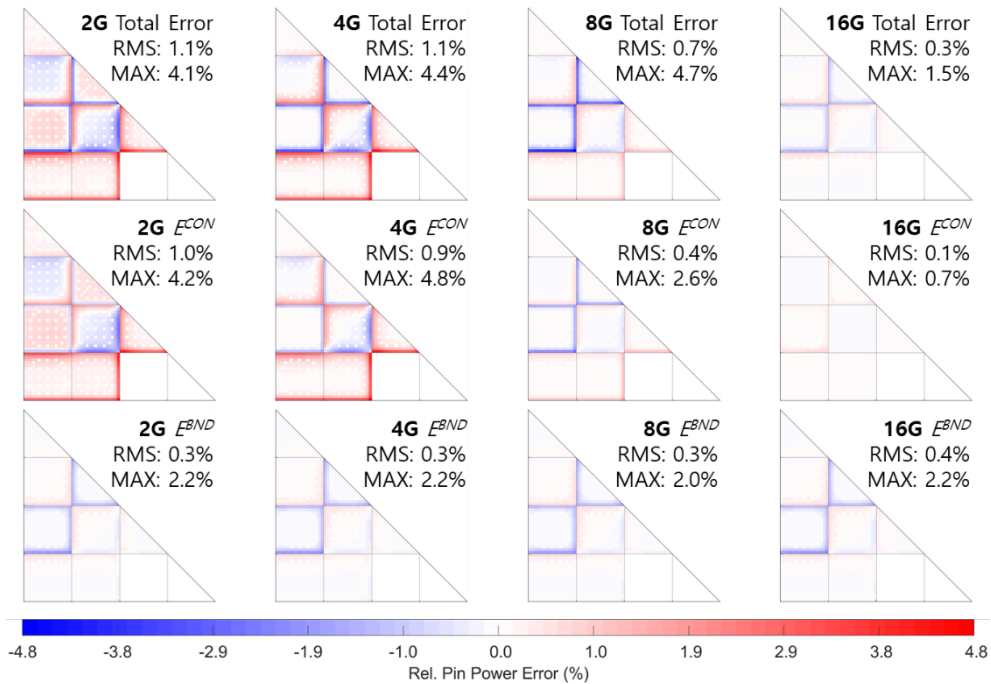


Figure 2.14. Relative pin power error (%) distributions due to the total spectral error (top), group condensation error (middle), and boundary spectral error (bottom)

From **Table 2.4** and the bottom row of **Figure 2.14**, it is noted that E^{BND} is nearly unaffected by the number of energy groups and it is remarkable only at the assembly boundaries. It can be understood by the fact that the thermal neutrons whose behavior is highly sensitive to the local heterogeneity have short mean free paths (MFP) of about a pin pitch. If the outermost pin-cells of the MOX FAs where E^{BND} is especially severe are not included, the RMS/MAX errors decrease from about 0.4%/2.2% to 0.2%/1.1% for the ARO and ARI cores with the 16G, and the nearly identical results are obtained with the different energy groups. Although the effect of E^{BND} locally appears, the MAX errors are not negligible because the normalized pin powers at the MOX FA boundaries are larger than 2.0. Furthermore, E^{BND} is unavoidable as far as SA PHXSs are used, unless a proper leakage correction technique is employed.

On the other hand, **Table 2.4** and the middle row of **Figure 2.14** show that E^{CON} is notably larger than E^{BND} and the use of more energy groups reduces E^{CON} . For the ARI case, the RMS/MAX of E^{CON} is about 1.0%/4.3% for the 2G, but it is 0.4%/2.6% for the 8G and 0.1%/0.7% for the 16G. The refined energy groups localize E^{CON} as well. As fewer groups are used, E^{CON} considerably increases even for the internal pins so that large errors are noted inside the FAs. Therefore, 2 or 4G structure might result in unacceptable errors unless elaborated tuning of the group structure is made for a range of PHMGCs [46], and 8 and more groups are required to reduce the RMS of E^{CON} and the resulting total spectral error within 0.5% and 1.0%. Consequently, the 8G would be desirable to yield generally good results while saving the computing cost, and it is selected as the default energy group structure for VANGARD.

The analyses presented in this chapter demonstrate that the spatial homogenization error predominates the errors due to the use of MG PHXSs in PHMGC; the boundary spectral error (E^{BND}) is unavoidable even with the 16G and it is not sensitive to the number of groups; the condensation error (E^{CON}) is large and appears in the assembly interior region if the number of groups is insufficient; and the spectral error can be significant if the configuration is highly heterogeneous.

In order to reduce the spectral error, employment of a leakage correction technique

is determined, and it leads to development of the pinwise LFM. By functionalizing the MG PHXSs to the leakage, the pinwise LFM can simultaneously correct E^{BND} and E^{CON} . The details of the pinwise LFM are provided in **Chapter 3**.

2.3. Errors due to Lower Order Solution Methods

The requirement for a sufficient number of energy groups in PHMGC confirmed in **Chapter 2.2** renders another requirement for adopting an elaborated solution method. It is due to the large changes of thermal PHXSs resulting in significant flux gradients as more energy groups are used with the pinwise geometry representation. In order to show the effect of the increased local heterogeneity, the *MOC-XG* results were obtained for the C5G7 based 1D pin array of **Figure 2.8** with the assembly-and pin-homogenized 2G XSs and the 7G PHXSs. The XSs were directly obtained from the 7G heterogeneous MOC calculation, and G1 – 4 and G5 – 7 were taken as the fast and thermal groups for the condensation.

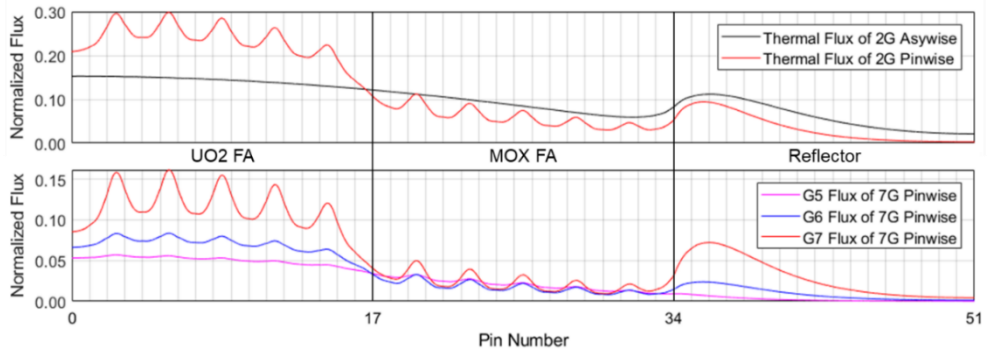


Figure 2.15. Thermal range flux distributions of *MOC-2G* with the assembly-and pin-homogenized XSs (top) and *MOC-7G* with the PHXSs (bottom)

Figure 2.15 presents the thermal flux distributions of the *MOC-XG*. It is noted that refining both geometry and energy range renders the steep flux gradient, and the degree of flux variation increases as the energy group index increases. It should also be noted that the higher angular moments of the SP_N formulation may reveal even

much severe spatial variations. It is the reason that the use of the nodal expansion method (NEM) solver for the SP₃ core calculation yielded unphysical fluctuations of the 2nd angular moment as noted in Ref. [12].

Although the primary purpose of the pinwise EFs in the core calculation is to correct the spatial homogenization error, the transport and discretization errors determined by a solver are also corrected. It is the reason that a very low order solver can yield acceptable results. This additional correction is introduced by the proper EF generation process which is to be performed with each solver employing the set of MG PHXSs and associated reference solution, such as the heterogeneous pin-averaged flux (ϕ_g^{Het}) for the SPH iteration presented in **Figure 2.16**.

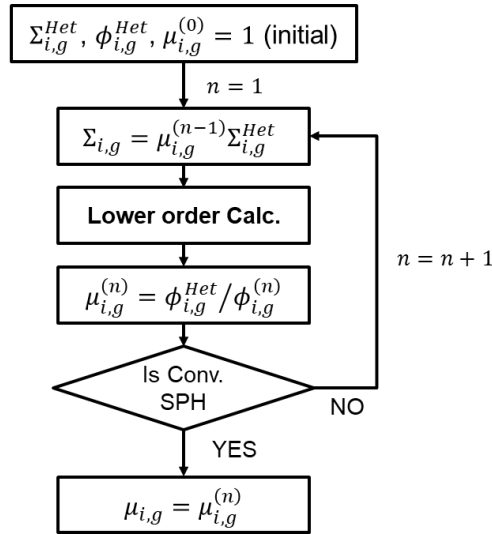


Figure 2.16. Iterative process for the generation of the SPH factors

The SPH iteration is performed as follows. Until the SPH factors are converged, the pinwise fluxes at the n-th step ($\phi_g^{(n)}$) is obtained by a specific lower order solver with the PHXSs (Σ_g^{Het}) and the SPH factors of the previous step ($\mu_g^{(n-1)}$), and the fluxes are used to determine the updated SPH factors ($\mu_g^{(n)}$). Resultantly, proper

degree of the correction for each solver is introduced by the SPH factors.

It means the heterogeneous reference can be exactly reproduced in the equivalent homogeneous problem with the correction introduced by the proper SPH factors. It is irrespective of the number of energy groups, transport approximation, and spatial discretization, in that the SPH factors capture all the possible errors. The results in **Figure 2.17** are the example. Both solvers succeed to reproduce the heterogeneous solution with the core SPH factors while the results without EFs show quite large errors. The MAX $\Delta\rho$ of the NO EF calculation is 5.9% for the CM diffusion FDM and 9.5% for the FM SP₃ FDM. The difference in the NO EF results also revealed that the degree of the additional correction is depending on the solver.

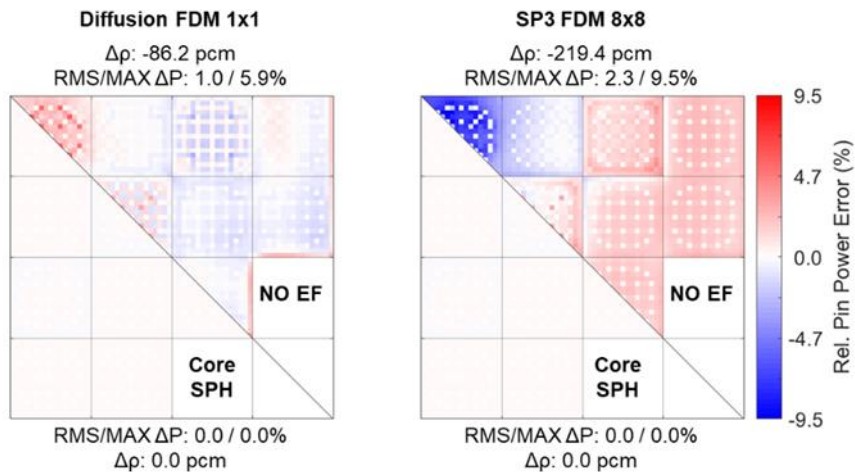


Figure 2.17. Results of the 8G FDM calculations employing the core PHXS set

In the practical core calculation, however, the EFs are generally obtained from smaller sample problems such as the SA configurations for FAs and the fuel-reflector configurations in **Figure 2.3** for the radial reflectors. Therefore, the errors due to the inconsistent EFs are appear in the core calculation results. It is the reason that heavily depending on the EFs for correction of the transport and discretization errors is not desirable. As the core environment deviates more from the reference condition where the EFs are obtained, the agreements would be deteriorated more since the proper

degree of the additional correction cannot be introduced by the single set of EFs. Furthermore, the two errors are large and sensitive to the core environment so that their effect would be more remarkably for highly heterogeneous cores.

Based on the fact that the EFs are depending on the solver, it was assumed that there would be the optimal solution method which can practically minimize the degree of the additional correction, and the use of the optimal solution method can decrease the inconsistency of the EFs in the core. As a preliminary work to verify the assumption, a series of test calculations were performed with the FDM and SENM solvers of the diffusion and SP_3 equations. The test primarily aimed to observe whether the reduction of either or both of the two errors due to the solver actually improve the agreements. In addition, it is to confirm that the degree of the errors can be estimated by comparing the lower order results to the corresponding higher order results without the use of the EFs. The target EF for the test is the SPH factors. It is because the SPH factors are more preferred for the practical PHMGCs due to its simplicity and less requirement for the computing cost. It should be noted that all the pinwise TSCC codes at SNURPL including the diffusion FDM solver of Yoon [17], SPHINCS, and VANGARD employ the SPH factors.

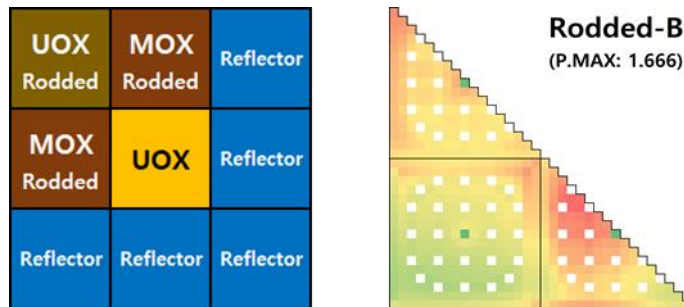


Figure 2.18. Radial core configuration (left) and the pin power distribution (right) of the C5G7 2D Rodded-B case

The C5G7 2D Rodded-B core calculations are a part of the test. **Figure 2.18** presents the radial configuration and the reference pin power distribution of the Rodded-B case. For the problem representing the radial slice of the corresponding

3D benchmark, the 7G calculations were performed with four solvers. The PHXSs and the SPH factors based on the SA and the fuel-reflector configurations were employed. Because the energy group structure is retained in the pin-homogenized problem, the spectral error is marginal, and the inconsistency of the SA SPH factors has larger effect on the solution. Each of the solvers is a combination of the diffusion and SP₃ theory with the FDM and SENM. Note that each pin-cell is taken as the base mesh, and the discretization error of the pinwise SENM is slightly less than the FM FDM with 8x8 meshes per pin [19]. More details of the pinwise SENM solver is provided later in this chapter. The results were compared with two kinds of the reference solutions, one obtained by the pin-homogenized MOC calculation (*MOC-7G*) and the other obtained by the heterogeneous MOC calculation (*MOC-Het*).

The calculations were performed without and with the SPH factors, and those are noted by *NO SPH* and *With SPH*, respectively. The *NO SPH* results are obtained to show that the comparisons which are not involving the EFs is required to investigate the errors due to the solver. It means the lower order calculation result should not be corrected by the EFs and should be compared with the reference solution based on the same PHXS set and no EFs, in order to assess the solvers. It is confirmed by comparing the results presented in **Figure 2.19** and **Figure 2.20**. In **Figure 2.19**, the errors are obtained from the *NO SPH* versus *MOC-Het* comparisons, so the errors due to the PHXSs as well as the solvers are simultaneously affecting the results. It is hard to figure out the magnitude of the errors due to the solver.

In **Figure 2.20**, in contrast, the errors are obtained from the *NO SPH* versus *MOC-7G* comparisons. The results are determined by the solver so that the effect of the transport and discretization errors is noted more clearly. As presented in the figure, the diffusion FDM calculation which involves the largest transport and discretization errors yielded about 7.9%/15.7% of the RMS/MAX pin ΔP . The errors are rather increased to 9.6%/20.8% by the SP₃ FDM in that the error cancellation between the two errors are weakened by reducing only the transport error. The diffusion SENM decreased the errors to 2.5%/8.1% by reducing the discretization error which is especially large in this case. Lastly, the SP₃ SENM yielded further improvement to

1.6%/3.4% by reducing both of the two errors. Consequently, the degree of the additional correction is smallest for the SP₃ SENM, and it is followed by the diffusion SENM, diffusion FDM, and SP₃ FDM.

The results presented in **Figure 2.21** were obtained by comparing the lower order calculation results aided by the SPH factors to the *MOC-Het* reference, following the standard PHMGC procedure. As shown in the figure, the RMS/MAX pin ΔP are about 0.7%/3.0% for the SP₃ SENM calculation, and it is followed by 1.8%/4.1% for the diffusion SENM. The diffusion and SP₃ FDM calculations yielded notably larger pin ΔP . The errors are 2.3%/7.2% for the diffusion and 2.1%/10.2% for the SP₃. In that the spectral error is negligible, within about 0.1%/1.0% for the RMS/MAX pin ΔP , the errors are mainly determined by the inconsistent SPH factors. It means the good agreements of the SP₃ SENM originate from alleviation of the inconsistency of the SPH factors by reducing the additional correction.

The Δp and RMS/MAX ΔP errors presented in **Figure 2.19**, **Figure 2.20**, and **Figure 2.21** are summarized in **Table 2.5**. Note that the diffusion is noted as SP₁ in the table for the convenience.

**Table 2.5. Summary of the C5G7 2D Rodded-B core calculation results
(Ref. k-eff: 0.963586 for *MOC-Het* / 0.959933 for *MOC-7G*)**

Case	Solver	Δp (pcm)		RMS Pin ΔP (%)		MAX Pin ΔP (%)	
		SP1	SP3	SP1	SP3	SP1	SP3
<i>NO SPH</i> vs. <i>MOC-Het</i>	FDM	-356.2	818.3	5.28	6.99	9.76	14.50
	SENM	-1781.3	-759.0	4.89	4.30	13.16	9.53
<i>NO SPH</i> vs. <i>MOC-7G</i>	FDM	38.8	1213.3	7.87	9.58	15.65	20.80
	SENM	-1386.3	-346.0	2.48	1.63	8.14	3.39
<i>With SPH</i> vs. <i>MOC-Het</i>	FDM	-170.4	-103.5	2.34	2.05	7.24	10.19
	SENM	-42.8	25.4	1.78	0.70	4.12	3.02

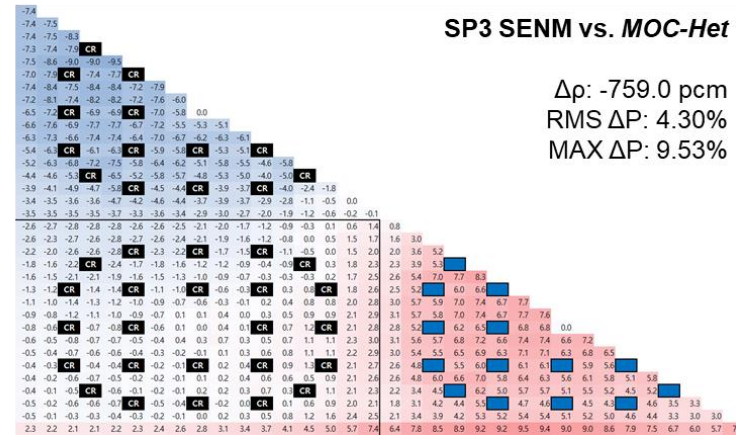
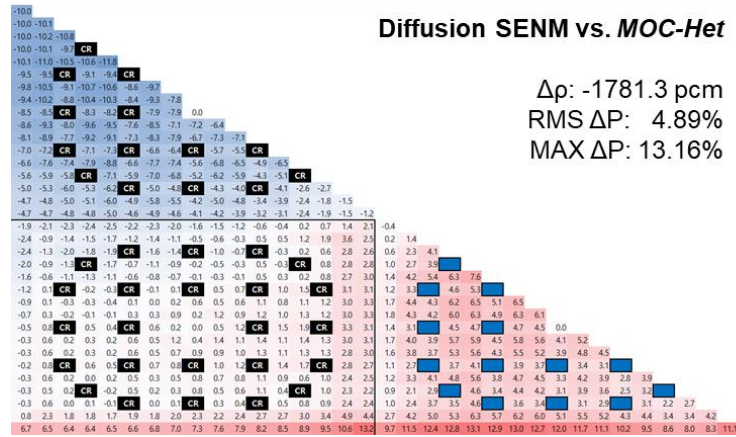
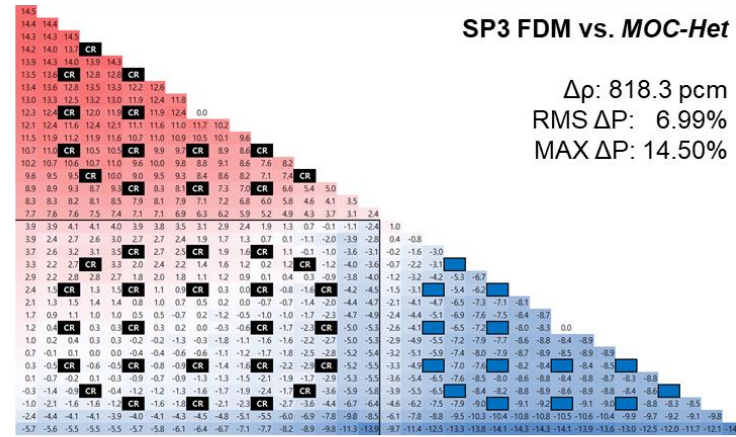
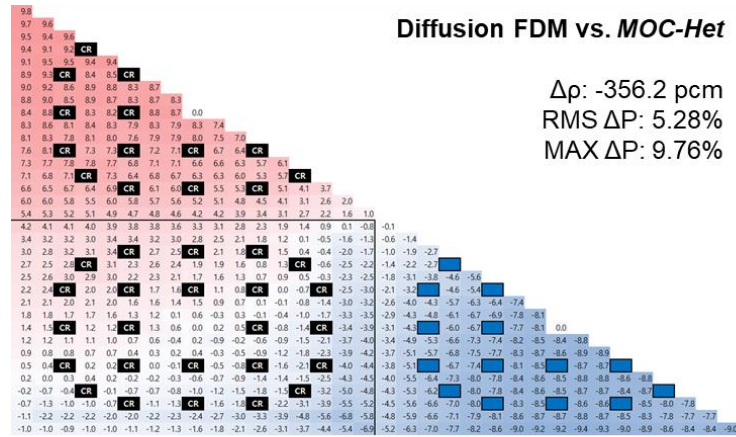


Figure 2.19. Comparison of the SP_N results **without the SPH factors** to MOC-Het for the C5G7 2D Rodded-B (Ref. k-eff: 0.963586)

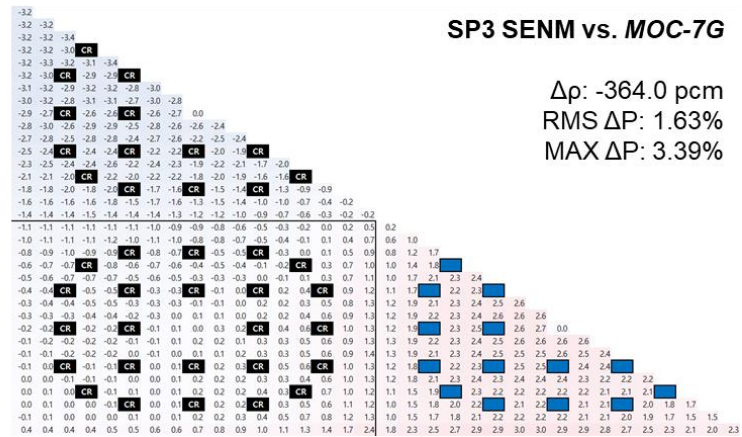
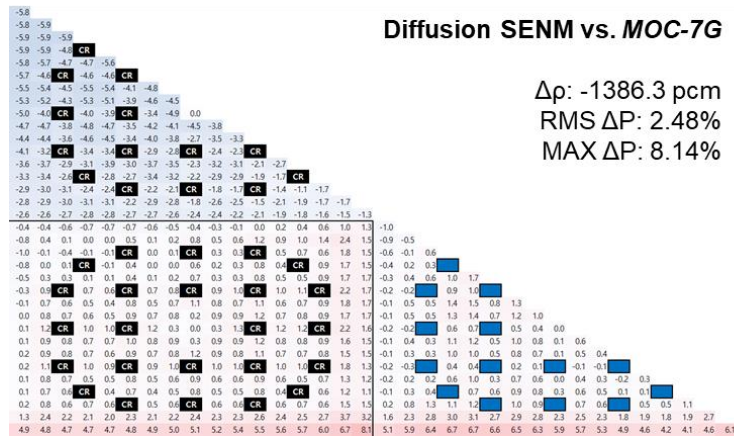
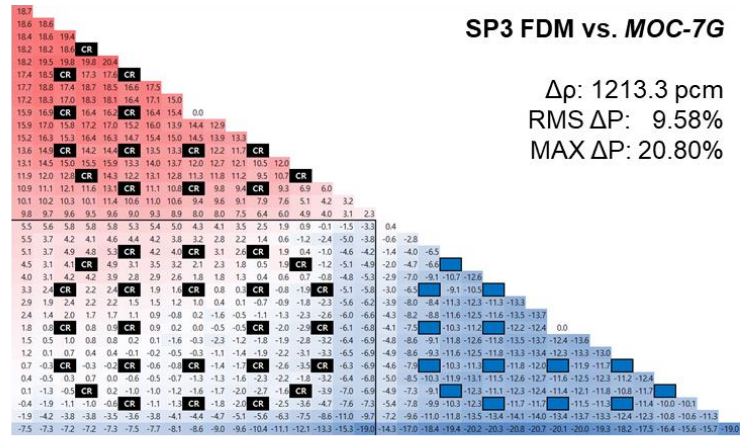
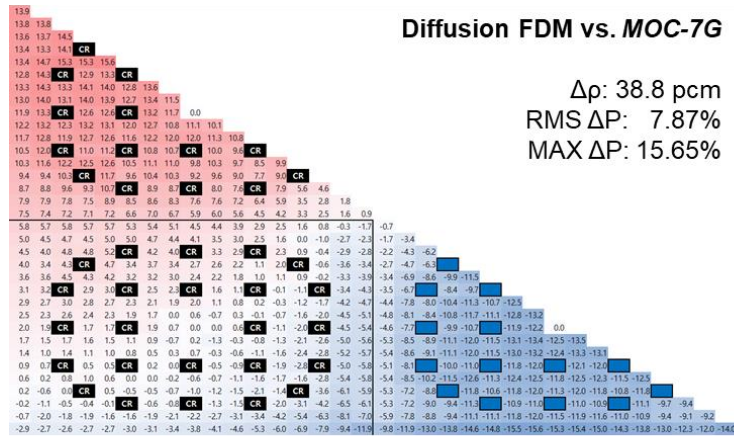


Figure 2.20. Comparison of the SPN results with the SPH factors to MOC-7G for the C5G7 2D Rodded-B (Ref. k-eff: 0.959933)

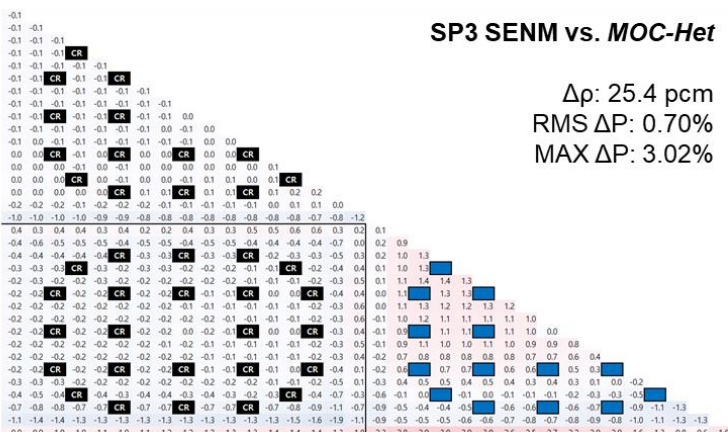
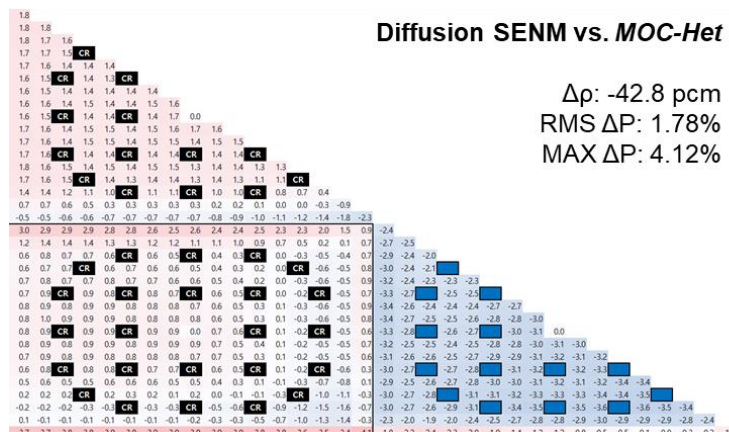
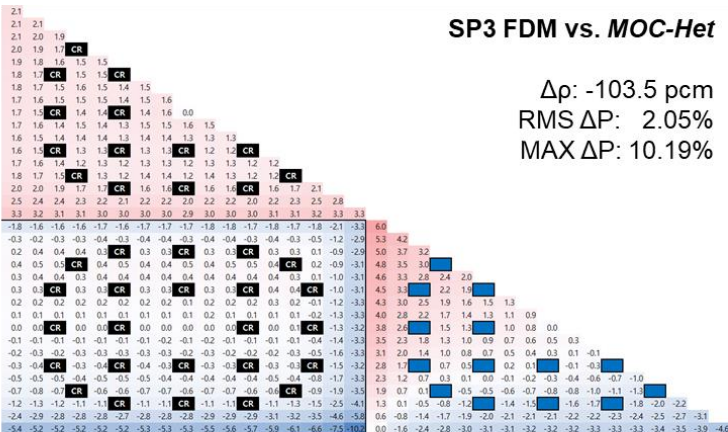
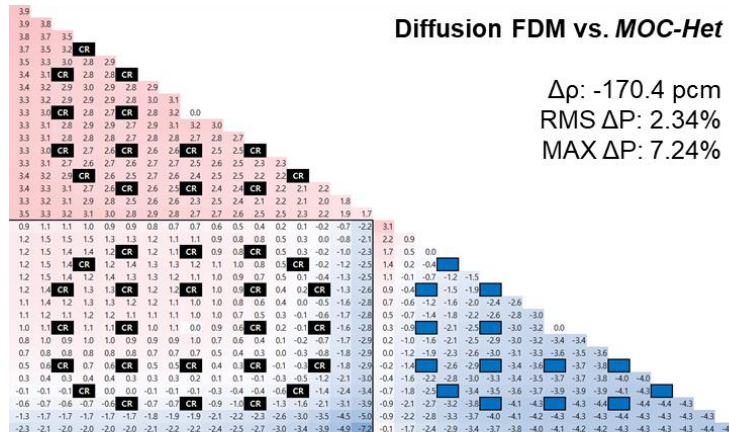


Figure 2.21. Comparison of the SPn results with the SPH factors to MOC-Het for the C5G7 2D Rodded-B (Ref. k-eff: 0.963586)

Based on the preliminary study, more extensive studies were performed to figure out whether the SP_3 SENM solver is the optimal or a better solution method exists. This chapter presents the results. As the beginning, the transport error due to the approximation of the NTE and the spatial discretization error depending on not only the mesh size but also the transport approximation is investigated in **Chapter 2.3.1**. The core PHXSs are used without the SPH factors and the core calculation results obtained by various lower order solvers are compared with the pin-homogenized reference solution, as noted in **Chapter 2.1**. In addition to the diffusion and SP_3 FDM, the SP_5 solver is employed to examine the higher order SP_N method, and the S_N solver based on the diamond differencing (DD) scheme [47] is also employed to evaluate the highly rigorous transport method in PHMGC. In that the VANGARD code has the GPU acceleration capability and previous studies including Ref. [48] has been demonstrated the exceptional computing performance of GPGPU, it was considered to employ the S_N solver if it has a clear advantage. The error cancellation between the transport and discretization errors is also investigated in detail.

Because the fact that the FM SP_3 FDM solver can successfully reduce the degree of the additional correction is revealed but the computing cost required for the FM FDM core calculation is too demanding, the SENM solver is employed. The one-node SP_3 SENM solver is derived in **Chapter 2.3.2**, and its accuracy is demonstrated for a 1D pin array and 2D SA problems. The one-node SENM solver can be easily applied for the higher order SP_N so that the SP_5 SENM solver is also derived.

Further investigations for the inconsistency of the SPH factors are then performed in **Chapter 2.3.3**. In this chapter, the flux-weighted assembly average of the SPH factor (AA-SPH) [49] for each group is introduced to normalize the core SPH factors. It is to compare the pinwise SPH factor distribution shapes, which is depending on not only the solver but also the assembly BC employed for the generation of the SPH factors. The normalized core SPH factors versus the SA SPH factors comparisons reveal that the difference of the pinwise SPH factor distribution shapes is reduced by the use of the proper solver. Test calculations using the core PHXSs and the SA SPH factors confirm that the reduction decreases the errors due to the inconsistency of the

SPH factors. In addition, it is also shown that the SPH factors for the S_N solver are sensitive to the BC, so the large error globally appears, and the error especially noted in the fast energy range leads to intolerable errors.

2.3.1. Assessment of the transport error and the discretization error

In order to reveal the degree of the additional correction required for each lower order solution method, the KAIST 1A core calculations were performed. Similar to the preceding study noted in **Chapter 2.1**, the errors are assessed by comparing lower order results with the corresponding higher order reference based on the same PHXSs. The transport error is assessed by comparing two FM results based on the core PHXSs, one is yielded by a lower order transport method and the other is yielded the best possible transport method, namely the MOC in this work. The discretization error is assessed by the CM vs. FM comparison based on the same transport method in that the discretization error has dependence on the transport method. The overall error is assessed by comparing a specific lower order calculation result with the reference transport solution based on the FM.

The transport approximation methods tested here are the diffusion, SP_N with $N = 3$ and 5 , and the S_N methods. The diffusion is denoted as the SP_1 for convenience. A FM FDM with 16×16 meshes per pin is used to solve the SP_N equations. For the S_N solver, the DD scheme with the same 16×16 meshes per pin is used and the discrete angles and weights are determined by the level-symmetric quadrature. The 4 and 8G core PHXSs are used without the SPH factors to obtain the lower order results and the reference. It should be noted that 16G examination results are not presented in that the results are not notably different from the 8G results. All the SP_N and the S_N results are compared with the *MOC-XG* references. The errors determined by the transport approximations are summarized in **Table 2.6** and **Table 2.7**, and radial distributions of the relative (Rel.) pin ΔP obtained from the 8G calculations are shown in **Figure 2.22**. Note that the numbers presented with the case ID are the multiplication factors obtained from the pin-homogenized MOC calculations.

Table 2.6. Transport errors obtained by the 4G FM calculations for KAIST 1A

Case	Solver	$\Delta\rho$ (pcm)	Absolute Pin ΔP (%)		Relative Pin ΔP (%)	
			RMS	MAX	RMS	MAX
1.135769	SP ₁	-661.1	2.19	5.95	2.91	9.76
	SP ₃	-534.8	1.38	3.79	2.43	11.50
	SP ₅	-512.2	1.34	3.99	2.38	11.86
	S ₄	-23.6	0.32	1.58	0.26	1.30
	S ₆	-11.9	0.13	0.72	0.11	0.60
	S ₈	-7.6	0.07	0.40	0.06	0.32
0.978799	SP ₁	-2325.2	2.67	8.93	3.18	10.28
	SP ₃	-1448.5	2.45	8.13	2.53	13.16
	SP ₅	-1430.0	2.56	8.55	2.61	13.39
	S ₄	-128.0	0.99	3.39	0.96	3.29
	S ₆	-65.0	0.48	1.44	0.48	1.57
	S ₈	-37.8	0.27	0.78	0.27	0.86

Table 2.7. Transport errors obtained by the 8G FM calculations for KAIST 1A

Case	Solver	$\Delta\rho$ (pcm)	Absolute Pin ΔP (%)		Relative Pin ΔP (%)	
			RMS	MAX	RMS	MAX
1.131685	SP ₁	-362.9	1.88	6.60	1.68	5.32
	SP ₃	-193.9	0.82	2.50	0.78	3.14
	SP ₅	-176.4	0.76	2.17	0.73	3.47
	S ₄	-27.2	0.33	1.61	0.28	1.30
	S ₆	-13.7	0.14	0.74	0.13	1.13
	S ₈	-9.8	0.07	0.41	0.07	0.65
0.972298	SP ₁	-1809.8	5.43	16.52	5.05	10.63
	SP ₃	-787.8	1.80	6.32	1.70	3.87
	SP ₅	-672.9	1.20	4.94	1.13	3.73
	S ₄	-156.8	1.04	3.47	1.01	3.48
	S ₆	-79.8	0.50	1.46	0.50	1.68
	S ₈	-47.3	0.28	0.79	0.28	0.94

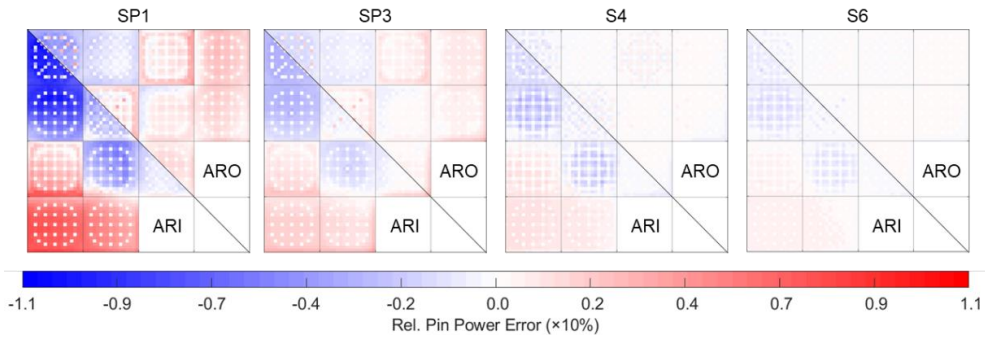


Figure 2.22. Relative pin power error (%) distributions originate from the transport error of the 8G FM calculations for KAIST 1A

From **Table 2.6** and **Table 2.7**, it is first noted that the errors of the SP_N solvers are depending on the number of energy groups and are notably reduced by increasing the number from 4G to 8G. It is because the group condensed diffusion coefficient for the G -th group (D_G) is not the same with the inverse of the G -th group transport XS divided by 3, since D_G is obtained by condensing the fine g -th group D_g [44]. The difference is larger in the 4G calculations due to the number of energy groups below the thermal cut-off energy 0.625eV is insufficient.

The difference is alleviated in the 8G calculations. However, the diffusion solver shows rather increased errors for the ARI case. The RMS/MAX Rel. ΔP are about 3.2%/10.3% for the 4G and 5.1%/10.6% for the 8G, therefore, the decrease of $\Delta\rho$ from -2325 to -1810 pcm is merely an error cancellation. The MAX ΔP of the diffusion that is higher than 5% even for the 8G ARO case is not tolerable.

Figure 2.22 shows that the ΔP error is especially large at around GT and BA pins, assembly boundary regions, and the core periphery. The errors are notably reduced by the SP_3 solver in that the $\Delta\rho$ and RMS/MAX Rel. ΔP errors are reduced by 1022 pcm and 3.4%/6.8% for the 8G ARI case. However, the errors themselves are not sufficiently small in that the $\Delta\rho$ of the SP_3 are nearly 200 and 800 pcm for the 8G ARO and ARI cases. Further improvements are attained by the SP_5 solver, but the differences between the SP_3 and SP_5 results are notably smaller than those between the diffusion and SP_3 . In contrast, the S_N method reduces the errors consistently as N

goes higher. Even for the 8G ARI case, S_6 yielded less than 80 pcm of $\Delta\rho$ and about 0.5%/1.7% of RMS/MAX ΔP , and S_8 yielded less than 1.0% for MAX ΔP .

Although the accuracy of the S_N cases is remarkable everywhere in the core, it must be noted that the transport error at the interior of an assembly can be captured by the SA based SPH factors in the core calculations. Because the unavoidable errors occurring at the assembly boundary are relatively smaller than those at the assembly internal region are, an SP_N solver can be used together with the SPH factors.

For the assessment of the discretization error, the CM SP_N FDM and CM S_N DD calculations were performed, and the results were compared with the corresponding FM reference solutions based on 16x16 meshes per pin. Namely, the error of the SP_3 FDM calculation with an arbitrary mesh number was estimated by comparison with the FM SP_3 FDM. The core PHXSs without the SPH factors were used as well.

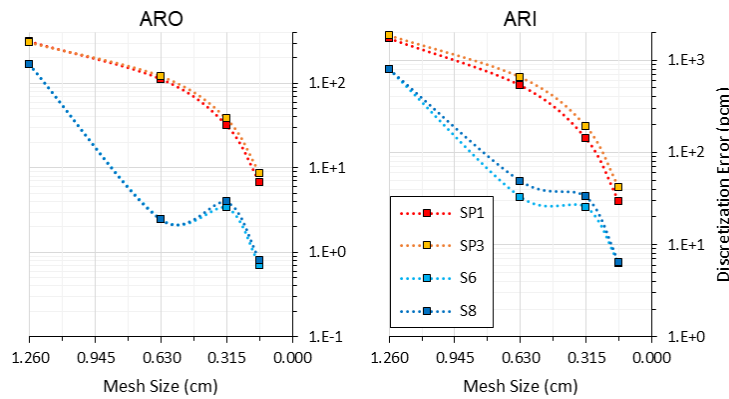


Figure 2.23. Discretization errors obtained with various solution methods

Table 2.8 shows the discretization errors obtained from the SP_3 FDM and S_8 DD calculations with the 8G PHXSs. Note that the diffusion FDM results are similar to the SP_3 FDM results and the S_4 and S_6 DD results are similar to the S_8 DD results, as presented in **Figure 2.23**. In general, the discretization error increases with the energy group index because the flux gradient becomes more severe in the low energy groups as more groups are used in the thermal energy range. The $\Delta\rho$ error of the SP_3

1x1 FDM for ARI, for example, is 1148 pcm, 1660 pcm, 1837 pcm, and 1919 pcm for the 2, 4, 8 and 16G cases. However, the mesh size dependence of the errors in terms of the error reduction ratio is not very sensitive to the number of groups so that only the 8G results are presented.

Table 2.8. Discretization errors obtained by the 8G SP3 FDM and S8 DD calculations for KAIST 1A

Case	Solver	Pin Mesh	$\Delta\rho$ (pcm)	Absolute Pin ΔP (%)		Relative Pin ΔP (%)	
				RMS	MAX	RMS	MAX
ARO	SP ₃ FDM	1x1	303.4	4.76	22.85	4.00	18.79
		2x2	121.2	1.78	8.15	1.51	6.73
		4x4	37.8	0.55	2.45	0.47	2.08
		8x8	8.6	0.12	0.56	0.11	0.47
	S ₈ DD	1x1	-167.8	2.80	15.47	2.38	12.51
		2x2	-2.4	0.28	1.56	0.23	1.21
		4x4	-3.9	0.08	0.46	0.07	0.38
		8x8	-0.8	0.02	0.10	0.01	0.08
ARI	SP ₃ FDM	1x1	1836.7	14.13	40.86	13.16	33.34
		2x2	648.8	5.22	14.62	4.85	11.98
		4x4	189.5	1.56	4.40	1.45	3.64
		8x8	41.4	0.35	0.99	0.32	0.82
	S ₈ DD	1x1	-797.7	7.13	23.29	6.58	18.41
		2x2	-49.0	0.53	2.09	0.48	1.88
		4x4	-33.0	0.25	0.76	0.24	0.67
		8x8	-6.4	0.05	0.15	0.05	0.13

In the table, it is first noted that the core calculations with 1x1 mesh per pin yielded remarkably large deviations from the FM reference, although the pin pitch is only 1.26cm. The errors of the SP₃ 1x1 FDM are about 1837 pcm and 13.2%/33.3% for the $\Delta\rho$ and RMS/MAX Rel. pin ΔP errors in case of the ARI. The use of the refined meshes rapidly decreases the errors. With 8x8 meshes, the $\Delta\rho$ and RMS/MAX Rel. ΔP errors drop to 41 pcm and 0.4%/1.0%, and the ΔP is noticeable only at the

assembly interior region where the SA SPH factors can capture it. For S_8 DD, similar degree of the errors was obtained with 4x4 meshes per pin.

Figure 2.24 shows the relative pin ΔP error distributions of the 8G SP₃ FDM based on various mesh sizes. Similar to the transport error, the pin ΔP is relatively large at the assembly interior region due to the severe local heterogeneity which originates from GTs, BAs, and CRs. It is important to observe that the pattern of the transport errors in **Figure 2.22** and that of the discretization errors in **Figure 2.24** are similar but the signs are opposite. It means the two errors cancel each other in the SP_N calculations, as noted in the introduction of **Chapter 2** and outlined in **Chapter 2.1**. It is the reason that the CM diffusion FDM yielded apparently good errors in previous studies [8] [20] in spite the transport and discretization errors are both large.

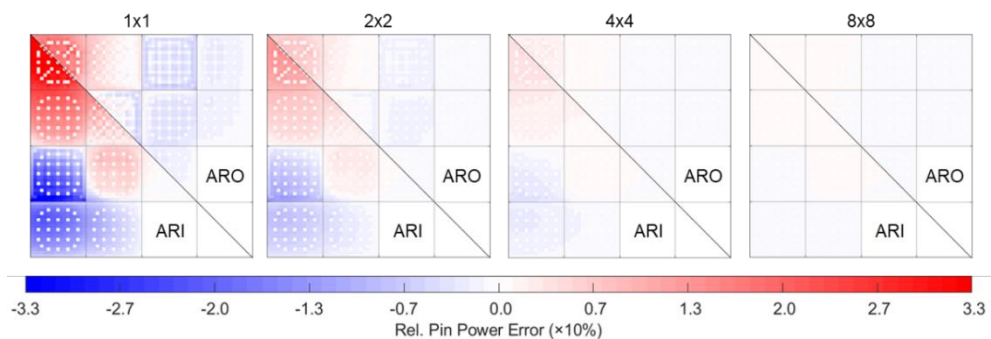


Figure 2.24. Relative pin power error (%) distributions originate from the discretization error of the 8G SP₃ FDM calculations for KAIST 1A

The error cancellation appears in the diffusion and SP_N calculation results and it originates from the representation of neutron current using the diffusion coefficient and the flux gradient. For convenience of the discussion, a small problem composed of two UO₂ fuel pins (UX) and a waterhole pin (WH) arranged in UX-WH-UX order is employed. The pin-cells are taken from C5G7 and the 7G calculations with PHXSs were performed with selected lower order solvers.

It is clearer to understand how the transport error appears. **Figure 2.25** shows the flux distributions in G7 obtained by the S_{20} DD and the FM diffusion and SP₃ FDM

solvers. The flux is normalized to yield the unit fission source. Each of the pin-cells is subdivided into 32 meshes so the discretization error is negligible. The increased transport error makes the flux distribution smoother in that the neutron streaming effect cannot be properly considered. Since the configuration is simple 1D, the SP₃ result is comparable to the S₂₀ in this case.

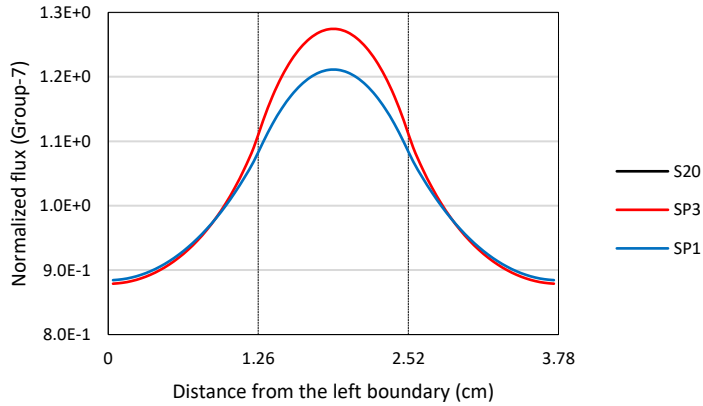


Figure 2.25. G7 flux distributions obtained by different solvers

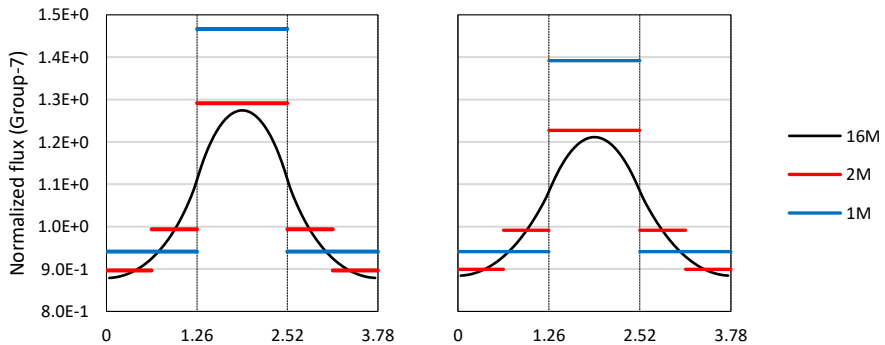


Figure 2.26. G7 flux distributions obtained by the SP₃ (left) and the diffusion (right) solvers with different mesh sizes

On the other hand, the discretization error differently appears. In the diffusion and SP_N FDM calculations, the flux gradient at the UX-WH interface is increased as the mesh size is increased, as shown in **Figure 2.26**. For the FDM calculations, the pin-

cells are subdivided into 1 (1M), 2 (2M), and 16 (16M) meshes and the resulting scalar fluxes are normalized to the unit fission source. It should be noted that the level of the pin-averaged G7 flux in the fuel pin-cells is nearly constant and irrelevant to the transport method and the mesh sizes. It is because the most of fission reaction, nearly about 68% of the total, occurs in G7, and the flux level required to yield the fixed amount of the fission source is determined by the nu-fission PHXS.

In this small problem, the lifecycle of neutrons starts from the fuel pins due to the fission reactions. The fission neutrons with high energy are slowed down mostly in the waterhole and then stream into the fuel pin. In that the pin-averaged flux level is determined by the fission source, the amount of neutron leakage from the waterhole to the fuel pin is also determined. It is the key to understand the increase of the flux gradient at the UX-WH interface.

In the FDM calculation based on the diffusion theory, for example, the current at the right surface of the i -th mesh is obtained by using the coupling coefficient (\tilde{D}) and the difference of the flux for the two adjacent meshes ($\phi_{i+1} - \phi_i$) as the follow.

$$J = -D\nabla\phi = -\frac{2\beta_i\beta_{i+1}}{\beta_i + \beta_{i+1}}(\phi_{i+1} - \phi_i) = -\tilde{D}(\phi_{i+1} - \phi_i) \quad (2.13)$$

The diffusivity (β_i) is the diffusion coefficient (D_i) divided by the mesh size (h_i), therefore, the coupling coefficient is decreased as the mesh size is increased. In order to conserve the current which is determined by the amount of fission source and the resulting pin-averaged flux level, the flux difference ($\phi_{i+1} - \phi_i$) should be increased as much as the coupling coefficient is decreased. The same phenomenon also occurs in the SP3 FDM calculation. The current is obtained with the coupling coefficient ($\tilde{D}_0 = \tilde{D}$) and the difference of the summed flux ($\hat{\phi}_i = \phi_{0,i} + 2\phi_{2,i}$) as:

$$J_1 = -D_0\nabla\hat{\phi} = -\tilde{D}_0(\hat{\phi}_{i+1} - \hat{\phi}_i) \quad (2.14)$$

where $\phi_{0,i}$ and $\phi_{2,i}$ are the scalar flux and the 2nd angular moment. Therefore, the difference of summed flux ($\hat{\phi}_{i+1} - \hat{\phi}_i$) should be increased to conserve the current when the coupling coefficient is decreased by the coarse mesh size.

Table 2.9. Results of the diffusion (SP₁) and SP₃ FDM calculations for the three-pin problem with the different mesh options (for G7)

Case	32M	16M	8M	4M	2M	1M
SP ₁ $\bar{\phi}_{UO2}$	9.472E-1	9.472E-1	9.471E-1	9.468E-1	9.454E-1	9.411E-1
Rel. Err.		0.00%	-0.01%	-0.05%	-0.19%	-0.65%
J^{Surf}	-7.677E-2	-7.676E-2	-7.668E-2	-7.639E-2	-7.530E-2	-7.197E-2
Rel. Err.		-0.02%	-0.12%	-0.51%	-1.92%	-6.26%
$\phi_{i+1} - \phi_i$	1.502E-2	3.004E-2	6.002E-2	1.196E-1	2.358E-1	4.507E-1
Ratio (vs. 32M)		2.00	4.00	7.96	15.69	30.00
$\bar{\phi}_{WH}$	1.168E+0	1.169E+0	1.172E+0	1.183E+0	1.227E+0	1.392E+0
Rel. Err.		0.06%	0.30%	1.27%	5.06%	19.14%
SP ₃ $\bar{\phi}_{UO2}$	9.470E-1	9.469E-1	9.468E-1	9.464E-1	9.452E-1	9.412E-1
Rel. Err.		0.00%	-0.01%	-0.06%	-0.19%	-0.61%
J^{Surf}	-7.684E-2	-7.682E-2	-7.673E-2	-7.642E-2	-7.544E-2	-7.273E-2
Rel. Err.		-0.03%	-0.14%	-0.54%	-1.82%	-5.35%
$\hat{\phi}_{i+1} - \hat{\phi}_i$	1.504E-2	3.006E-2	6.006E-2	1.196E-1	2.362E-1	4.554E-1
Ratio (vs. 32M)		2.00	3.99	7.96	15.71	30.29
$\bar{\phi}_{WH}$	1.221E+0	1.222E+0	1.226E+0	1.240E+0	1.291E+0	1.466E+0
Rel. Err.		0.08%	0.38%	1.55%	5.75%	20.09%

The discussions above are summarized in **Table 2.9**. The number of meshes per pin is increased from 1 (1M) to 32 (32M), and the corresponding 32M FDM results are the reference for the diffusion and the SP₃ calculations, respectively. The current (J^{Surf}) and the difference of scalar flux ($\phi_{i+1} - \phi_i$) and summed flux ($\hat{\phi}_{i+1} - \hat{\phi}_i$) are obtained from the UX-WH interface at 1.26cm. In other words, the flux difference of the diffusion 32M FDM is obtained from the 32nd mesh at the right end mesh of the first fuel pin and the 33rd mesh at the left end of the waterhole.

As previously noted, the pin-averaged flux ($\bar{\phi}_{UO_2}$) is nearly unchanged by the mesh size, so even the diffusion 1M FDM yielded less than 0.7% of relative error to the diffusion 32M FDM. Thus, the surface current is remained similar in the coarser mesh calculations and the flux difference is increased with the mesh size. For the diffusion 2M FDM where the mesh size is 16 times larger than the reference, for example, the resulting flux difference is increased about 15.7 times, and it leads to 5.1% overestimation of the pin-averaged flux in the waterhole ($\bar{\phi}_{WH}$).

It is similar in the lower order nodal calculation. **Figure 2.27** presents the diffusion NEM calculation results as the example. The figure shows the scalar flux and the net current distributions in G7, and both are normalized to the unit fission source. The order of basis polynomial is denoted by 2nd and 4th, and the diffusion 16M FDM result denoted by 16M is also included for the comparison. It is clearly shown that the 4th order NEM and the FM FDM results are nearly overlapped while the 2nd order NEM yielded somewhat notable deviations.

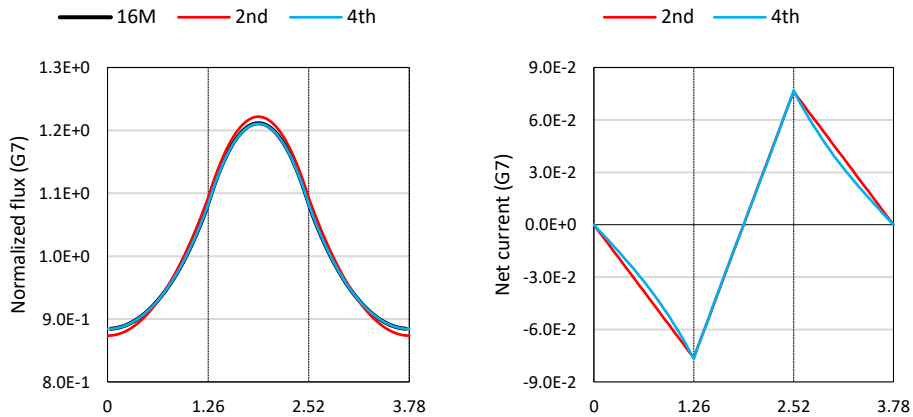


Figure 2.27. G7 scalar flux (left) and net current (right) distributions obtained by the 2nd and 4th order diffusion NEM calculations

It is because the 2nd order NEM should conserve the current with fewer number of the basis. In the NEM calculation, the flux and currents are approximated as:

$$\begin{aligned}\phi(\xi) &= \bar{\phi} + a_1 P_1(\xi) + a_2 P_2(\xi) + a_3 P_3(\xi) + a_4 P_4(\xi) \\ J(\xi) &= a_1 P_1'(\xi) + a_2 P_2'(\xi) + a_3 P_3'(\xi) + a_4 P_4'(\xi)\end{aligned}\quad (2.15)$$

where $\bar{\phi}$ is the average flux and P_n are the basis polynomials defined for $[0, 1]$ interval [50], but the 3rd and 4th order terms are not available in the 2nd order NEM. Thus the 1st (a_1) and the 2nd (a_2) order coefficients are overestimated to yield the similar amount of the leakage. It is shown in **Table 2.10**. Because the flux and current are normalized to the same amount of fission source, the difference between the 2nd and the 4th order NEM calculation results is less than -0.1% for the fuel pin-averaged flux ($\bar{\phi}_{UO_2}$) and -0.8% for the current at the UX-WH interface at 1.26cm (J^{Surf}). On the other hand, the 1st ($a_1^{UO_2}$) and 2nd ($a_2^{UO_2}$) order coefficients for the first fuel pin is overestimated by 10.8% and 1.7%, and the 2nd (a_2^{WH}) order coefficient for the waterhole is also overestimated by 0.2%. Resultantly, about 0.2% overestimation of the pin-averaged flux in the waterhole ($\bar{\phi}_{WH}$) is observed.

Table 2.10. Results of the 2nd and 4th order diffusion NEM calculations for the three-pin problem (for G7)

	NEM 4th	NEM 2nd	Rel. Error (%)
J^{Surf}	-7.678E-2	-7.620E-2	-0.75
$\bar{\phi}_{UO_2}$	9.472E-1	9.466E-1	-0.07
$a_1^{UO_2}$	9.897E-2	1.096E-1	10.79
$a_2^{UO_2}$	-3.596E-2	-3.655E-2	1.65
$\bar{\phi}_{WH}$	1.168E+0	1.179E+0	0.93
a_1^{WH}	0.000E+0	0.000E+0	-
a_2^{WH}	8.581E-2	8.597E-2	0.19

In contrast to the diffusion-like solvers, the characteristic based methods including the S_N does not involve the error cancellation. Instead, alike the transport error, the increase of discretization error makes the smoother flux distribution shape. Because

the outgoing angular flux is defined as:

$$\varphi(s) = \varphi_{in} e^{-\Sigma_r s} + \frac{Q}{\Sigma_t} (1 - e^{-\Sigma_t s}) \quad (2.16)$$

for the incoming angular flux (φ_{in}) and the flat source (Q), the red colored source driven (SD) term cannot be properly considered with too coarse mesh size, while the blue colored attenuation term is not depending on the mesh size. **Figure 2.28** shows the S_2 calculation results based on the short characteristics (SC) as the example.

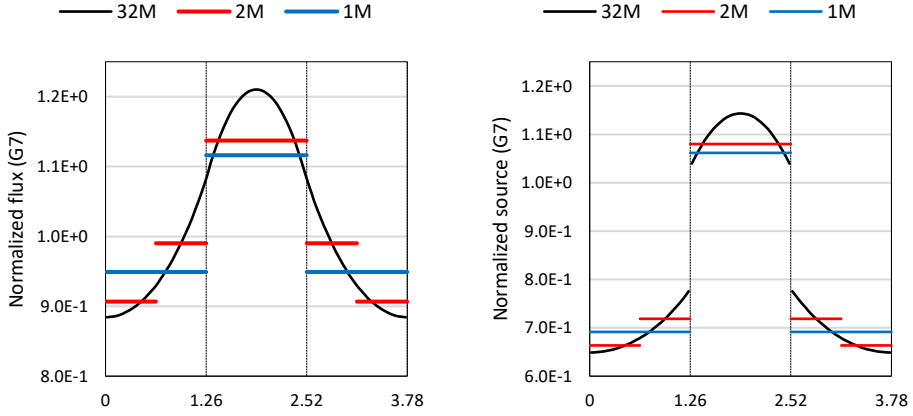


Figure 2.28. G7 scalar flux (left) and source (right) distributions obtained by the S_2 calculations based on the short characteristics

The results are presented with more detail in **Table 2.11**. The number of meshes per pin is increased from 1 (1M) to 32 (32M), and the 32M results are the reference. The fuel pin-averaged flux ($\bar{\phi}_{UO_2}$) and the current (J^{Surf}) at the UX-WH interface at 1.26cm is not notably changed by the number of meshes. On the other hand, the sum of source driven term in the fuel pin (φ_{src,UO_2}) and the waterhole ($\varphi_{src,WH}$) should be noted. In order to obtain the two terms, the SD term is accumulated from 0 to 1.26cm position for φ_{src,UO_2} by following the direction of right partial current (J^+) while the SD term from 2.52 to 1.26cm position is accumulated for $\varphi_{src,WH}$ by

following the direction of left partial current (J^-). Based on the results, it is noted that the use of fewer number of mesh leads to underestimation of the source driven term and then the scalar flux. In case of the 1M, for example, the underestimations for φ_{src,UO_2} and J^+ are 4.5% and 4.3% while those for $\varphi_{src,WH}$ and J^- are 2.9% and 2.9%. Resultantly, the relative error of J^{Surf} is only about 2.1% while the 4.4% underestimation of the pin-averaged flux in the waterhole ($\bar{\phi}_{WH}$) is observed.

Table 2.11. Results of the S₂ SC calculations for the three-pin problem with the different mesh options (for G7)

	32M	16M	8M	4M	2M	1M
$\bar{\phi}_{UO_2}$	9.472E-1	9.473E-1	9.473E-1	9.476E-1	9.484E-1	9.491E-1
Rel. Err.		0.00%	0.01%	0.04%	0.12%	0.20%
J^{Surf}	-7.679E-2	-7.680E-2	-7.687E-2	-7.711E-2	-7.778E-2	-7.837E-2
Rel. Err.		0.02%	0.11%	0.43%	1.29%	2.06%
φ_{src,UO_2}	6.983E-1	6.981E-1	6.973E-1	6.942E-1	6.844E-1	6.665E-1
Rel. Err.		-0.03%	-0.15%	-0.59%	-1.99%	-4.54%
J^+	2.740E-1	2.739E-1	2.736E-1	2.725E-1	2.688E-1	2.623E-1
Rel. Err.		-0.03%	-0.14%	-0.56%	-1.88%	-4.26%
$\varphi_{src,WH}$	1.071E+0	1.071E+0	1.070E+0	1.067E+0	1.058E+0	1.040E+0
Rel. Err.		-0.02%	-0.08%	-0.34%	-1.18%	-2.86%
J^-	3.508E-1	3.507E-1	3.505E-1	3.496E-1	3.466E-1	3.407E-1
Rel. Err.		-0.02%	-0.08%	-0.34%	-1.19%	-2.88%
$\bar{\phi}_{WH}$	1.168E+0	1.167E+0	1.165E+0	1.158E+0	1.137E+0	1.116E+0
Rel. Err.		-0.04%	-0.22%	-0.85%	-2.62%	-4.42%

Noting that the error cancellation is involved in the diffusion-like calculations, the total error due to the transport and discretization errors is also observed. In that the two errors determined by a specific solver are simultaneously corrected by the SPH factors, the investigation for the overall effect is inevitable. The diffusion and SP₃ FDM and the S₈ DD calculations were performed with various mesh sizes. The core PHXSs were employed without the SPH factors, and the results were compared with

the pin-homogenized MOC reference.

Figure 2.29 shows the selected results from the 4G and 8G comparisons for the ARO core. The ARI results are essentially similar with the ARO, but the magnitude of the errors is larger. In that the difference between the 8G and 16G results is relatively smaller than that between the 4G and 8G results and the dependence of the errors to the number of energy group and mesh size is similar, the 16G results are not presented. On the other hand, **Table 2.12** presents the summary of the 8G results and the contribution from the two error sources for each solver.

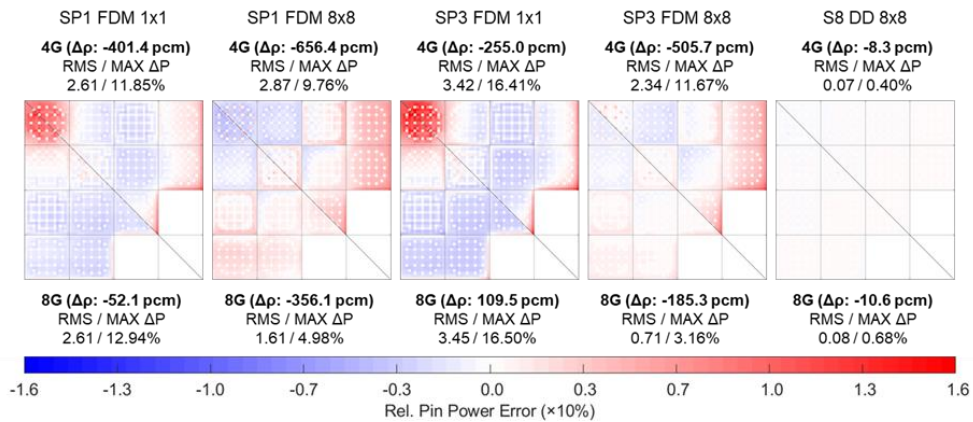


Figure 2.29. Relative pin power error (%) distributions due to the two errors determined by selected solvers for the KAIST 1A ARO core calculations

In **Figure 2.29**, it is first noted that the S_8 8x8 DD yielded the smallest errors regardless of the number of energy groups due to its accuracy in representation of the transport effect and flux gradient. For the pin power error, it is followed by the SP_3 8x8 FDM in that the RMS/MAX Rel. pin ΔP are 2.3%/11.7% for the 4G and 0.7%/3.2% for the 8G. It is clearly noted by **Table 2.12** that the reduction of the transport error with more energy group improves the results, since the discretization error for the RMS/MAX Rel. pin ΔP is merely 0.1%/0.5%. In case of the SP_3 1x1 FDM with the severe discretization error, in contrast, the use of more energy group rather increases the pin ΔP by weakening the error cancellation. It is also noted that the diffusion results behave similar with the SP_3 but the larger transport error results

in somewhat notable differences of the apparent errors. The results show that a rigorous transport approximation should be combined with an elaborated spatial discretization method, in order to guarantee accurate and reliable core calculation results by reducing the error cancellation.

Table 2.12. Total errors and contributions of the two error sources obtained from the 8G KAIST 1A ARO core calculations with the specific solvers

Solver	Diffusion FDM		SP ₃ FDM		S ₈ DD
	1x1	8x8	1x1	8x8	8x8
Trans. Err. (pcm) (RMS/MAX ΔP %)	-362.9 (1.7 / 5.3)		-193.9 (0.8 / 3.1)		-9.8 (0.1 / 0.6)
Disc. Err. (pcm) (RMS/MAX ΔP %)	310.8 (4.0 / 19.3)	6.7 (0.1 / 0.4)	303.4 (4.0 / 18.8)	8.6 (0.1 / 0.5)	-0.8 (0.0 / 0.1)
Total Err. (pcm) (RMS/MAX ΔP %)	-52.1 (2.6 / 12.9)	-356.1 (1.6 / 5.0)	109.5 (3.5 / 16.5)	-85.3 (0.7 / 3.2)	-10.6 (0.1 / 0.7)

2.3.2. Employment of the SENM for the SP_N equation

The results in the previous chapter show the need for the refined meshes, however, the computing burden for the FM FDM core calculations is too demanding. In this regard, the SENM nodal solver which is originally developed for the assemblywise diffusion calculation [51] is adapted to the PHMGCs employing the SP_N theory. The SENM approximates the moment distributions using the hyperbolic functions and Legendre polynomials as the basis functions so that the possible fluctuation of the higher moment due to the 4th order polynomial expression can be prevented.

The SP₃ SENM formulation was previously derived Jeong [52] but it is considered less appropriate for the GPU-specific pinwise nodal code because of the computing burden, complexity of the similarity transformation, and parallel efficiency. Instead, the one-node formulation is determined in order to take advantage of the inherent

parallelism in the GPU-accelerated core calculation. In this chapter, the one-node SP₃ SENM kernel is formulated and the test calculation results for the C5G7 1D pin array and VERA 2D FAs which are intended to demonstrate the accuracy in terms of the discretization error are presented.

(1) Formulation of the one-node SP₃ SENM kernel

The SP₃ equation can be written for the summed flux and the 2nd moment as:

$$\begin{aligned} -D_{0,g} \nabla^2 \hat{\phi}_{0,g} + \Sigma_{r0,g} \hat{\phi}_{0,g} &= s_{0,g} \\ -D_{2,g} \nabla^2 \phi_{2,g} + \Sigma_{r2,g} \phi_{2,g} &= s_{2,g} \end{aligned} \quad (2.17)$$

where

$$\begin{aligned} \hat{\phi}_{0,g} &= \phi_{0,g} + 2\phi_{2,g}, \\ D_{0,g} &= \frac{1}{3\Sigma_{tr,g}}, \quad D_{2,g} = \frac{3}{7\Sigma_{t,g}}, \quad \Sigma_{r0,g} = \Sigma_{r,g}, \quad \Sigma_{r2,g} = \frac{4}{3}\Sigma_{r,g} + \frac{5}{3}\Sigma_{t,g}, \\ q_{0,g} &= \frac{\chi_g}{k_{eff}} \sum_{g'=1} \nu \Sigma_{f,g} \phi_{0,g'} + \sum_{g' \neq g} \Sigma_{g' \rightarrow g} \phi_{0,g'}, \\ s_{0,g} &= q_{0,g} + 2\Sigma_{r,g} \phi_{2,g}, \quad \text{and} \quad s_{2,g} = -\frac{2}{3}q_{0,g} + \frac{2}{3}\Sigma_{r,g} \hat{\phi}_{0,g}. \end{aligned}$$

Each of the moment equation is decoupled by arranging the off-diagonal reaction terms to the sources in the right-hand-side (RHS). It would be worthwhile to note that not the scalar flux but the summed flux is added to the 2nd moment source term for stability of the higher moment calculation.

Hereinafter, only the summed flux equation is discussed since the two moment equations share the same form. By applying the transverse integration to the moment equations for the u-direction and normalizing it for the coordinate variable ξ_u defined in [-1, 1], the equation is written as:

$$\left(-\frac{4D_0}{h_u^2} \frac{d^2}{d\xi_u^2} + \Sigma_r \right) \hat{\phi}_0(\xi_u) = s_0(\xi_u) - L(\xi_u) \quad (2.18)$$

where the h_u is the node width and the L denotes the transverse leakage externally given as the quadratic polynomial. The group index g is dropped for simplicity. In the SENM, the entire RHS is approximated by the N -th order polynomial as:

$$Q(\xi_u) = s_0(\xi_u) - L(\xi_u) = \sum_{i=0}^N q_{0,i}^u P_i(\xi_u) \quad (2.19)$$

and Legendre polynomials are employed for the basis. N is 2 for pin size nodes and 4 for assembly size nodes because the higher order source expansion is beneficial for the accuracy of flux approximation within large nodes but it degenerates the stability when the node size is small. Therefore, the quadratic and the quartic source expansion is applied for the radial and the axial directions in the 3D calculation.

The source expansion coefficient ($q_{0,i}^u$) is used to determine the analytic solution of Eq. (2.18) given as:

$$\begin{aligned} \hat{\phi}_0(\xi_u) &= \hat{\phi}_0^H(\xi_u) + \hat{\phi}_0^P(\xi_u) \\ &= A_0^u \sinh(\kappa_0^u \xi_u) + B_0^u \cosh(\kappa_0^u \xi_u) + \sum_{i=0}^N c_{0,i}^u P_i(\xi_u) \\ &= \hat{\phi}_0 + A_0^u \sinh(\kappa_0^u \xi_u) + B_0^u \left(\cosh(\kappa_0^u \xi_u) - \frac{\sinh(\kappa_0^u)}{\kappa_0^u} \right) \\ &\quad + \sum_{i=1}^N c_{0,i}^u P_i(\xi_u) \end{aligned} \quad (2.20)$$

The superscript H and P denote the homogeneous and particular solutions, and

$$\hat{\phi}_0 = \frac{1}{2} \int_{-1}^1 \hat{\phi}_0(\xi_u) d\xi_u, \quad \kappa_0^u = \frac{h_u}{2} \sqrt{\frac{\Sigma_{r0}}{D_0}}, \quad \text{and} \quad \kappa_0^2 = \frac{h_u}{2} \sqrt{\frac{\Sigma_{r2}}{D_2}}.$$

The particular solution coefficients ($c_{0,i}$) are determined by using the method of undetermined coefficients as:

$$\begin{aligned}
c_{0,1} &= \frac{1}{\Sigma_{r0}} \left(q_{0,1} + \frac{15}{\kappa_0^2} q_{0,3} \right), & c_{0,3} &= \frac{q_{0,3}}{\Sigma_{r0}}, \\
c_{0,2} &= \frac{1}{\Sigma_{r0}} \left(q_{0,2} + \frac{35}{\kappa_0^2} q_{0,4} \right), & c_{0,4} &= \frac{q_{0,4}}{\Sigma_{r0}}.
\end{aligned} \tag{2.21}$$

The u is dropped for simplicity. $c_{0,0}$ is not obtained from $q_{0,i}$ because the node-averaged moments should be considered as unknown.

After the homogeneous solution as well as the particular solution is obtained, $q_{0,i}$ is approximated by the polynomial as:

$$\hat{\phi}_0(\xi_u) \cong \hat{\phi}_0 + \sum_{i=1}^N a_{0,i}^u P_i(\xi_u) \tag{2.22}$$

and the flux coefficients ($a_{0,i}^u$) are obtained by using the orthogonal property of Legendre polynomials, as detailed by Yoon [51].

For convenience of the derivation, the partial odd moments at each surface are approximated as detailed first by Lee [12] and then PARCS theory manual [50]. In the SP₃ theory, the partial odd moments at the surface are defined in terms of the even moments and the net moment as:

$$J_1^\pm = \frac{1}{4} \hat{\phi}_0^s \pm \frac{1}{2} J_1 - \frac{3}{16} \phi_2^s, \quad J_3^\pm = \frac{7}{16} \phi_2^s \pm \frac{1}{2} J_3 - \frac{1}{16} \hat{\phi}_0^s. \tag{2.23}$$

The 2nd moment in the partial 1st moment equation and the summed flux in the partial 3rd moment render difficulty in the formulation. Therefore, Eq. (2.23) is approximated by truncation as:

$$\tilde{J}_1^\pm = \frac{1}{4} \hat{\phi}_0^s \pm \frac{1}{2} J_1, \quad \tilde{J}_3^\pm = \frac{7}{16} \phi_2^s \pm \frac{1}{2} J_3. \tag{2.24}$$

It would be called as the approximated partial moment, contrast to the exact form in Eq. (2.23). Note that Eq. (2.23) and Eq. (2.24) yield the same net moment, and

their incoming values at the reflective boundary is the same with the outgoing. However, it should be aware that the vacuum BC arises difference. For the boundary where the incoming moments are zero, the approximated moments are:

$$\tilde{J}_1^- = \frac{3}{109}(\tilde{J}_1^+ + 8\tilde{J}_3^+), \quad \tilde{J}_3^- = \frac{1}{109}(14\tilde{J}_1^+ + 3\tilde{J}_3^+). \quad (2.25)$$

In Eq. (2.24), fraction of the surface even moment can be arbitrary and it has only a negligible effect on the converged solution. Therefore, with f_1 and f_3 for the 1st and 3rd approximated partial moment, Eq. (2.25) can be generalized as:

$$\tilde{J}_1^- = f_{11}\tilde{J}_1^+ + f_{13}\tilde{J}_3^+, \quad \tilde{J}_3^- = f_{31}\tilde{J}_1^+ + f_{33}\tilde{J}_3^+. \quad (2.26)$$

where

$$\begin{aligned} f_{11} &= -\frac{1}{f_d}(25 - 112f_1 + 64f_3 - 256f_1f_3), & f_{13} &= \frac{96f_1}{f_d}, \\ f_{31} &= \frac{32f_3}{f_d}, & f_{33} &= -\frac{1}{f_d}(25 + 112f_1 - 64f_3 - 256f_1f_3), \\ & \text{and } f_d &= 25 + 112f_1 + 64f_3 + 256f_1f_3 \end{aligned}$$

The homogeneous coefficients, A and B , for either the summed flux or the 2nd moment is derived for the arbitrary fractions. At the right and the left boundaries of the target node, the approximated incoming partial moments are:

$$\tilde{J}_{in}^r = f\phi(1) - \frac{1}{2}J(1), \quad \tilde{J}_{in}^l = f\phi(-1) + \frac{1}{2}J(-1). \quad (2.27)$$

and the net surface moment can be defined as:

$$\begin{aligned} J &= -\frac{2D}{h} \frac{d}{d\xi} \phi(\xi) = -2\beta k (A \cosh(\kappa\xi) + B \sinh(\kappa\xi)) + J^P(\xi). \\ J^P(\xi) &= -\frac{2D}{h} \frac{d}{d\xi} \phi^P(\xi) = -2\beta \sum_{i=1}^N c_i P_i'(\xi). \end{aligned} \quad (2.28)$$

By inserting Eq. (2.27) in Eq. (2.28), the homogeneous coefficients are:

$$\begin{aligned}
 A &= \frac{\frac{1}{2}(\tilde{J}_{in}^r - \tilde{J}_{in}^l) - (f + \beta)c_1 - (f + 6\beta)c_3}{\beta k \cosh(\kappa) + f \sinh(\kappa)}, \\
 B &= \frac{-f\bar{\phi} + \frac{1}{2}(\tilde{J}_{in}^r + \tilde{J}_{in}^l) - (f + 3\beta)c_2 - (f + 10\beta)c_4}{\beta \kappa \sinh(\kappa) + f \left(\cosh(\kappa) - \frac{\sinh(\kappa)}{\kappa} \right)}.
 \end{aligned} \tag{2.29}$$

It should be noted that c_3 and c_4 are zero for the radial direction, and A can be readily determined by the given incoming moments and the particular solution coefficients. On the other hand, the node average moment ($\bar{\phi}$) must be obtained in order to determine B . By using Eq. (2.28), the multidimensional nodal balance equation is written as:

$$\begin{aligned}
 \sum_{u=x,y,z} \frac{J_u(1) - J_u(-1)}{h_u} + \Sigma_r \bar{\phi} &= \bar{s}, \\
 \frac{J_u(1) - J_u(-1)}{h_u} &= -\Sigma_D^u \left(\kappa^u \sinh(\kappa^u) B + 3c_2^u + 10c_4^u \right), \\
 \Sigma_D^u &\equiv \frac{4\beta}{h_u} = \frac{4D}{h_u^2}.
 \end{aligned} \tag{2.30}$$

Eq. (2.30) is rearranged as:

$$\bar{\phi} = \frac{\bar{s} + C}{\Sigma_r + \sum_{u=x,y,z} \Sigma_D^u f \tau^u} \tag{2.31}$$

where

$$\begin{aligned}
 C &= \sum_{u=x,y,z} \Sigma_D^u \left(\frac{1}{2} \tau^u (J_{in}^{u,l} + J_{in}^{u,r}) + (3 - \tau^u (f + 3\beta^u)) \right) c_2^u + (10 - \tau^u (f + 10\beta^u)) c_4^u, \\
 \tau^u &= \frac{\kappa^u \sinh(\kappa^u)}{\beta^u \kappa^u \sinh(\kappa^u) + f \left(\cosh(\kappa^u) - \frac{\sinh(\kappa^u)}{\kappa^u} \right)}.
 \end{aligned}$$

Finally, the approximated outgoing moments are:

$$\begin{aligned} \begin{bmatrix} \tilde{J}_{out}^r \\ \tilde{J}_{out}^l \end{bmatrix} &= \begin{bmatrix} f\phi(1) + \frac{1}{2}J(1) \\ f\phi(-1) - \frac{1}{2}J(-1) \end{bmatrix} \\ &= \begin{bmatrix} \alpha_s & \alpha_c \\ -\alpha_s & \alpha_c \end{bmatrix} \begin{bmatrix} A \\ B \end{bmatrix} + \begin{bmatrix} f(\bar{\phi} + \phi^P(1)) + \frac{1}{2}J^P(1) \\ f(\bar{\phi} + \phi^P(-1)) - \frac{1}{2}J^P(-1) \end{bmatrix} \end{aligned} \quad (2.32)$$

Here,

$$\begin{aligned} \alpha_s &= -\beta\kappa \cosh(\kappa) + f \sinh(\kappa), \\ \alpha_c &= -\beta\kappa \sinh(\kappa) + f \left(\cosh(\kappa) - \frac{\sinh(\kappa)}{\kappa} \right). \end{aligned}$$

(2) Accuracy of the SP₃ SENM solver

In order to demonstrate the accuracy of the SENM solver for the SP₃ equation, a test calculation was performed for the C5G7 1D pin array given in **Figure 2.8**. The same 7G PHXSs were used, and the SP₃ FDM calculations based on 4 (4M), 8 (8M), and 64 (64M) meshes per pin were also performed for the comparison. The FDM 64M results are taken as the reference.

Figure 2.30 presents the scalar flux and the 2nd angular moment distributions for G7 where the steepest flux gradients are observed. The SENM faithfully represents the flux gradient especially severe at around the GT pin-cells and the fuel-reflector interface without a nonphysical fluctuation due to the use of the hyperbolic functions. Compared to the reference, the resulting $\Delta\rho$ error is less than 1 pcm. Note that the $\Delta\rho$ errors of FDM 4M and 8M are -73 and -19 pcm, respectively.

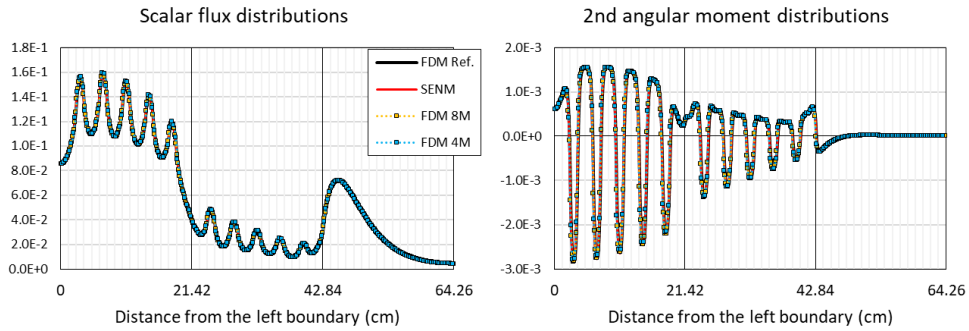


Figure 2.30. G7 scalar flux and the 2nd angular moment distributions for the C5G7 1D pin array obtained from the SP₃ FDM and SENM calculations

The VERA 2D FA calculations with the SP₃ FDM and SENM solvers were then performed. The 17x17 FA specifications were taken from the VERA problem 2, and descriptions of the selected FAs are given in **Table 2.13**. The 8G PHXSs were obtained by the 47G heterogeneous lattice calculations with nTRACER.

Table 2.13. Descriptions of the selected VERA 2D FAs

ID	Enrichment	Descriptions
G	3.1%	24 Ag-In-Cd control rods
H	3.1%	24 B ₄ C control rods
K	3.6% + 3.1%	Radial zoning + 24 Pyrex
N	3.1%	104 IFBA + 20 WABA
O	3.1%	12 Gadolinia
P	3.1%	24 Gadolinia

Table 2.14 presents the $\Delta\rho$ error due to the discretization. The reference is the SP₃ FM FDM result based on 64x64 meshes per pin. Because of the severe heterogeneity originates from CRs and BAs, the FDM shows large error. In case of the H FA, for example, the error is about 9021 pcm with the 1x1 and 3430 pcm with the 2x2 meshes. On the other hand, the SENM yielded about 216 pcm of $\Delta\rho$. It is even better than the FM FDM with 8x8 meshes per pin.

Table 2.14. Discretization error in the reactivity (pcm) obtained by the SP₃ FDM and SENM calculations for the VERA 2D FAs

ID	Ref.	FDM			SENM
		1x1	2x2	8x8	
G	0.817349	6350.3	2399.1	200.6	138.9
H	0.748805	9020.7	3430.2	288.2	216.0
K	1.008013	1863.4	668.3	53.3	29.2
N	0.862269	1370.0	461.6	35.0	7.7
O	1.032027	2035.5	827.5	75.8	29.5
P	0.900619	4647.9	1900.6	176.2	84.3

The FAs were also used to confirm that the quartic source expansion is not needed when the node size is small. The SP₃ SENM calculations were performed with the 2nd and the 4th order source expansion options. Each pin-cell was subdivided in order to show the instability originates from the higher source expansion within small nodes. The FM FDM results are taken as the reference.

It would be worthwhile to note that the instability can be explained by employing Eq. (2.29). When the diffusivity (β) becomes too large due to small node size, the homogeneous solution coefficients (A, B) are directly determined by the particular solution coefficients (c_i) which are obtained from the source coefficients (q_i) and severely fluctuating until the calculation is converged. It conflicts to the physics that the leakage effect is more remarkable in small mesh.

The SENM results based on various mesh size are summarized in **Table 2.15**. N/A indicates that the calculation is diverged so that no data exists. Regardless of the assembly configuration, the difference between the 2nd order and the 4th source expansion cases is negligibly small.

Lastly, the SP₃ SENM calculations were performed for the KAIST1A cores. The SP₃ FM FDM results based on 16x16 meshes per pin were taken as the reference, and the SENM results agreed well. For example, the $\Delta\rho$ and the RMS/MAX Rel. pin ΔP errors yielded by the 8G SP3 SENM are about 21 pcm and 0.2%/0.4%, while

those of the SP₃ FDM based on the 8x8 meshes are 41 pcm and 0.3%/0.8%.

Table 2.15. Discretization error of the reactivity (pcm) obtained by the SP3 SENM calculations for the VERA 2D FAs with the different source expansion orders

ID	Case	1x1	2x2	4x4
G	2nd	138.9	54.3	14.4
	4th	138.1	54.1	N/A
	Diff.	0.8	0.2	N/A
H	2nd	216.0	94.9	26.4
	4th	215.0	94.7	N/A
	Diff.	1.0	0.2	N/A
K	2nd	29.2	5.7	1.0
	4th	29.0	5.7	N/A
	Diff.	0.2	0.0	N/A
N	2nd	7.7	2.9	0.8
	4th	7.6	2.9	N/A
	Diff.	0.1	0.0	N/A
O	2nd	29.5	14.5	4.4
	4th	28.6	14.3	N/A
	Diff.	0.9	0.2	N/A
P	2nd	84.3	34.6	10.5
	4th	82.3	33.9	N/A
	Diff.	2.0	0.7	N/A

(3) Application of the SENM kernel for the SP₅ core calculation

Noting the accuracy of the SP₃ SENM solver, the one-node SENM kernel for the SP₅ calculation is derived for further investigation. Similar to Eq. (2.17), the SP₅ equation can be written as:

$$\begin{aligned}
 -D_{0,g} \nabla^2 \hat{\phi}_{0,g} + \Sigma_{r0,g} \hat{\phi}_{0,g} &= s_{0,g} \\
 -D_{2,g} \nabla^2 \hat{\phi}_{2,g} + \Sigma_{r2,g} \hat{\phi}_{2,g} &= s_{2,g} \\
 -D_{4,g} \nabla^2 \phi_{4,g} + \Sigma_{r4,g} \phi_{4,g} &= s_{4,g}
 \end{aligned} \tag{2.33}$$

where

$$\begin{aligned}
 \hat{\phi}_{0,g} &= \phi_{0,g} + 2\phi_{2,g}, & \hat{\phi}_{2,g} &= \phi_{2,g} + \frac{4}{3}\phi_{4,g}, \\
 D_{0,g} &= \frac{1}{3\Sigma_{tr,g}}, & D_{2,g} &= \frac{3}{7\Sigma_{t,g}}, & D_{4,g} &= \frac{5}{11\Sigma_{t,g}}, \\
 \Sigma_{r0,g} &= \Sigma_{r,g}, & \Sigma_{r2,g} &= \frac{4}{3}\Sigma_{r,g} + \frac{5}{3}\Sigma_{t,g}, & \Sigma_{r4,g} &= \frac{64}{45}\Sigma_{r,g} + \frac{161}{45}\Sigma_{t,g}, \\
 q_{0,g} &= \frac{\chi_g}{k_{eff}} \sum_{g'=1} \nu \Sigma_{f,g} \phi_{0,g'} + \sum_{g' \neq g} \Sigma_{g' \rightarrow g} \phi_{0,g'}, \\
 s_{0,g} &= q_{0,g} + 2\Sigma_{r0,g} \hat{\phi}_{2,g} - \frac{8}{3}\Sigma_{r0,g} \phi_{4,g}, \\
 s_{2,g} &= -\frac{2}{3}q_{0,g} + \frac{2}{3}\Sigma_{r0,g} \hat{\phi}_{0,g} + \frac{4}{3}\Sigma_{r2,g} \phi_{4,g}, \\
 \text{and } s_{4,g} &= \frac{8}{15}q_{0,g} - \frac{8}{15}\Sigma_{r0,g} \hat{\phi}_{0,g} + \frac{4}{5}\Sigma_{r2,g} \hat{\phi}_{2,g}.
 \end{aligned} \tag{2.34}$$

The even moment equations are decoupled with each other so that those can be solved as the SP₃ equations. The only difference is representation of the partial odd moments and the vacuum BC. The partial moments up to the 5th order are written in terms of the even moments and the net odd moment as:

$$\begin{aligned}
J_1^\pm &= \frac{1}{4}\hat{\phi}_0^s \pm \frac{1}{2}J_1 - \frac{3}{16}\hat{\phi}_2^s + \frac{5}{32}\phi_4^s, \\
J_3^\pm &= \frac{7}{16}\hat{\phi}_2^s \pm \frac{1}{2}J_3 - \frac{1}{16}\hat{\phi}_0^s - \frac{205}{768}\phi_4^s, \\
J_5^\pm &= \frac{407}{768}\phi_4^s \pm \frac{1}{2}J_5 + \frac{1}{32}\hat{\phi}_0^s - \frac{41}{256}\hat{\phi}_2^s.
\end{aligned} \tag{2.35}$$

Therefore, likewise Eq. (2.24), the approximated partial moments are defined by the truncated form of Eq. (2.35) as:

$$\tilde{J}_1^\pm = \frac{1}{4}\hat{\phi}_0^s \pm \frac{1}{2}J_1, \quad \tilde{J}_3^\pm = \frac{7}{16}\hat{\phi}_2^s \pm \frac{1}{2}J_3, \quad \tilde{J}_5^\pm = \frac{407}{768}\phi_4^s \pm \frac{1}{2}J_5. \tag{2.36}$$

At the reflective boundary, the incoming approximated partial moment is the same as the outgoing. At the vacuum boundary where the real incoming partial moments are zero, however, the incoming approximated partial moments are nonzero and those can be obtained with the outgoing approximated partial moments as:

$$\tilde{J}_n^- = f_{n1}\tilde{J}_1^+ + f_{n3}\tilde{J}_3^+ + f_{n5}\tilde{J}_5^+, \tag{2.37}$$

with $n = 1, 3, \text{ and } 5$, and the coefficients f_{n1} , f_{n3} , and f_{n5} are defined as:

$$\begin{aligned}
f_{11} &= -\frac{1}{f_d} \left(\begin{array}{l} 33075 - 148716f_1 + 100352f_3 + 76800f_5 \\ -416768f_1f_3 - 344064f_1f_5 + 196608f_3f_5 - 786432f_1f_3f_5 \end{array} \right), \\
f_{13} &= -\frac{1}{f_d} (-116928f_1 - 294912f_1f_5), \quad f_{15} = -\frac{1}{f_d} (28800f_1 + 245760f_1f_3) \\
f_{31} &= -\frac{1}{f_d} (-38976f_3 - 98304f_3f_5), \\
f_{33} &= -\frac{1}{f_d} \left(\begin{array}{l} 33075 + 148716f_1 - 100352f_3 + 76800f_5 \\ -416768f_1f_3 + 344064f_1f_5 + 196608f_3f_5 - 786432f_1f_3f_5 \end{array} \right), \\
f_{35} &= -\frac{1}{f_d} (-89600f_3 - 419840f_1f_3),
\end{aligned}$$

$$f_{51} = -\frac{1}{f_d}(5760f_5 + 49152f_3f_5), \quad f_{53} = -\frac{1}{f_d}(-53760f_5 - 251904f_1f_5),$$

$$f_{55} = -\frac{1}{f_d} \left(33075 + 148716f_1 + 100352f_3 - 76800f_5 \right. \\ \left. + 416768f_1f_3 - 344064f_1f_5 - 196608f_3f_5 - 786432f_1f_3f_5 \right),$$

and $f_d = 33075 + 148716f_1 + 100352f_3 + 76800f_5$
 $+ 416768f_1f_3 + 344064f_1f_5 + 196608f_3f_5 + 786432f_1f_3f_5$

where f_1 , f_3 , and f_5 are the numbers used to determine the approximated partial moments. In Eq. (2.36), for example, $f_1 = 1/4$ for \tilde{J}_1^\pm , $f_3 = 7/16$ for \tilde{J}_3^\pm , and $f_5 = 407/768$ for \tilde{J}_5^\pm , but arbitrary numbers can be employed instead.

Note that the SP₅ SENM solver derived here is employed for the KAIST 1A and AP1000 PWR core calculations with the SPH factor in a preliminary study [30]. However, the difference between the SP₃ and SP₅ SENM results are small to neglect, within about 1 pcm for the $\Delta\rho$ and 0.1% for the MAX pin ΔP for the 8G calculations. It is also noted in **Chapter 4**.

2.3.3. Inconsistency of the SPH Factors due to the Solution Methods

In order to show that the inconsistency of the SA based SPH factor in the core can be reduced by the use of the optimal solution method, further investigations for the SPH factors were performed. The analysis detailed in this chapter is mainly focused on the intra-assembly distribution shapes of the pinwise SPH factors. It is because the deviation of the flux weighted AA-SPH can be considered well by assemblywise corrections including the improved SPH method [16] and the Selengut normalization method [49] but the distortion of the distribution shape is not.

The KAIST 1A ARI core was selected for the target problem and the core SPH factor sets were obtained with various solvers and compared with the corresponding SA SPH factors. Since the flux-weighted AA-SPH based on the core fluxes and SPH factors (CF-AA-SPH) deviates from unity while the SA based AA-SPH (SA-AA-SPH) is set to unity during the SPH generation [49], the core SPH factors are divided by the CF-AA-SPH for each assembly and energy group the normalization. Then the normalized core SPH factors were compared with the corresponding SA SPH factors. The CF-AA-SPH and the relative difference of the normalized core SPH factor to the corresponding SA SPH factor are:

$$\bar{\mu}_G^{Core} = \frac{\sum_{i \in Asy} \mu_{G,i}^{Core} \bar{\phi}_{G,i}^{Hom-Core} V_i}{\sum_{i \in Asy} \bar{\phi}_{G,i}^{Hom-Core} V_i}, \quad \Delta\mu_{G,i} = \frac{\mu_{G,i}^{Core} / \bar{\mu}_G^{Core} - \mu_{G,i}^{SA}}{\mu_{G,i}^{SA}} \quad (2.38)$$

where i is the pin index within the target assembly; G is the group index; $\Delta\mu$ is the relative difference of the normalized core SPH factor; and the superscript *Hom-Core* means the fluxes are taken from the pin-homogenized core calculation.

The RMS and MAX of $\Delta\mu$ for each group of the 8G are given in **Table 2.16**. Here *SA ONLY* indicates that the SA based SPH factor set is applied to all FAs. The diffusion and SP₃ solvers combined with FDM and SENM and the S₈ FM DD solver are used to obtain the SPH factors. The various cases are to examine the dependence

of the inconsistency on the transport approximations and the spatial discretization methods. In the table, the diffusion results are denoted by SP₁ for convenience, and G3 and G8 where the flux levels are highest in the fast and thermal ranges are emphasized in bold. The SENM results are essentially similar with the 8x8 FDM results so that the diffusion SENM results are not presented.

Table 2.16. Relative difference (%) of the normalized core SPH factors to the SA SPH factors for each group of the 8G obtained from the KAIST 1A ARI core (SA ONLY)

Solver	Error	G1	G2	G3	G4	G5	G6	G7	G8
SP1 FDM 1x1	RMS	1.64	1.07	0.51	1.13	0.19	0.42	0.58	0.95
	MAX	7.58	4.85	3.71	4.26	0.88	1.75	2.87	4.49
FDM 8x8	RMS	1.64	1.09	0.53	1.10	0.20	0.47	0.65	1.14
	MAX	7.54	4.93	3.80	4.13	0.84	1.75	2.61	4.62
SP3 FDM 1x1	RMS	0.53	0.36	0.34	1.20	0.17	0.35	1.37	0.94
	MAX	2.08	1.86	2.26	4.59	0.76	1.77	8.10	3.28
FDM 8x8	RMS	0.61	0.47	0.34	1.16	0.17	0.25	0.52	0.79
	MAX	2.73	2.05	2.18	4.48	0.72	0.95	2.84	3.34
SENM	RMS	0.61	0.48	0.34	1.16	0.18	0.25	0.54	0.80
	MAX	2.79	2.05	2.17	4.41	0.75	0.91	2.82	3.34
S8 DD 8x8	RMS	1.03	1.05	1.83	0.25	0.28	0.29	1.22	2.94
	MAX	6.08	5.73	11.77	1.26	1.20	1.56	6.93	15.90

In addition, the radial $\Delta\mu$ distributions for G3 and G8 are presented in **Figure 2.31**. Normally the SPH factors based on SA configuration are applied to the peripheral FAs (PAs) as well as the internal FAs, however, a separate set of SPH factors can be generated for the PAs by using the fuel-reflector configurations shown in **Figure 2.3**. Both cases were examined in this section. Here *PA SPH* is the case where the PA SPH factor set are used for the PAs. Since it is noted in **Table 2.16** that the SP₃ FDM results based on 8x8 meshes per pin are nearly the same with the SP₃ SENM, less than 0.06% difference regardless of the energy group, only the SP₃ SENM results are given in the figure.

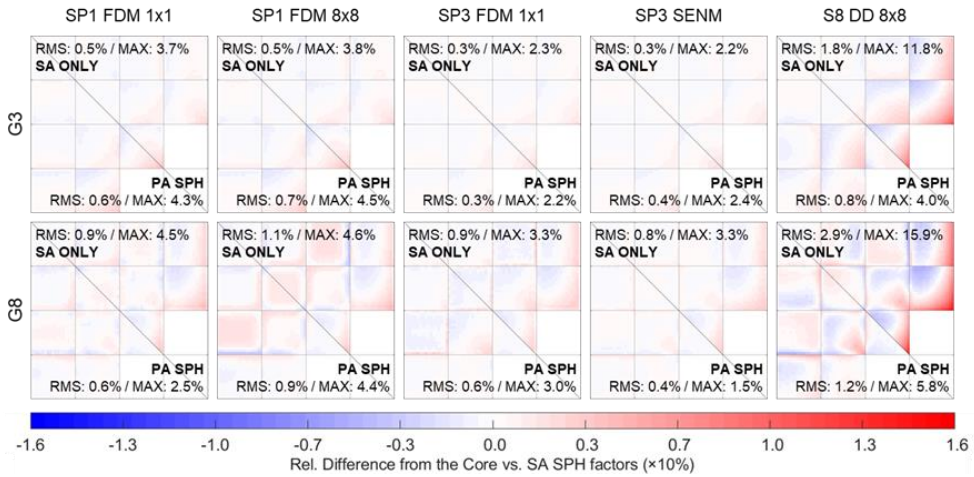


Figure 2.31. Relative difference (%) of the normalized core SPH factors to the SA SPH factors in G3 (top) and G8 (bottom) of the 8G for the KAIST 1A ARI core

From the table and **Figure 2.31**, it is revealed that the SP₃ SENM yields the smallest $\Delta\mu$ followed by the diffusion FDM with the 1x1 mesh. For G8, the MAX $\Delta\mu$ of the SP₃ SENM is about 3.3% for *SA ONLY* and 1.5% for *PA SPH* and those appear at the core periphery and the UO₂/MOX interfaces. Although the *SA ONLY* case shows non-negligible G8 $\Delta\mu$ in PAs, its effect is limited due to the low flux level. It is worthwhile to note that the SP₃ core calculation result is not notably affected by the use of *PA SPH* factor set. In this ARI case, the difference turns out to be less than about 5 pcm for $\Delta\rho$ and 0.3% for the MAX absolute (Abs.) pin ΔP errors. It means that the FM SP₃ solver can accurately reproduce the pinwise core fluxes with the SA SPH factor set, and the PA SPH factor set is not essential.

On the other hand, the diffusion 1x1 FDM results are similar to those of the SP₃ SENM. However, this is a mere consequence of the error cancellation between the transport and the discretization errors. For the G8 PA SPH results, for example, the diffusion 8x8 FDM and the SP₃ 1x1 FDM cases weaken the error cancellation by reducing only one of the transport or discretization errors so that the RMS $\Delta\mu$ rather increases from 0.9% to 1.1% for the diffusion 8x8 FDM and is not changed for the SP₃ 1x1 FDM. The two solvers show large $\Delta\mu$ at the assembly internal regions as well as the core periphery and the UO₂/MOX interfaces.

It is also noted that the S_8 8x8 DD yielded remarkably large $\Delta\mu$. For the *SA ONLY* cases, the MAX $\Delta\mu$ is observed in the PAs and it is about 11.8% for G3 and 15.9% for G8. Since the severe $\Delta\mu$ in the PAs is reduced by using the PA SPH factor set as shown in the *PA SPH* case, the S_N core calculation requires the PA SPH factor sets. However, large $\Delta\mu$ for the assembly boundary pins, which is nearly about 4.9% at the UO_2/MOX interface, still remains and the intra-assembly $\Delta\mu$ distributions are notably distorted. It implies that the significant $\Delta\mu$ cannot be mitigated by the aforementioned correction techniques which is to adjust AA-SPHs.

Noting that the severe distortion of the SPH factor distributions is observed from a simple problem, such as the EDGE type fuel-reflector problem, it is demonstrated that the distortion notably deteriorates the core calculation results. For the example, the 8G KAIST 1A ARO and ARI core calculation results are given in **Figure 2.32** and **Figure 2.33**. In addition to the SA and core SPH factor sets denoted by *Core SPH* and *SA SPH*, the *SA + Core* SPH factor sets were used with the SA PHXSs for the S_8 8x8 DD calculations. The *SA + Core* indicates that the core SPH factors are used for a part of the entire energy range. The fast (*F*), intermediate (*I*), and thermal (*T*) ranges correspond to G1 – 3, G4 – 6, and G7 – 8, respectively.

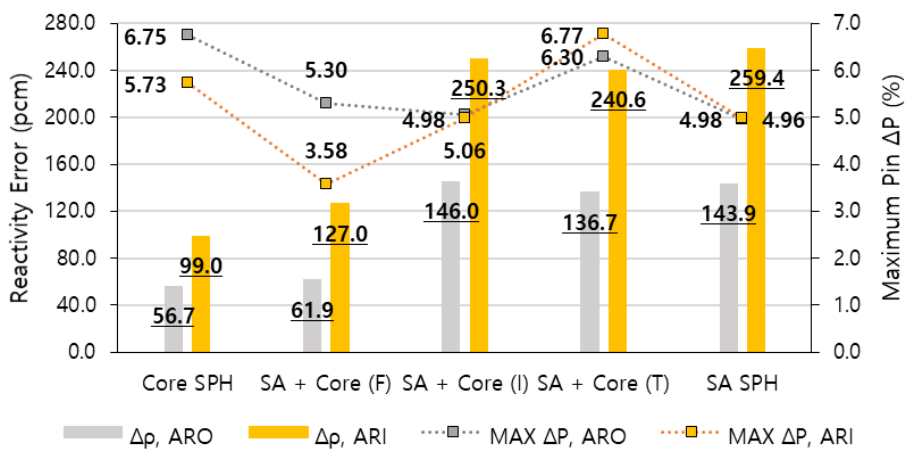


Figure 2.32. Reactivity and the maximum pin power errors for the KAIST 1A ARO and ARI core calculations with the SA PHXSs and the various SPH factor sets

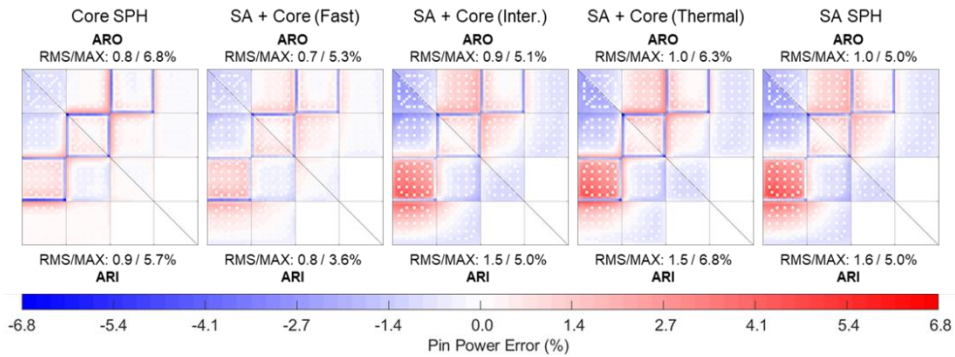


Figure 2.33. Radial pin power error (%) distributions for the KAIST 1A ARO and ARI core calculations with the SA PHXSs and the various SPH factor sets

As shown in the two figures, the *Core SPH* gives the lowest errors while the *SA SPH* gives the highest. Note that the errors appear in the *Core SPH* results originate from the spectral error of the SA PHXSs. The results clearly reveal that the fast group SPH factors have the largest effect on the core calculation results. In the ARI case, for example, the $\Delta\rho$ and RMS/MAX pin ΔP errors are 99 pcm and 0.9%/5.7% for the *Core SPH*, and those are followed by 127 pcm and 0.8%/3.6% for the *SA + Core (F)*. On the contrary, the *SA + Core (I)* and *SA + Core (T)* results are close to the *SA SPH* which shows 260 pcm of the $\Delta\rho$ and 1.6%/5.0% of the RMS/MAX pin ΔP .

The significant effect of the fast group SPH factors as well as the severe distortion is contrary to the SP_N calculations. As noted by Kozłowski [13], the fast group EFs have marginal effect on the diffusion-like calculations. The large impact of the fast group SPH factors and their sensitivity to the neighboring nodes raise an important limitation. Considering the long MFP of fast neutrons ranging an assembly pitch, it is hard to obtain the proper SPH factors for the S_N from SA configurations. Based on the analysis, it is concluded that the FM S_N solver is inadequate for the PHMGC. Thus the S_N core calculation results are not presented in **Chapter 4**.

Contrary to the S_N , the SP_3 SENM solver successfully resolve the inconsistency. **Table 2.17** and **Figure 2.34** present the results of the diffusion and SP_3 calculations with the core PHXSs and the SA SPH factors. In that the core PHXSs do not involve

the spectral error, the errors are resulted only by the inconsistency of the SPH factors. For the core calculations employing the diffusion and SP₃ FDM solvers taking a pin-cell as a mesh, which are employed for the core calculations in the previous studies, the RMS/MAX pin ΔP are 0.7%/4.6% and 1.1%/8.5%. For the diffusion calculations with better discretization methods, the MAX pin ΔP drops to 1.6% by the 2x2 FDM but increases again to 3.2% by the SENM because the reduction of the discretization error weakens the error cancellation. For the SP₃ calculations, on the other hand, the MAX pin ΔP drops to 2.7% by the 2x2 FDM and decreases to 1.1% by the SENM.

Table 2.17. Results of the 8G KAIST ARO core calculations with the core PHXSs and the SA SPH factors

Solver		$\Delta\rho$ (pcm)	Pin ΔP (%)	
			RMS	MAX
Diffusion	FDM 1x1	-10.1	0.71	4.59
	FDM 2x2	-11.1	0.55	1.55
	SENM	-11.1	0.71	3.19
SP3	FDM 1x1	17.2	1.12	8.51
	FDM 2x2	15.9	0.39	2.73
	SENM	15.6	0.23	1.07

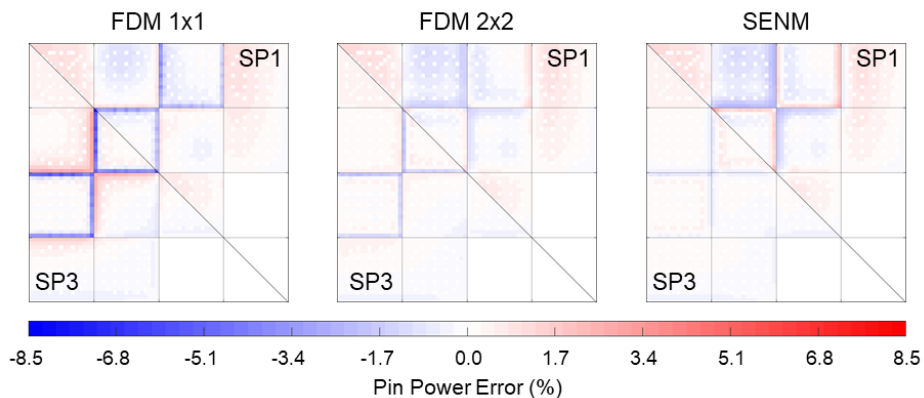


Figure 2.34. Radial pin power error (%) distributions obtained with the core PHXSs and the SA SPH factors

The analysis presented in this chapter demonstrates that the SP_3 SENM solver is the optimal solution method which can reduce the inconsistency of the SA based SPH factors in the core by minimizing the degree of the additional correction as much as practically possible. Compared to the SP_3 SENM, the diffusion solvers and the CM SP_3 FDM solver are significantly affected by the error cancellation which is depending on the core environment. In addition, the SP_5 calculation results are not notably different to the SP_3 and the S_N calculation yields the intolerable error due to the distortion of the SPH factors especially noted in the fast energy range.

Although the errors due to the SA SPH factors is successfully captured by the SP_3 SENM solver, however, the spectral error due to the SA based PHXSs still remains. In that the effect of the spectral error can be remarkable for core problems involving severe heterogeneity, the need for a leakage correction is raised. In the following **Chapter 3**, development and application of the pinwise LFM for the spectral leakage correction is presented in detail.

Chapter 3. Development of the Pinwise Leakage Feedback Method

In that the use of a sufficiently large number of energy groups is an effective way to reduce the spectral error, it had been regarded that the effect of the spectral error is small to neglect while the assemblywise few group calculations involve significant errors. However, the systematic analysis revealed that the spectral error due to the use of the SA based PHXSs can be notable for highly heterogeneous core problems, and it globally appears if the number of energy group is insufficient. Thus the pinwise leakage feedback method (LFM) is employed for the leakage correction of the SA PHXSs. It is based on the fact that the perturbation of the PHXS originates from the leakage effect introduced by the neighboring nodes in the core.

This chapter is to detail the pinwise LFM as the follows. **Chapter 3.1** presents the fundamentals of the method. Functionalization of the MG PHXSs to the leakage is rationalized and selection of the proper leakage parameters, namely the three group (3G) leakage to removal ratio (LTRR), is described. **Chapter 3.2** shows how the SPH factors are considered. Noting that the agreements of the CM diffusion and SP_3 calculations are not notably improved by the pinwise LFM due to the inconsistency of the SA SPH factors, correction of the SPH factors is examined. In that the leakage correction of the SPH factors deteriorate the convergence of the LFM iteration, the assemblywise DF (ADF) base on the partial current is employed. **Chapter 3.3** details the LFM coefficient generations for branch conditions.

3.1. Functionalization of PHXSs to Leakage Parameters

The LFM is originally developed for correction of the assemblywise few group XSs and it is adopted for PHMGCs. Based on the empirical correlation between the perturbed XSs and the leakage fraction (LF), Ban [25] functionalized the XSs to the LFs representing the fast and thermal energy ranges. The G-th group LF, which is renamed as the leakage to removal ratio (LTRR) in this work for clarification of the meaning, is defined as:

$$l_G = \frac{\sum_{s=1}^{N_{surf}} J_G^s A_s}{\int_V \Sigma_{r,G} \phi_G dV} = \frac{1}{\Sigma_{r,G} \phi_G} \left(\frac{\chi_G}{k_{eff}} \sum_{G'} v \Sigma_{f,G'} \phi_{G'} + \sum_{G' \neq G} \Sigma_{G' \rightarrow G} \phi_{G'} - \Sigma_{r,G} \phi_G \right). \quad (3.1)$$

The spectral index shift (SIS) is used as well for a special treatment for FAs at the core periphery, namely peripheral assembly treatment (PAT). The SIS is defined as:

$$\Delta\Gamma = \frac{\phi_1}{\phi_2} - \frac{\phi_1^{SA}}{\phi_2^{SA}}, \quad (3.2)$$

where ϕ_1 and ϕ_2 are the fluxes in the fast and thermal energy groups of the 2G structure. Because the spectral index (SI) can be derived from the thermal neutron balance equation as Eq. (3.3) and the down scattering XS ($\Sigma_{1 \rightarrow 2}$) is written as Eq. (3.4) with F and I representing the fast and intermediate energy ranges in G1, the SIS indirectly represent the spectral shift in the whole fast range [53]. It is the reason that the SIS is additionally used for PAs whose flux spectra are notably shifted by the radial reflector nodes filled with abundant of moderator.

$$L_2 + \Sigma_{r2} \phi_2 = \Sigma_{1 \rightarrow 2} \phi_1, \quad \Gamma = \frac{\phi_1}{\phi_2} = \frac{\Sigma_{r2} + (L_2/\phi_2)}{\Sigma_{1 \rightarrow 2}}, \quad (3.3)$$

$$\Sigma_{1 \rightarrow 2} = \frac{\Sigma_{I \rightarrow T} \phi_I}{\phi_F + \phi_I}, \quad (3.4)$$

Therefore, an assemblywise XS for g-th group is functionalized with the fast (l_1) and thermal (l_2) LTRRs and the SIS as:

$$\frac{\Sigma_g - \Sigma_g^{SA}}{\Sigma_g^{SA}} = \alpha_g l_1 + \beta_g l_2 + \gamma_g \Delta\Gamma, \quad (3.5)$$

$$\Sigma_g = \Sigma_g^{SA} \left(1 + \alpha_g l_1 + \beta_g l_2 + \gamma_g \Delta\Gamma \right), \quad (3.6)$$

where γ_g is nonzero only for PAs.

For the functionalization of MG PHXSs, on the other hand, the SIS is not used because it cannot yield an improvement of the solution agreements while deteriorates the stability of LFM scheme [54]. Only the use of LTRRs based on a previous study of Fujita [36] is determined. By utilizing the generalized perturbation theory based on the diffusion theory, Fujita derived the relationship between the variation of MG PHXSs due to the leakage and the leakage to flux ratio which is essentially similar with the LTRRs. However, while the spectral interference correction proposed by Fujita employs the groupwise leakage parameters for the functionalization of PHXSs, the pinwise LFM employs only the three LTRRs as:

$$\frac{\Sigma_g - \Sigma_g^{SA}}{\Sigma_g^{SA}} = \alpha_g (l_F - l_F^{SA}) + \beta_g (l_I - l_I^{SA}) + \gamma_g (l_T - l_T^{SA}) \quad (3.7)$$

$$= \alpha_g \Delta l_F + \beta_g \Delta l_I + \gamma_g \Delta l_T,$$

$$\Sigma_g = \Sigma_g^{SA} \left(1 + \alpha_g \Delta l_F + \beta_g \Delta l_I + \gamma_g \Delta l_T \right). \quad (3.8)$$

The subscripts F , I , and T indicate the fast, intermediate, and thermal energy ranges. These three energy groups (3G) are independent of the number of energy groups actually used for the core calculation. Not the LTRRs themselves but their deviations from the reference condition are used in that the pin-cells has a certain amount of the leakage over surfaces even if the assembly has all reflective BC.

3.1.1. Three group LTRRs as the fitting parameters

The use of the minimum number of leakage parameters is the fundamental strategy of the pinwise LFM. Increasing the number of the parameters corresponding to the actual number of energy groups is considered not desirable. Since refining the groups effectively reduces the group condensation error which takes the large portion of the total spectral error, the use of the groupwise parameters indicates spending more computing cost for correction of more accurate PHXSs.

In addition, the LFM coefficients for the functionalization are obtained by the fixed-point least square fitting on the data set obtained from various sample problems, so that more fitting samples are required for more fitting parameters. It renders a notable problem in application of the pinwise LFM for the practical core calculations. In case of the AP1000 PWR initial core, for example, 6 types of 2x2 checkerboards (CBs) per FA can be obtained from the 7 FA types. Thus, more samples, such as 3x3 mini core configurations, should be devised for the use of the 8G LTRRs.

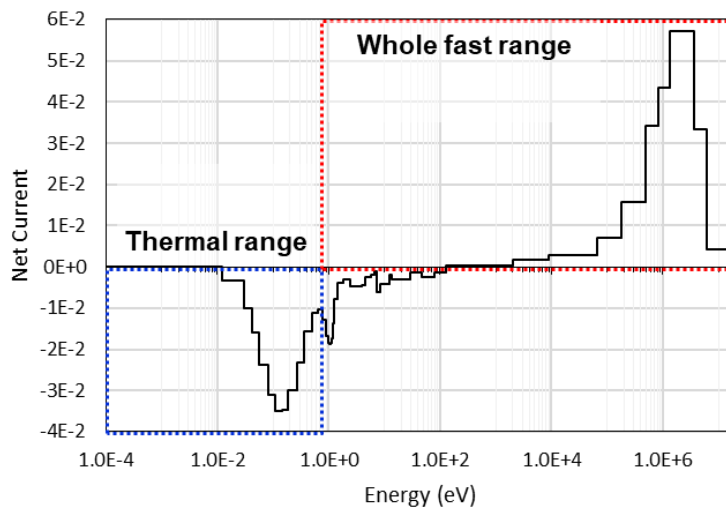


Figure 3.1. 47G current spectrum for a UO_2 fuel pin-cell

In order to use the smaller number of LTRRs, the 2G LTRRs were tested the first. As shown in **Figure 3.1**, the fast and thermal leakages are depending on the fission and thermal flux spectrum, respectively, so those are the most fundamental and independent to each other. Therefore, fitting of the groupwise LTRRs using the 2G LTRRs was tried. If a PHXS can be represented by the groupwise LTRRs as:

$$\frac{\Sigma_g - \Sigma_g^{SA}}{\Sigma_g^{SA}} = \sum_{g'} c_{g'} \Delta l_{g'}, \quad (3.9)$$

and each Δl_g can be represented by the LTRRs for the whole fast range (Δl_{wF}) and the thermal ranges (Δl_T) as:

$$\Delta l_g = d_{g,wF} \Delta l_{wF} + d_{g,T} \Delta l_T, \quad (3.10)$$

it is obvious that the target PHXS can be represented with only the 2G LTRRs as well. However, the 2G fitting results are not satisfactory in general.

Figure 3.2 presents the example. For a corner pin-cell of the APR1400 B2 FA, the groupwise LTRRs were obtained from the 4G nTRACER calculations using the SA and 2x2 CB configurations, and the least square fittings were performed with the 2G LTRRs. From the fitting results, it is clearly noted that the Δl_2 data points deviate from the fitting plane fixed at the origin. Resultantly, the fitting performance in terms of the goodness of fitting (GOF) defined as Eq. (3.11) is merely 0.457.

$$R^2 = 1 - \frac{\sum_i (z_i - f(x_i, y_i))^2}{\sum_i (z_i - \bar{z})^2} \quad (3.11)$$

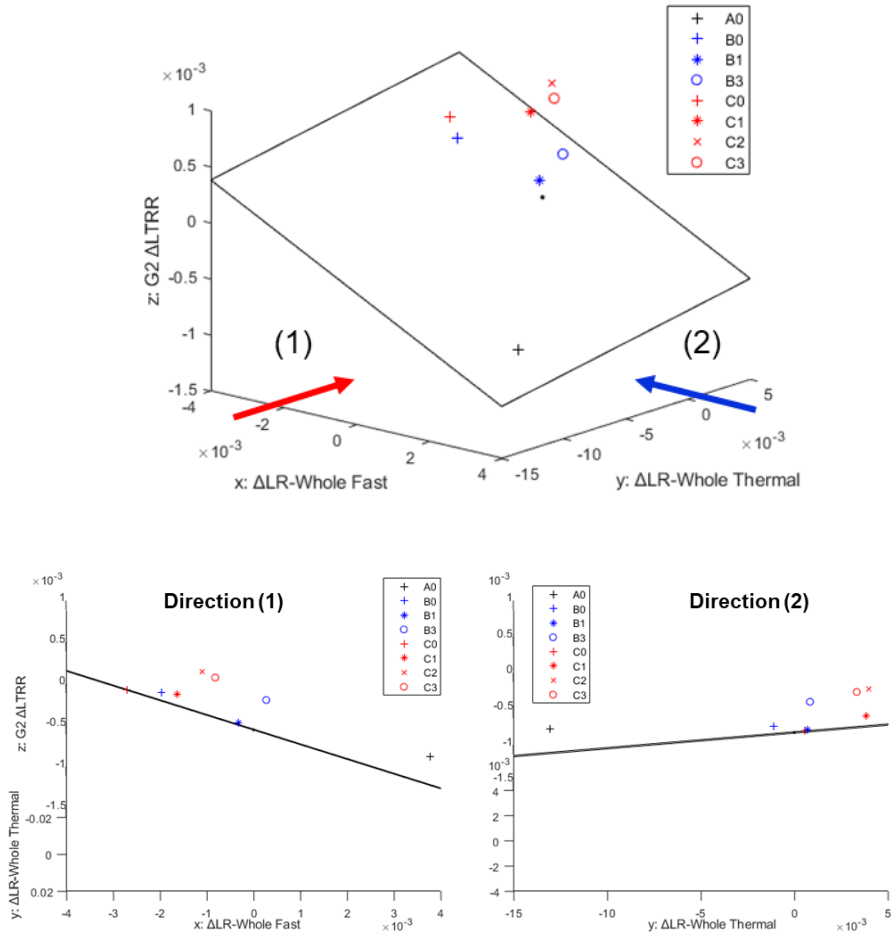


Figure 3.2. Fitting result for the G2 LTRRs of the 4G calculations obtained for a corner pin-cell of the APR1400 B2 FA with the 2G LTRRs

It is worthwhile to note that a similar error was observed from the assemblywise LFM [25]. The fitting planes based on PAs were notably shifted from the planes based on 2x2 CB representing the core internal FAs (IAs), and the shift rendered the need for employment of the SIS for PAT. Therefore, as the SIS indirectly represents the spectral shift in the whole fast range, the whole fast range is subdivided into the fast and intermediate ranges to consider the shift directly.

Figure 3.3 and **Table 3.1** present the fitting results for the out scattering XS with the 2G, 3G, and 4G LTRRs. For the fitting with the 3G LTRRs, G1, G2 – 3, and G4 of the 4G, and G1 – 3, G4 – 6, and G7 – 8 of the 8G are taken as the fast, intermediate,

and thermal energy ranges, respectively. For the fitting with the 4G LTRRs, on the other hand, the 4G correspond to G1 – 3, G4 – 5, G6, and G7 – 8 of the 8G. Note that the contribution of ΔI_I is removed from the relative difference of XS as:

$$\frac{\sum_g^{Core} - \sum_g^{SA}}{\sum_g^{SA}} - \beta_g \Delta I_I, \quad (3.12)$$

and the remaining are shown in the right of **Figure 3.3**, in order to set the data points on the fitting plane. In addition to the GOF, the RMS fitting error defined as Eq. (3.13) is also given in **Table 3.1**. Compared to the fitting results based on the 2G LTRRs, the results based on the 3G LTRRs show notable improvement. For G2 out scattering XS of the 4G, for example, the GOF is improved from 0.795 to 1.000 and the RMS fitting error is decreased from $130 \times 10^{-3}\%$ to $5 \times 10^{-3}\%$. It is also noted that the data points are closely distributed to the fitting plane, as shown in the right of **Figure 3.3**. However, the fitting results based on the 4G LTRRs are not notably different to the results based on the 3G LTRRs.

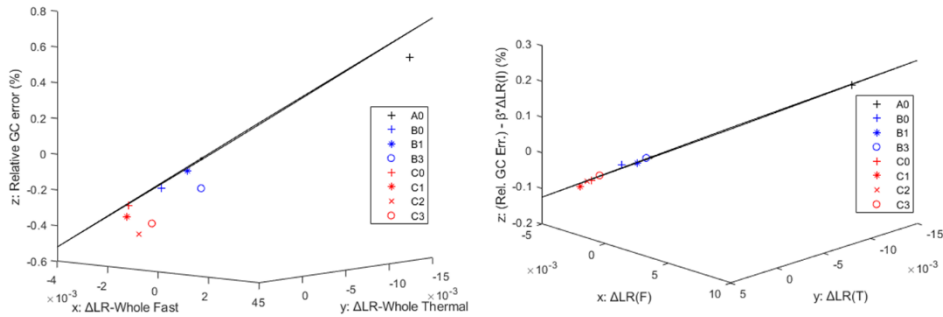


Figure 3.3. Fitting results for the G2 out scattering XS of the 4G obtained for a corner pin-cell of the APR1400 B2 FA with the 2G (left) and 3G (right) LTRRs

$$E_{LFM}^{RMS} = \sqrt{\frac{1}{N} \left(\frac{\Sigma_{CB} - \Sigma(\Delta l)}{\Sigma_{SA}} \right)^2} \quad (3.13)$$

Table 3.1. Improvement of the fitting performance for out scattering XS obtained from a corner pin-cell of the APR1400 B2 FA

		2G LTRR	3G LTRR	4G LTRR
$\Sigma_{out,2}$ (4G)	R^2 (GOF)	0.795	1.000	1.000
	E_{LFM}^{RMS} (10^{-3} %)	130.1	5.2	2.7
$\Sigma_{out,4}$ (8G)	R^2 (GOF)	0.042	0.999	1.000
	E_{LFM}^{RMS} (10^{-3} %)	29.1	0.9	0.6

3.1.2. Energy group definition for the intermediate range LTRR

The need for further investigation of the energy boundary to define the fast and intermediate energy ranges is rendered by the use of the 3G LTRRs. As previously noted, the fast leakage determined by the fission spectrum and the thermal leakage determined by the thermal flux spectrum are the most fundamental parameters, so that two options can be considered for the division of whole fast range. One is the simplest 3G taking G1 – 9, G10 – 35, and G36 – 47 of the nTRACER 47G as the fast, intermediate, and thermal ranges. Based on the observation that the fission spectrum is notable only in G1 – 9 and the fact that the upper energy boundary of G36 is the well-known thermal cut-off energy of 0.625 eV, all the groups between the two ranges are taken as the intermediate range. The other is a modified 3G separating certain energy range which cannot be represented well as the function of the fast and thermal LTRRs and taking it as the intermediate range.

In order to determine the intermediate energy range for the modified 3G, the 47G nTRACER calculations were performed for various CBs whose configurations are based on **Figure 3.4** with periodic boundary condition. By employing the nTIG

restart capability of nTRACER, the explicitly modeled 2x2 CB geometries were defined by GEO files and the material information for each flat-XS-region (FXR) was assigned by MAT files. The MAT files were obtained from the SA depletion calculations with nTRACER. For Sample 1 configuration, the material information for zero burnup was assigned for the neighboring FAs regardless of the burnup exposure of the target FA. For Sample 2 configuration, on the contrary, the assembly averaged burnup exposures are the same for the target and neighboring FAs. Note that Sample 1 is to mimic a reload core where the fresh and burned fuels are shuffled while Sample 2 is to simulate a part of the initial core which is being depleted.



Figure 3.4. 2x2 CB configurations used to obtain the LFM coefficients for a target FA with a certain burnup exposure

The 47G LTRRs were then obtained for each pin-cell and the least square fittings employing the fast and thermal range LTRRs corresponding to G1 – 9 and G36 – 47 were performed. **Figure 3.5** and **Figure 3.6** present the results obtained for a corner pin-cell of the AP1000 Region 4 FA with 5GWD/tHM of the assembly averaged burnup exposure. Region 4 FA loaded with 3.4%, 3.8%, and 4.2% enriched UO₂ fuels features the checkerboard of the higher/lower enriched fuel in the core, and it is equipped with a large number of the integral fuel burnable absorbers (IFBA) and the wet annular burnable absorbers (WABA). For the energy range higher than 0.1 eV, the GOF is given in **Figure 3.5** and the RMS fitting errors are in **Figure 3.6**. The dotted black lines are the energy group boundaries of the 8G structure.

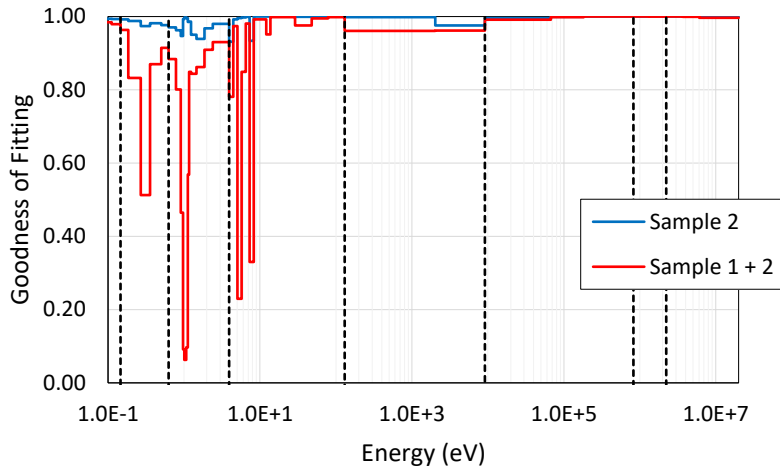


Figure 3.5. The GOF obtained by fitting the 47G delta LTRRs with the 2G LTRRs for a corner pin-cell of the AP1000 Region 4 FA with 5GWD/tHM burnup

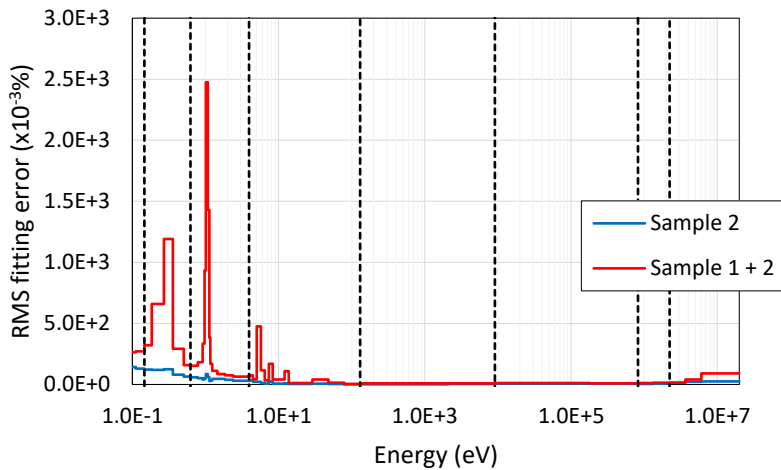


Figure 3.6. The RMS error obtained by fitting the 47G delta LTRRs with the 2G LTRRs for a corner pin-cell of the AP1000 Region 4FA with 5 GWD/tHM burnup

From the figures, it is noted first that the 47G delta LTRRs obtained only from the Sample 2 configuration are somewhat accurately represented by the fast and thermal LTRRs. The GOF and the RMS fitting error denoted by the blue lines are larger than 0.970 and less than $84.2 \times 10^{-3}\%$, respectively. However, in case that the 47G delta LTRRs obtained from the Sample 1 configuration are included, the fitting results are

severely deteriorated as denoted by the red lines. The GOF drops to nearly about 0.063 and the RMS fitting error increases to $2474.9 \times 10^{-3}\%$ and those are especially noted in the energy range corresponding to G6 of the 8G and G3 of the 4G.

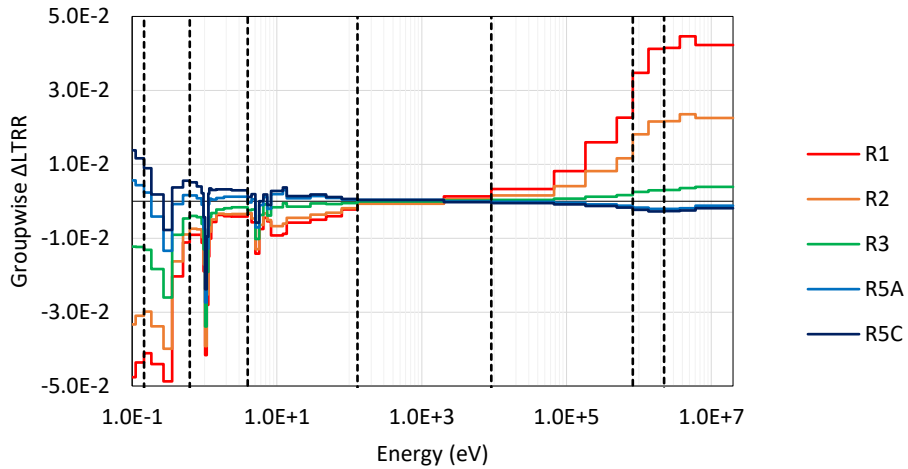


Figure 3.7. The 47G delta LTRRs obtained from the Sample 1 configurations for a corner pin-cell of the AP1000 Region 4 FA with 5 GWD/tHM burnup

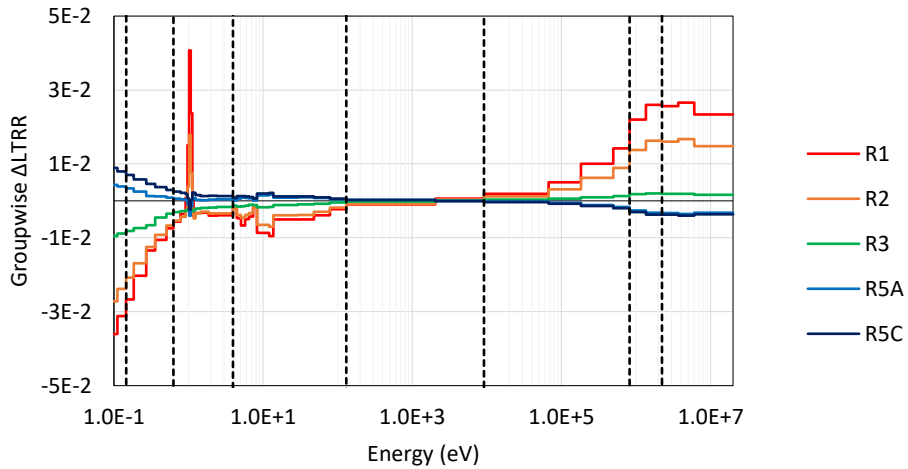


Figure 3.8. The 47G delta LTRRs obtained from the Sample 2 configurations for a corner pin-cell of the AP1000 Region FA with 5 GWD/tHM burnup

The deterioration originates from the difference of the 47G delta LTRRs presented in **Figure 3.7** and **Figure 3.8**. The figures correspond to the Sample 1 and 2 and the neighboring FA types are indicated. In the energy range corresponding to G1 – 4 of the 8G, the 47G delta LTRRs obtained from the two configurations show similar distribution shapes. In G5 of the 8G, the differences in the distributions are noted but those are not as significant as the differences in G6 of the 8G.

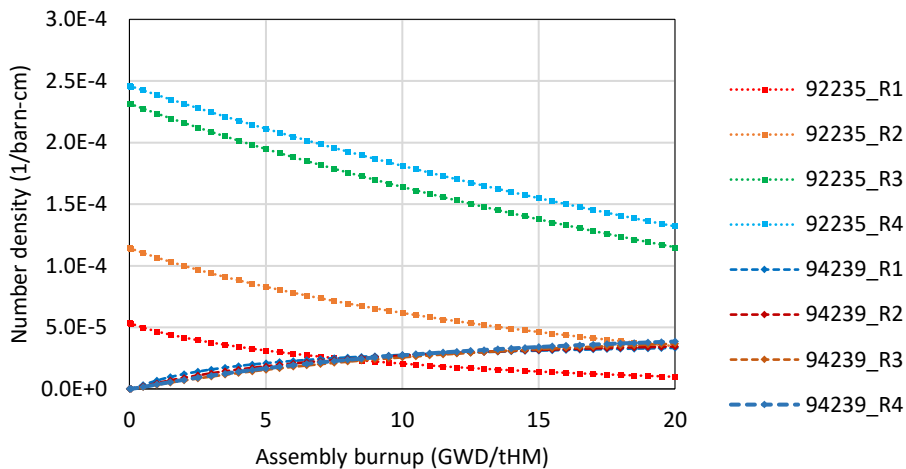


Figure 3.9. The U-235 and Pu-239 inventory changes for the corner pin-cells of the AP1000 PWR FAs during the depletion

The difference is related with the isotope inventory change due to the depletion. As shown in **Figure 3.9**, the Pu-239 inventory of corner pin-cells is gradually increased by the depletion. The ratio of Pu-239 to U-235 is the largest for Region 1 FA loaded with the natural U and it is followed by 1.58% enriched Region 2 FA. The Pu-239 number density reaches to nearly about 67%, 22%, and 8% of the U-235 for Region 1, 2 and 3 at the point that the assembly averaged burnup is 5 GWD/tHM, and the density fractions are proportional to the significance of the 47G delta LTRR deviations presented by **Figure 3.7** and **Figure 3.8**. It is because the XS difference between the two isotopes is notable at around the energy range corresponding to G6 of the 8G, as shown in **Figure 3.10**.

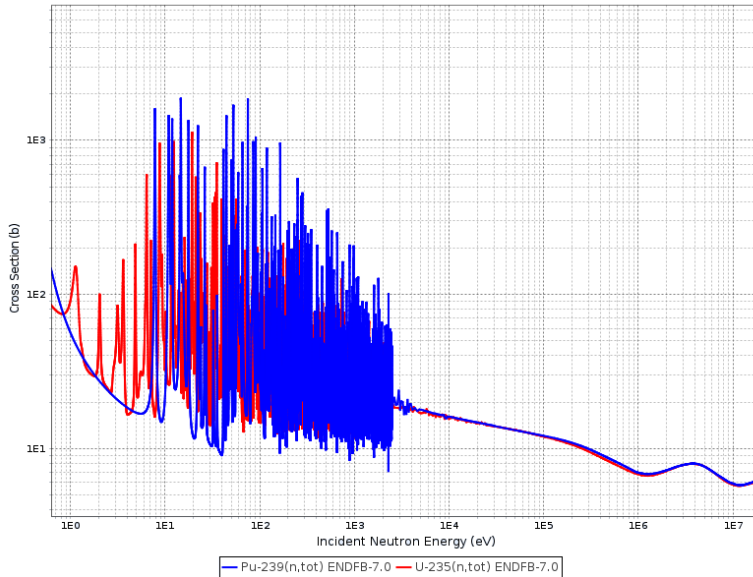


Figure 3.10. Microscopic total XS of U-235 (red) and Pu-239 (blue) in the whole fast energy range higher than 0.625 eV cut-off

Based on the results showing that G1 – 5 of the 8G can be represented well by the fast and thermal LTRRs, G4 – 5 in addition to the G1 – 3 are included the fast range and only G6 is selected as the intermediate. The determination for the modified 3G corresponds to G1 – 2 and G3 of the 4G.

The fitting results based on the simple and the modified 3G are essentially the same for the initial core. However, as the burnup increases, the fitting results based on the simple 3G are severely degenerated while the results based on the modified 3G are not. The examples are presented in **Figure 3.11** and **Figure 3.12**. The fitting targets are G3 nu-fission PHXSs of the 4G. The burnup exposures of the corner pin-cell are 4.5 and 16.6 GWD/tHM at the points the assembly burnups are 5.0 and 18.0 GWD/tHM. Note that not the relative difference of the PHXSs themselves but the data points processes as Eq. (3.12) are presented in the figures to show the distributions of the points on the fitting plane.

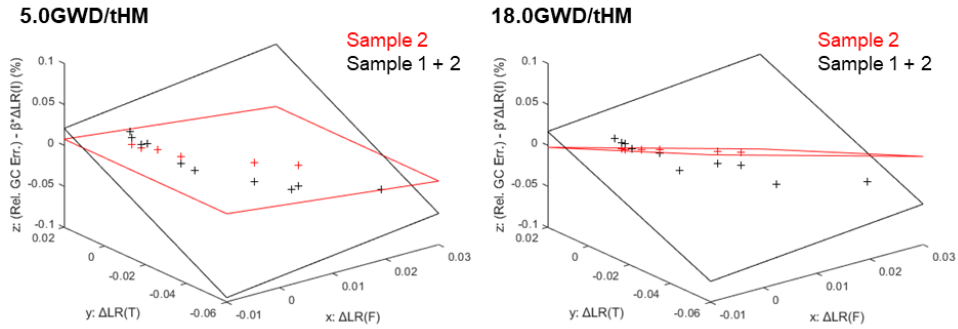


Figure 3.11. Fitting results based on the simple 3G for G3 nu-fission PHXS of the 4G obtained from a corner pin-cell of the AP1000 Region 4 FA

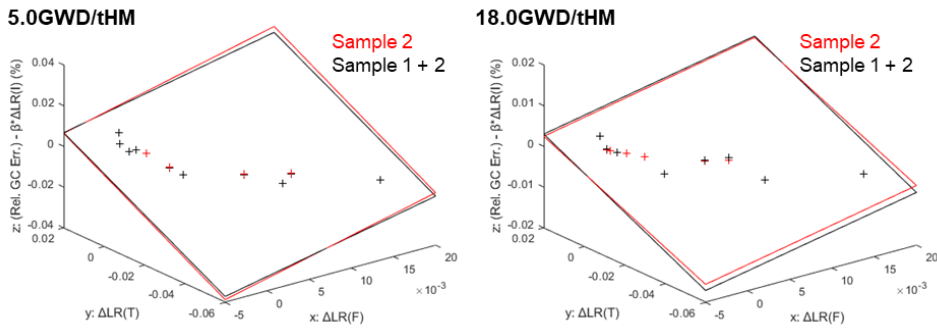


Figure 3.12. Fitting results based on the modified 3G for G3 nu-fission PHXS of the 4G obtained from a corner pin-cell of the AP1000 Region 4 FA

From **Figure 3.11**, it is clearly noted that the fitting plane based on the simple 3G is notably changed by the selection of fitting samples and the difference between the black and red planes depends on the increase of burnup. From **Figure 3.12**, on the contrary, the fitting plane based on the modified 3G is slightly changed by the sample and the difference between the planes does not increase by the burnup.

Resultantly, the fitting results based on the modified 3G are remarkably better than the simple 3G results and comparable to the 4G fitting results, as shown in **Table 3.2**. The fitting results for G3 out-scattering are also included for the comparison. In the case that the simple 3G is employed, the GOF for G3 nu-fission PHXS is 0.998 for the Sample 2 only so that the fitting results are seemingly good, but it drops to 0.667

for the Sample 1 only and to 0.398 for the Sample 1 + 2 in that the 3G LTRRs are inadequate to capture the deviations noted in **Figure 3.7** and **Figure 3.8**. In the case that the modified 3G is employed, in contrast, the GOF is 0.941 for the nu-fission and 0.987 for the out scattering, while the GOF based on the four groupwise LTRRs is 0.941 for the nu-fission and 0.988 for the out scattering. In addition, the difference of the RMS fitting errors obtained with the modified 3G and the 4G LTRRs is also small. It does not exceed $0.5 \times 10^{-3}\%$. Therefore, the modified 3G is determined as the default energy range setting for the pinwise LFM.

Table 3.2. Fitting results for G3 PHXSs of the 4G obtained from a corner pin-cell of the AP1000 Region 4 FA with 5 GWD/tHM burnup

Specifications	G3 nu-fission (4G)		G3 out scattering (4G)	
	GOF	RMS ($10^{-3}\%$)	GOF	RMS ($10^{-3}\%$)
Sample 1 (Simple 3G)	0.667	287.0	0.890	105.7
Sample 2 (Simple 3G)	0.998	8.6	0.995	6.1
Sample 1 + 2 (Simple 3G)	0.398	379.6	0.623	166.3
Sample 1 + 2 (Modified 3G)	0.941	92.7	0.987	25.3
Sample 1 + 2 (4G fitting)	0.941	92.5	0.988	24.8

3.1.3. Core calculation with the pinwise LFM

The LFM coefficient generations employing the MG PHXSs as the fitting data and the corresponding LTRRs as the fitting parameters is the first step in application of the pinwise LFM. The PHXSs and LTRRs should be generated by the transport calculations for a group of representative CB configurations. **Figure 3.13** shows the 2x2 CB configurations for a target FA with and without CR insertion. The periodic boundary conditions are employed for each CB.

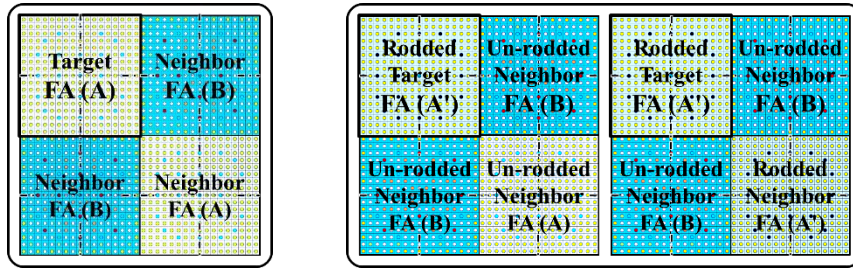


Figure 3.13. Sample CB configuration for a normal FA (left) and a rodded FA (right)

For a un-rodded FA, AB/BA patterned 2x2 CB which mimics the core interior region is used. The 2x2 CB consists of two types of FAs, therefore, a core loaded with N types of FAs provides $N(N+1)$ sample points per pin position per group. For a rodded FA, both A'B/BA and A'B/BA' patterned CBs are used to consider different rodded configurations. The A'B/BA patterned CB with 3 un-rodded FAs represents a single control rod bank insertion case while the A'B/BA' patterned CB with 1 rodded and 2 un-rodded FAs represents an all-rods-in (ARI) infinite core. The number of sample points is $2N(N-1)$ for the target core.

The coefficient set is obtained by the fixed point least-square fitting using the generated PHXSs and the LTRRs. It should be noted that the pinwise LFM does not require an additional treatment for PAs such as PAT [25]. Although a similar method can be employed for the pinwise LFM, its effect on the core calculation results is less than 1 pcm for the reactivity and 0.1% for the pin power.

In addition, a single set of radial reflector PHXSs obtained from the fuel-reflector local problem loaded with arbitrary FAs are employed for the core calculation and the leakage correction is not applied. The use of the single set is determined by test calculations outlined in **Figure 3.14**. The PA-reflector sets are denoted by the FA type and the shape of the local problem. For example, B-edge PA and reflector indicate that the PHXSs and the SPH factors of the PA and reflector are based on the edge shaped local problem with B type FA. For the presented case, the PHXSs and the SPH factors for the PAs and the reflectors were obtained with A and B type FAs. Then the inconsistency was introduced, e.g. put A-edge reflector next to B-edge PA,

and the PHMGCs were performed. The results are compared with the nTRACER reference. Even with the 2-GCs, the difference due to the inconsistent reflector is less than 10 pcm for the reactivity and 0.5 % for the pin power error.

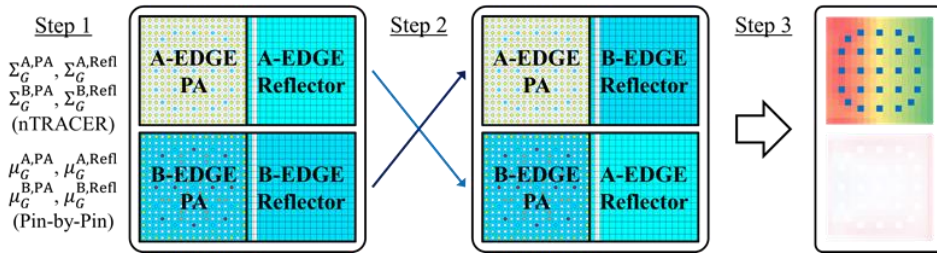


Figure 3.14. Switching reflectors to assess the error of using a single reflector XS set

The core scale test was also performed. The APR1400 PWR 2D initial core was employed due to the large radial leakage yielded by high-enriched PAs. The reflector PHXSs obtained by the nTRACER calculations for the fuel-reflector problems and the whole core are utilized for the test. The core calculations were carried out by SPHINCS. The comparison between the two cases based on the different reflector PHXSs reveals only a marginal difference, 2 pcm for the $\Delta\rho$ and 0.1 % for the RMS pin ΔP , even though the 2G was used to increase the spectral error.

The calculation scheme of the pinwise LFM involves iteration shown in **Figure 3.15**. The 3G LTRRs are determined at each step using the MG core calculation result and are fed back to update the functionalized MG PHXSs. The updated PHXSs are then used for the core calculation. The iteration continues until the convergence criteria are satisfied. The differences in reactivity or the fission source distribution between the two successive steps are used to check solution convergence.

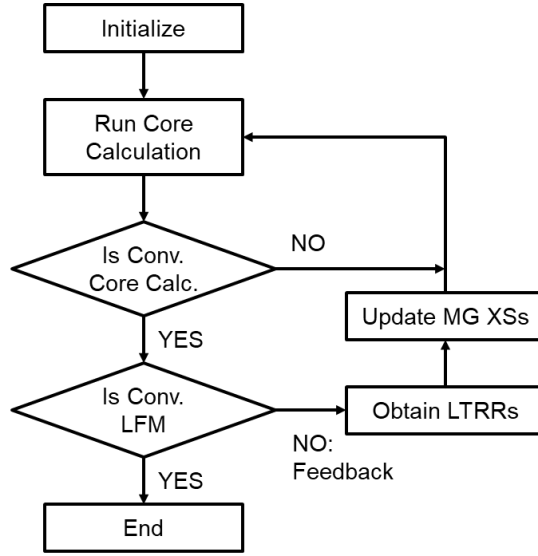


Figure 3.15. Iterative calculation scheme of the pinwise LFM

3.2. Considerations for the SPH Factors

The use of the SPH factors in the core calculation rendered two related issues. The inconsistency of the SPH factors in definition of the LTRR is the first. The PHXSs and the 3G LTRRs used for the generation of the LFM coefficients are obtained by the transport calculations for a target SA and sample CB problems. By introducing the SPH factors (μ_G) that forces the equivalence between the heterogeneous and the homogenized systems, Eq. (3.1) can be rewritten for a LTRR (l_G^{CB}) determined by the transport calculation for a CB as:

$$l_G^{CB} = \frac{1}{\mu_G^{CB} \sum_{r,G} \phi_G^{Hom}} \left(\frac{\chi_G}{k_{eff}} \sum_{G'} \mu_{G'}^{CB} \nu \Sigma_{f,G'}^{CB} \phi_{G'}^{Hom} + \sum_{G' \neq G} \mu_{G'}^{CB} \Sigma_{G' \rightarrow G}^{CB} \phi_{G'}^{Hom} - \mu_G^{CB} \Sigma_{r,G}^{CB} \phi_G^{Hom} \right), \quad (3.14)$$

where ϕ_G^{Het} and ϕ_G^{Hom} are the heterogeneous reference flux and the homogeneous

flux, and Σ_G^{CB} is the G-th group PHXS generated by the transport calculation for the CB. The SPH factor (μ_G^{CB}) can be obtained by the lower order MG calculation with Σ_G^{CB} and it guarantees equivalence between the heterogeneous flux and the SPH corrected homogenized flux ($\mu_G^{CB} \phi_G^{Hom}$). The LTRRs obtained by Eq. (3.14) are independent of the lower order calculation options including the order of transport approximation and the degree of spatial discretization method, since the PHXSs and the SPH corrected fluxes originate from the transport reference.

In the core calculation, however, not μ_G^{CB} but the SA based SPH factors (μ_G^{SA}) are used. Since the neighbor effect perturbs both the PHXSs and the SPH factors, the LTRRs actually determined by the PHMGC would be different to the ones employed for the LFM coefficient generations. Fujita [55] suggested an alternative procedure which allows to avoid the inconsistency. The alternative procedure determines the LTRRs by the PHMGC employing Σ_G^{CB} and μ_G^{SA} as:

$$l_G^{CB} = \frac{1}{\mu_G^{SA} \Sigma_{r,G}^{CB} \phi_G^{Hom}} \left(\frac{\chi_G}{k_{eff}} \sum_{G'} \mu_{G'}^{SA} \nu \Sigma_{f,G'}^{CB} \phi_{G'}^{Hom} + \sum_{G' \neq G} \mu_{G'}^{SA} \Sigma_{G' \rightarrow G}^{CB} \phi_{G'}^{Hom} - \mu_G^{SA} \Sigma_{r,G}^{CB} \phi_G^{Hom} \right). \quad (3.15)$$

In order to assess the effectiveness of the new LTRRs, the LTRRs based on Eq. (3.14) and (3.15) were employed for the 4G SP₃ calculations with SPHINCS. The target problems are the heavily rodged AP1000 2D cores which feature the highly heterogeneous commercial core design. The results reveal that the effect of the different LTRRs is less than 7 pcm for the reactivity and within 0.4 % for the pin power. Despite the additional burden for the PHMGCs and the notable difference of the SPH factors due to the use of coarse mesh FDM, the improvement is marginal. Therefore, it is determined to keep using the LTRRs based on Eq. (3.14).

Perturbation of the SPH factors is another issue. Thus the change of the assembly BC introduced by the neighboring nodes not only results in the spectral error but also

affects the SPH factors, the SPH factors as well as the PHXSs should be corrected in principle in order to exactly reproduce the heterogeneous reference. The need for the accurate SPH factor can be clearly noted by test calculations for a simple CB, such as one presented in **Figure 3.16**. The target R2/R4 CB consists of the AP1000 Region 2 FA loaded with 1.58% UO₂ fuel and no BA and Region 4 FA loaded with 3.4%, 3.8%, and 4.2% UO₂ fuels and involving 68 IFBA and 12 WABA, and it represents the loading pattern of the core interior region.

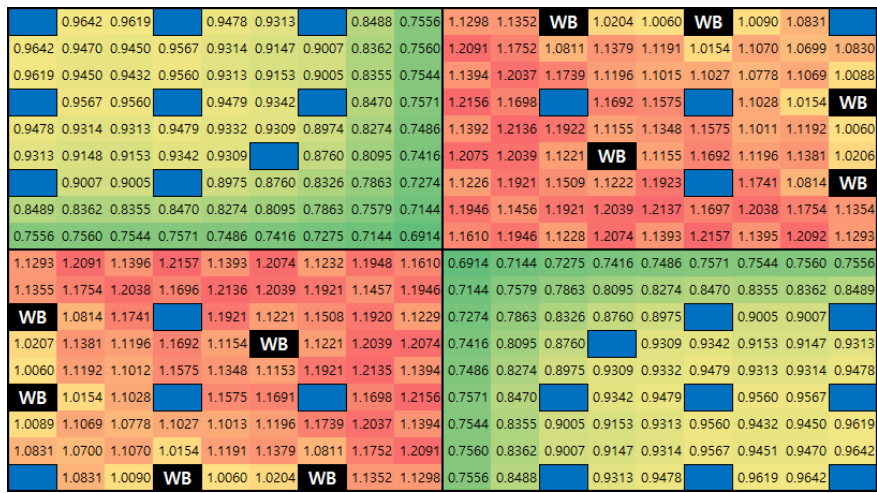


Figure 3.16. Radial pin power distribution of the 2x2 CB loaded with the AP1000 Region 2 and 4 FAs (Ref. k-eff: 1.01355)

Table 3.3 and **Figure 3.17** present the results of the 4G SP₃ FDM calculations for the R2/R4 CB taking each pin-cell as a mesh. Because of the spectral error which is especially severe at the boundaries, the RMS/MAX pin ΔP errors are 1.1%/3.2% for the no LFM case, but the errors decrease to 0.3%/0.7% by the correction. In that the remaining errors originate from the inconsistency of the SA SPH factors, the errors are decreased again by employing the CB SPH factors which are based on the CB. The MAX pin ΔP is only about 0.1% with the CB SPH factors and the pinwise LFM. Note that consistent results were obtained from different CB problems with various lower order solution methods.

Table 3.3. Results of the 4G SP₃ FDM calculations for the R2/R4 CB

SPH	LFM	$\Delta\rho$ (pcm)	Pin ΔP (%)	
			RMS	MAX
SA		4.1	1.13	3.15
SA	Applied	4.4	0.31	0.68
CB	Applied	0.1	0.03	0.14

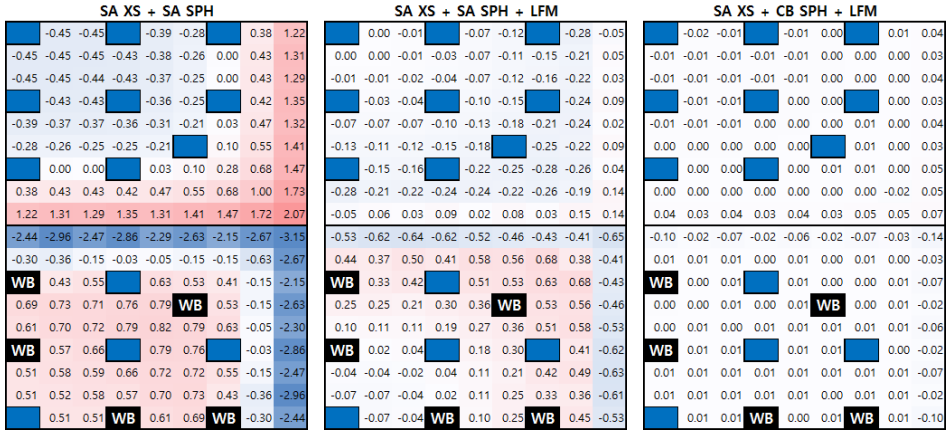


Figure 3.17. Radial pin power error (%) distributions for the R2/R4 CB obtained from the 4G SP₃ FDM calculations with different options

Motivated by the results, leakage correction of the SPH factors was examined. Noting that the fitting results for the SPH factors themselves were not satisfactory in that the GOF was nearly zero for certain pin-cells and energy groups, it was tried to functionalize the SPH corrected PHXSs as:

$$\frac{\mu_g^{CB} \Sigma_g^{CB} - \mu_g^{SA} \Sigma_g^{SA}}{\mu_g^{SA} \Sigma_g^{SA}} = \alpha_g \Delta I_F + \beta_g \Delta I_I + \gamma_g \Delta I_T. \quad (3.16)$$

However, this approach yielded severe deterioration of the fitting results. It would be worthwhile to see **Figure 3.18** which presents the GOF distributions for the SPH corrected G3 removal and nu-fission PHXSs of the 4G obtained from the AP1000 Region 4 FA. Note that the SPH factors are for the diffusion 1x1 FDM. The poor

the SP3 1x1 FDM, for example, the relative difference between the CB and SA SPH factors is decreased by normalizing the CB SPH factors using the AA-SPH, as shown in **Figure 3.19**. The relative difference ranging from -1.1% to 2.0% is, however, still significant. Resultantly, the RMS/MAX pin ΔP obtained from the R2/R4 CB by the 4G SP₃ FDM calculation is 0.3%/0.7% with the correction for the PHXSs only, as noted in **Table 3.3**, and it is rather increased to 0.9%/1.7% by applying the additional correction to the AA-SPH and the pin ΔP are remarkable for the assembly internal pin-cells. Based on the results, it is determined not to apply a leakage correction for the SPH factors in this work. Correction strategies

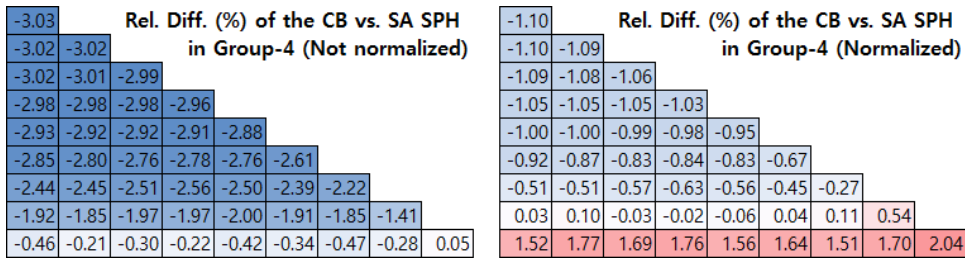


Figure 3.19. Relative difference (%) between the CB and SA SPH factors obtained from the AP1000 Region 4 FA with the SP₃ FDM solver

Instead, the use of assembly DF (ADF) is determined. Since the SA-AA-SPH for each group is set to unity during the SPH iterations, the deviation of AA-SPHs in the core cannot be considered by the conventional SPH factors based on SA configurations. This inherent limit of the SPH method can be effectively reduced by employing the ADF in addition to the pinwise SPH factors. The concept of using the pinwise SPH factors with the ADF is essentially the same with the improved SPH method [16], however, not the flux based ADF but the current based ADF [56] is used for the SP₃ to avoid difficulties in the higher angular moment calculations with the MOC. Note that the improved SPH method is used for the diffusion. The current based DF for the SP₃ is obtained as:

$$f^{\pm} = \frac{J^{\pm}}{J_1^{\pm}} = \frac{J^{\pm}}{\frac{1}{4}\hat{\phi}_0 \pm \frac{1}{2}J_1 - \frac{3}{16}\phi_2}, \quad (3.18)$$

where J^{\pm} and J_1^{\pm} are the partial current of the reference and the SP₃, and $\hat{\phi}_0$ is the summed flux and ϕ_2 is the 2nd angular moment. The ADF is obtained after the SPH iteration is converged and used to divide the pinwise SPH factors.

Table 3.4. Comparison of the 4G AA-SPHs obtained with the SP₃ SENM solver for the AP1000 R2/R4 CB

		G1	G2	G3	G4
CB SPH	Region 2	0.9934	1.0004	1.0021	1.0214
	Region 4	1.0061	0.9996	0.9978	0.9656
	Ratio (2 vs. 4)	0.9874	1.0007	1.0044	1.0579
SA SPH	Rel. Error (%)	1.28	-0.07	-0.44	-5.47
SA SPH + ADF	Region 2	1.0019	0.9924	0.9977	0.9785
	Region 4	1.0026	0.9914	0.9947	0.9528
	Ratio (2 vs. 4)	0.9993	1.0010	1.0031	1.0268
	Rel. Error (%)	1.20	0.03	-0.13	-2.92

The effectiveness of the ADF can be noted by comparing the AA-SPHs. For the example, **Table 3.4** shows the 4G AA-SPHs obtained with the SP₃ SENM solver for the R2/R4 CB. *CB SPH*, *SA SPH*, and *SA SPH + ADF* indicate that the AA-SPHs were obtained by the CB calculations with the CB PHXSs and the CB SPH factors, SA SPH factors, and SA SPH factors normalized with the ADF, respectively. *Ratio* is determined by dividing the Region 2 AA-SPH with the Region 4 AA-SPH for each group, and *Rel. Error* is the relative error of the ratio to the CB SPH case.

From the table, it is clearly noted that the error reduction is the most significant in G4 where the local heterogeneity and the resulting flux gradient are severe. The CB calculation results presented in **Table 3.5** and **Figure 3.20** reveal that the error reduction due to the ADF notably improves the accuracy in that the RMS/MAX pin

ΔP errors are decreased from 0.7%/1.3% to 0.2%/0.4%.

Table 3.5. Results of the 4G SP₃ SENM calculations for the R2/R4 CB

SPH	LFM	$\Delta\rho$ (pcm)	Pin ΔP (%)	
			RMS	MAX
SA Only		10.6	0.66	1.96
SA Only	Applied	1.4	0.70	1.27
SA + ADF	Applied	-1.3	0.24	0.43

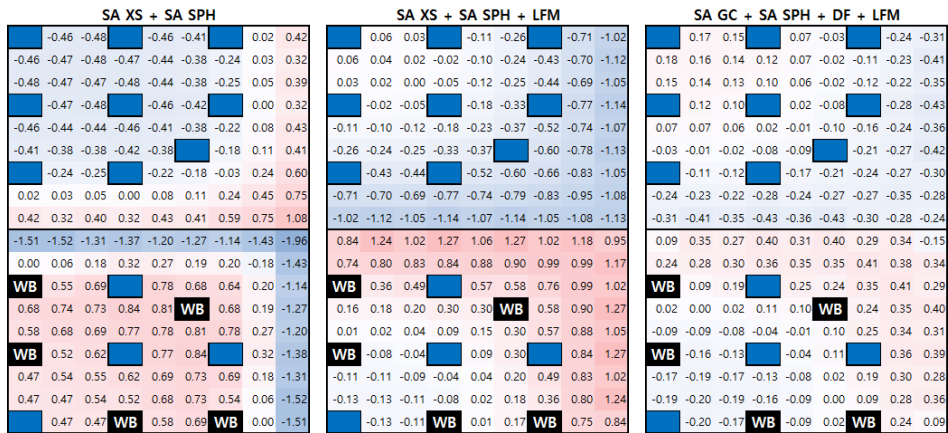


Figure 3.20. Radial pin power error (%) distributions for the R2/R4 CB obtained from the 4G SP₃ SENM calculations with different options

3.3. Coefficient Generations for Branch Calculations

Functionalization of the PHXSs to the thermal hydraulic (T/H) effect is normally performed by combining the partial derivative terms corresponding to each branch condition as follow [18]. It is based on the assumption that the cross effect of the branch conditions is small to neglect.

$$\begin{aligned} \sigma(T_m, T_f, ppm, \rho) &= \sigma(T_{m,0}, T_{f,0}, ppm_0, \rho_0) \\ &+ \left. \frac{d\sigma}{dT_m} \right|_{P=P_0} (T_m - T_{m,0}) + \frac{\partial \sigma}{\partial \sqrt{T_f}} (\sqrt{T_f} - \sqrt{T_{f,0}}) \quad (3.19) \\ &+ \frac{\partial \sigma}{\partial ppm} (ppm - ppm_0) + \frac{\partial \sigma}{\partial \rho} (\rho - \rho_0). \end{aligned}$$

If the cross effect between the T/H and leakage is negligible, the LFM coefficient set obtained from the base condition can be employed even if the core condition is perturbed by the T/H effect. In other words, based on **Figure 3.21** including the SA PHXSs at the base ($\bar{\Sigma}_g^{SA}$) and branch ($\bar{\Sigma}_g^{SA,TH}$) conditions and the CB PHXS at the base ($\bar{\Sigma}_g^L$) and branch ($\bar{\Sigma}_g^{L,TH}$), (5) can be approximated by a linear combination of (1) representing the leakage effect and (2) representing the T/H effect.

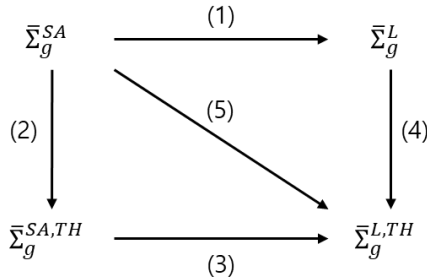


Figure 3.21. Functionalization of the PHXS to the T/H and leakage effects

In order to employ the functionalization scheme, significance of the cross effect should be systematically analyzed. As detailed in Ref. [25], the leakage and T/H

effects on the PHXS and the normalized flux can be determined as follow.

$$\begin{aligned}\Delta\bar{\Sigma}_g^{TH} &= \bar{\Sigma}_g^{SA,TH} - \bar{\Sigma}_g^{SA}, & \Delta\tilde{\phi}_g^{TH} &= \tilde{\phi}_g^{SA,TH} - \tilde{\phi}_g^{SA} & (\text{T/H effect}), \\ \Delta\bar{\Sigma}_g^L &= \bar{\Sigma}_g^L - \bar{\Sigma}_g^{SA}, & \Delta\tilde{\phi}_g^L &= \tilde{\phi}_g^L - \tilde{\phi}_g^{SA} & (\text{Leakage effect}).\end{aligned}\quad (3.20)$$

The tilde sign indicates that the sum of fine g group fluxes is 1 for the corresponding condensed G group. Then the cross effect can be determined by subtracting the leakage and T/H terms from the target PHXS and the normalized flux as:

$$\begin{aligned}\Delta\bar{\Sigma}_g^X &= \bar{\Sigma}_g^{L,TH} - (\bar{\Sigma}_g^{SA} + \Delta\bar{\Sigma}_g^{TH} + \Delta\bar{\Sigma}_g^L), \\ \Delta\tilde{\phi}_g^X &= \tilde{\phi}_g^{L,TH} - (\tilde{\phi}_g^{SA} + \Delta\tilde{\phi}_g^{TH} + \Delta\tilde{\phi}_g^L).\end{aligned}\quad (3.21)$$

By employing Eq. (3.20) and (3.21), the target PHXS involving the two effects can be decomposed as follow. The terms corresponding to the leakage, T/H, and cross effects are colored in blue, red, and green for the identification.

$$\begin{aligned}\bar{\Sigma}_G^{L,TH} &= \sum_{g \in G} (\bar{\Sigma}_g^{SA} + \Delta\bar{\Sigma}_g^L + \Delta\bar{\Sigma}_g^{TH} + \Delta\bar{\Sigma}_g^X) (\tilde{\phi}_g^{SA} + \Delta\tilde{\phi}_g^L + \Delta\tilde{\phi}_g^{TH} + \Delta\tilde{\phi}_g^X) \\ &= \sum_{g \in G} \left(\begin{aligned} &\bar{\Sigma}_g^{SA} \tilde{\phi}_g^{SA} + \bar{\Sigma}_g^{SA} \Delta\tilde{\phi}_g^L + \Delta\bar{\Sigma}_g^L \tilde{\phi}_g^{SA} + \Delta\bar{\Sigma}_g^L \Delta\tilde{\phi}_g^L \\ &+ \bar{\Sigma}_g^{SA} \Delta\tilde{\phi}_g^{TH} + \Delta\bar{\Sigma}_g^{TH} \tilde{\phi}_g^{SA} + \Delta\bar{\Sigma}_g^{TH} \Delta\tilde{\phi}_g^{TH} \\ &+ \bar{\Sigma}_g^{SA} \Delta\tilde{\phi}_g^X + \Delta\bar{\Sigma}_g^X \tilde{\phi}_g^{SA} + \Delta\bar{\Sigma}_g^X \Delta\tilde{\phi}_g^X \\ &+ \Delta\bar{\Sigma}_g^L (\Delta\tilde{\phi}_g^{TH} + \Delta\tilde{\phi}_g^X) \\ &+ \Delta\bar{\Sigma}_g^{TH} (\Delta\tilde{\phi}_g^L + \Delta\tilde{\phi}_g^X) \\ &+ \Delta\bar{\Sigma}_g^X (\Delta\tilde{\phi}_g^L + \Delta\tilde{\phi}_g^{TH}) \end{aligned} \right) \end{aligned}\quad (3.22)$$

The analysis aims to confirm that the contribution of the green colored terms are sufficiently smaller than the other, and the results are satisfactory. For a corner pin-cell of the APR1400 B2 FA, for example, the contributions are summarized in **Table 3.7** for the diffusion coefficient and the absorption, nu-fission, and out scattering PHXSs. As shown in **Table 3.6**, the moderator temperature and density is increased from 290.6°C and 0.7465g/cc to 330.6°C and 0.6493g/cc, considering the core inlet

condition and the upper limit of the T/H branch condition, and the leakage effect is introduced by composing a 2x2 CB with the A0 FA. Note that the A0 FA loaded with 1.72% UO₂ fuel has the lowest enrichment in the APR1400 initial core so that the leakage effect is the most significant.

Table 3.6. The leakage and T/H condition applied to the target pin-cell

	$\bar{\Sigma}^{SA}$	$\bar{\Sigma}^L$	$\bar{\Sigma}^{SA,TH}$	$\bar{\Sigma}^{L,TH}$
Leakage	SA	B2/A0	SA	B2/A0
T/H	290.6°C, 0.7465g/cc		330.6°C, 0.6493g/cc	

Table 3.7. Deviations of the 4G PHXSs due to the leakage, T/H, and cross effect obtained from a corner pin-cell of the APR1400 B2 FA

XS	Group	$\bar{\Sigma}^{SA}$	$\bar{\Sigma}^{L,TH}$	Total, %	Lkg, %	T/H, %	Other, %
D_G	1	1.764E+00	1.887E+00	6.97	0.07	6.91	-0.01
	2	7.450E-01	8.127E-01	9.08	0.00	9.08	0.00
	3	7.718E-01	8.491E-01	10.02	-0.01	10.03	0.00
	4	3.579E-01	4.045E-01	13.00	-1.41	14.75	-0.33
$\Sigma_{a,G}$	1	2.323E-03	2.300E-03	-0.99	0.64	-1.59	-0.05
	2	2.052E-02	2.008E-02	-2.16	0.20	-2.41	0.05
	3	1.631E-02	1.577E-02	-3.33	0.08	-3.43	0.02
	4	7.256E-02	6.919E-02	-4.65	1.44	-6.17	0.08
$\nu\bar{\Sigma}_{f,G}$	1	3.529E-03	3.470E-03	-1.67	1.24	-2.85	-0.06
	2	7.853E-03	7.815E-03	-0.49	0.26	-0.81	0.06
	3	1.850E-02	1.852E-02	0.10	0.12	-0.05	0.03
	4	1.014E-01	9.944E-02	-1.93	1.45	-3.52	0.14
$\Sigma_{out,G}$	1	1.628E-01	1.445E-01	-11.26	-0.28	-11.04	0.05
	2	4.096E-01	3.552E-01	-13.27	0.13	-13.41	0.01
	3	6.869E-01	6.040E-01	-12.06	-0.01	-12.06	0.00
	4	8.889E-01	7.852E-01	-11.67	0.84	-12.48	-0.03

The results show that the deviations are mainly due to the T/H effect and those are augmented by the leakage effect. The cross effect has the negligibly small portion.

Consequently, it is determined to apply the LFM coefficients obtained from the base condition for a range of the core operating condition.

In addition to the T/H effect, variations of the LFM coefficients by the depletion were observed. **Figure 3.22** and **Figure 3.23** show the results obtained from a corner pin-cell of the AP1000 Region 4 FA. Note that the 2x2 CB configurations given in **Figure 3.4** were employed for the coefficient generations. Although the coefficients are drastically changed near the BOC, the variations become smooth right after several burnup steps, so that the LFM coefficients can be interpolated to the burnup.

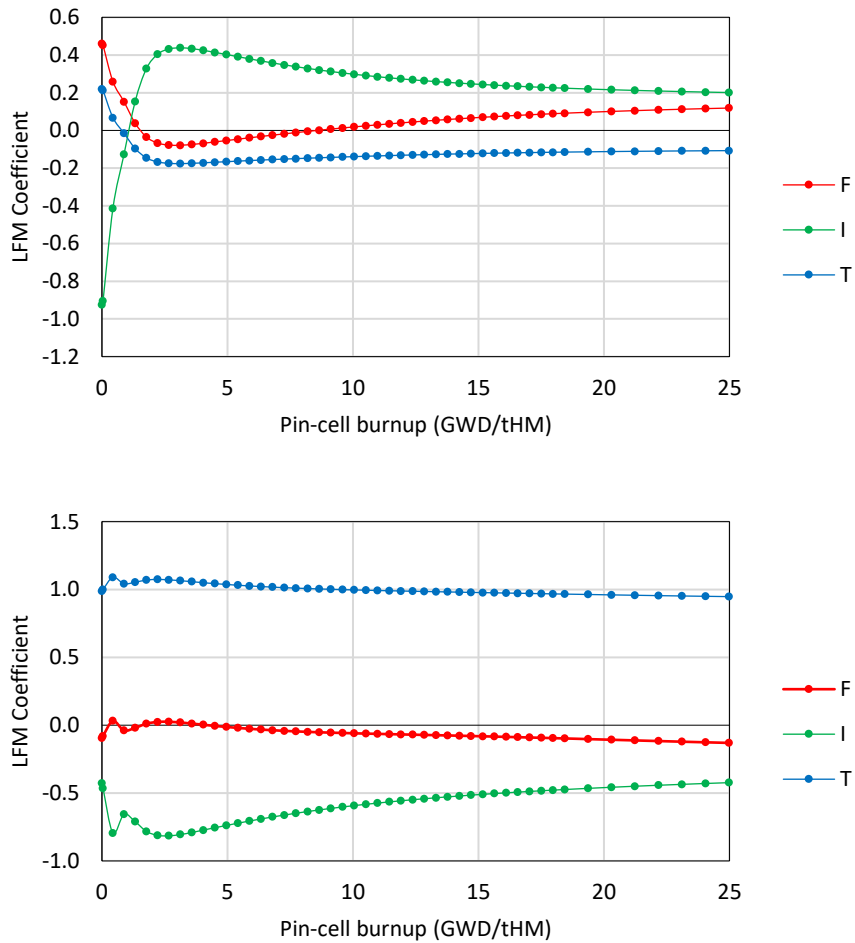


Figure 3.22. LFM coefficients of G1 (top) and G4 (bottom) diffusion coefficients

for the 4G obtained from a corner pin-cell of the AP1000 Region 4 FA

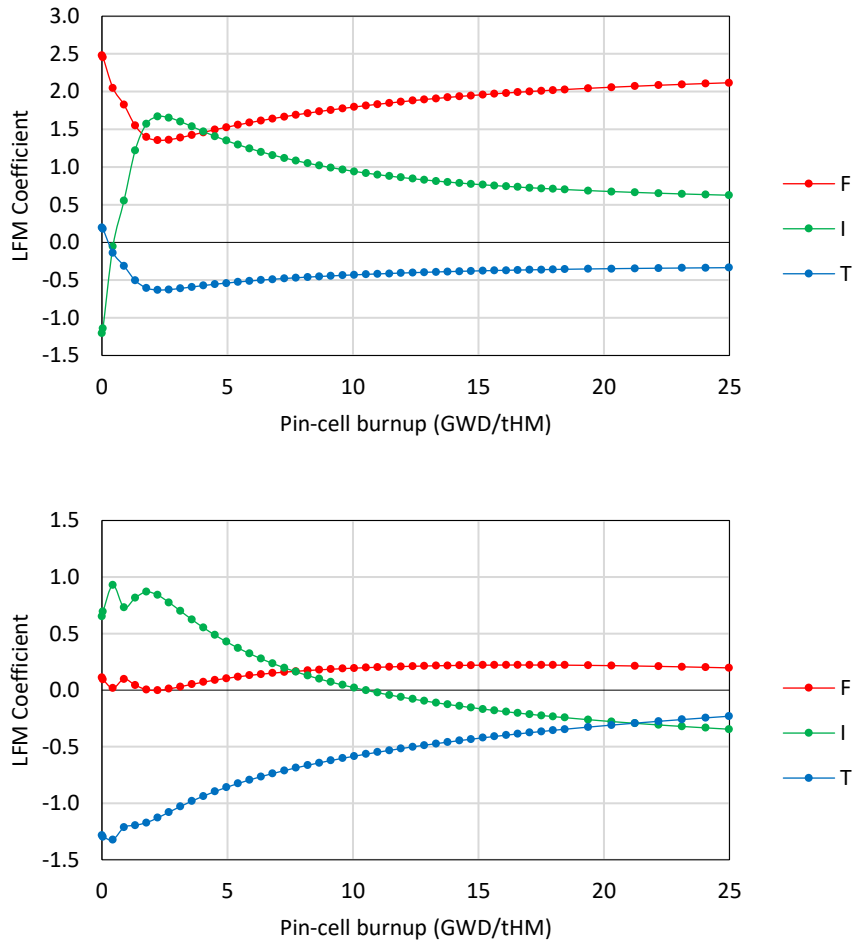


Figure 3.23. LFM coefficients of G1 (top) and G4 (bottom) nu-fission PHXSs for the 4G obtained from a corner pin-cell of the AP1000 Region 4 FA

Chapter 4. Validation of the Solution Methods

Test calculations based on the general TSCC procedure are performed to examine the accuracy of the solution methods and to observe the solution improvement by the pinwise LFM correction in the practical PHMGCs. The target cores are the KAIST 1A benchmark and the AP1000 and APR1400 PWR initial cores. The nTRACER flat source MOC calculations are performed for the targets with the 47G TCP₀ XS library for generation of the reference solution as well as the PHXSs. The ray parameters are characterized by 0.04cm ray spacing and 16 azimuthal and 4 polar angles per octant sphere. Note that the ray spacing and the number of azimuthal angles for the KAIST 1A problems are 0.01cm and 32 to keep the consistency with the results presented in **Chapter 2**. The reference solutions are obtained by the DWCCs while the SA configurations for FAs and the fuel-reflector problems for the radial reflectors are employed to obtain the PHXSs. The 4, 8, and 16G condensations are based on the energy group structures given in **Table 2.3**.

The SPH factor generations and the lower order core calculations are carried out by the FDM and SENM solvers of the diffusion and SP₃ equations. The SPHINCS and VANGARD codes are employed for the FDM and SENM calculations, and each pin-cell is taken as a mesh. The axial FDM mesh size for SPHINCS is 1.0 cm. The SPH factors for each solver are obtained from the PHXSs and the associated fluxes by following the standard procedure. Unless otherwise noted, the SPH factors are normalized with the proper ADF as detailed in the previous chapter. The S_N solvers are not used for the core calculations due to the inconsistency of the SA based SPH factors in the core. The SP₅ SENM solver, on the other hand, is employed for the KAIST 1A core and the AP1000 3D SA calculations to confirm that the SP₅ is not any better than the SP₃ in the PHMGC.

The outline of this chapter is as follows. **Chapter 4.1** is to present the preliminary test calculation results for the KAIST 1A benchmark problem. The core involves severe heterogeneity which originates from the small core size and the CB assembly loading pattern composed of the UO₂ and MOX FAs while the T/H conditions are

fixed. In this regard, KAIST 1A is highly adequate for examination of the solution methods and the pinwise LFM. In that the accuracy of the solver are estimated and the effectiveness of the pinwise LFM is revealed for this difficult problem, the range of test calculations is extended to the commercial reactor cores.

Chapter 4.2 presents the results obtained from the AP1000 PWR initial core. The target problems are the 2D initial HZP core and its depletion up to 20 GWD/tHM, the 3D SA and 3x3 mini-cores without and with the T/H effect, and the 3D cores at the HZP and HFP states and the Cycle 1 depletion. The 2D initial HZP core calculations are to show that the results for the large core are consistent with the KAIST 1A results, and the 2D HZP ARO core depletion is to estimate the solution agreements versus the core burnup and to validate the LFM coefficients tabulated to the pinwise burnup exposure. The 3D SA and 3x3 mini-core calculations are to reveal the need for a sufficiently high order axial solver, to select the formula to determine the effective fuel temperature in the T/H calculation, and to assess applicability of the LFM coefficients based on 2D for the 3D problems. The 3D core calculations are to demonstrate the accuracy of the SP₃ SENM solver and the performance of the pinwise LFM for the practical operating core calculations. In addition, the computing time comparisons are done for the HZP core.

Chapter 4.3 shows the results obtained from the APR1400 PWR initial core. It is to confirm that the core calculation results which are consistent with the observations in **Chapter 4.2** can be obtained from the different problem. Based on the results for the APR1400 PWR core problems, it can be concluded that the high-fidelity TSCC strategies established in this work is successfully validated.

4.1. KAIST 1A Benchmark

For the KAIST 1A cores whose configurations are detailed in **Chapter 2**, the diffusion and SP₃ FDM and SENM calculations were performed first and the results were compared with the nTRACER reference. The FDM calculations based on 2x2 meshes per pin-cell were also performed to observe the effect of spatial discretization error in the PHMGCs. Note that only the SA based SPH factors were used without the ADF. The results are summarized in **Table 4.1** for the ARO and **Table 4.2** for the ARI. **Figure 4.1** and **Figure 4.2** are to detail the dependence of the errors to the degree of the transport approximation and the discretization method. The diffusion results are denoted by SP₁ for convenience.

Table 4.1. Results of the KAIST 1A ARO core calculations (Ref. k-eff: 1.132102)

Grp.	Solver		$\Delta\rho$ (pcm)	Pin ΔP (%)	
				RMS	MAX
4G	SP ₁	1x1 FDM	72.1	0.98	6.84
		2x2 FDM	70.2	0.69	2.63
		SENM	69.8	0.79	3.04
	SP ₃	1x1 FDM	92.4	1.44	10.50
		2x2 FDM	90.1	0.89	5.13
		SENM	89.7	0.76	2.66
8G	SP ₁	1x1 FDM	46.7	0.96	7.61
		2x2 FDM	45.5	0.59	2.39
		SENM	45.4	0.68	2.62
	SP ₃	1x1 FDM	76.8	1.39	11.16
		2x2 FDM	75.2	0.76	5.82
		SENM	75.2	0.58	3.45
16G	SP ₁	1x1 FDM	27.1	0.62	3.80
		2x2 FDM	22.1	0.63	2.75
		SENM	20.5	0.90	5.39
	SP ₃	1x1 FDM	61.4	0.99	7.40
		2x2 FDM	56.4	0.28	1.58
		SENM	54.5	0.29	1.36

Table 4.2. Results of the KAIST 1A ARI core calculations (Ref. k-eff: 0.976441)

Grp.	Solver		$\Delta\rho$ (pcm)	Pin ΔP (%)	
				RMS	MAX
4G	SP ₁	1x1 FDM	78.9	1.01	6.70
		2x2 FDM	88.4	0.67	2.77
		SENM	92.8	0.70	3.20
	SP ₃	1x1 FDM	184.4	1.62	8.63
		2x2 FDM	192.2	1.23	5.33
		SENM	197.1	1.15	3.97
8G	SP ₁	1x1 FDM	-55.2	1.43	9.31
		2x2 FDM	-46.5	1.15	4.55
		SENM	-42.1	1.13	4.27
	SP ₃	1x1 FDM	99.1	1.37	9.72
		2x2 FDM	106.3	0.82	5.05
		SENM	111.8	0.66	3.29
16G	SP ₁	1x1 FDM	-96.7	1.35	6.58
		2x2 FDM	-91.3	1.27	4.66
		SENM	-87.8	1.34	4.86
	SP ₃	1x1 FDM	63.5	0.95	7.12
		2x2 FDM	67.3	0.35	1.83
		SENM	70.6	0.32	1.32

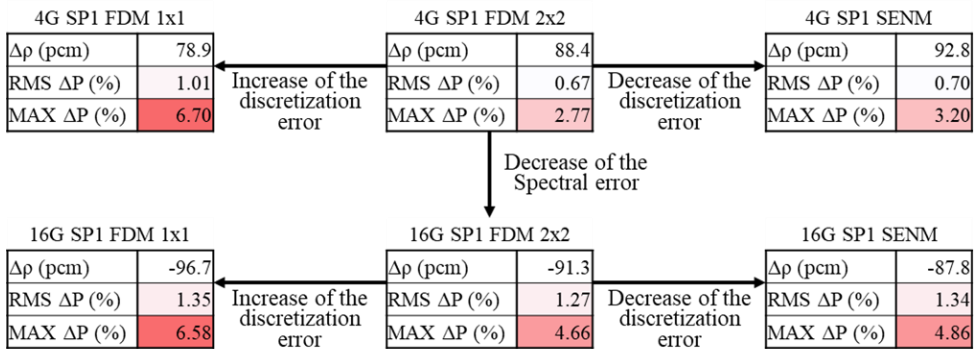


Figure 4.1. Error cancellation of the diffusion calculations for the KAIST 1A ARI

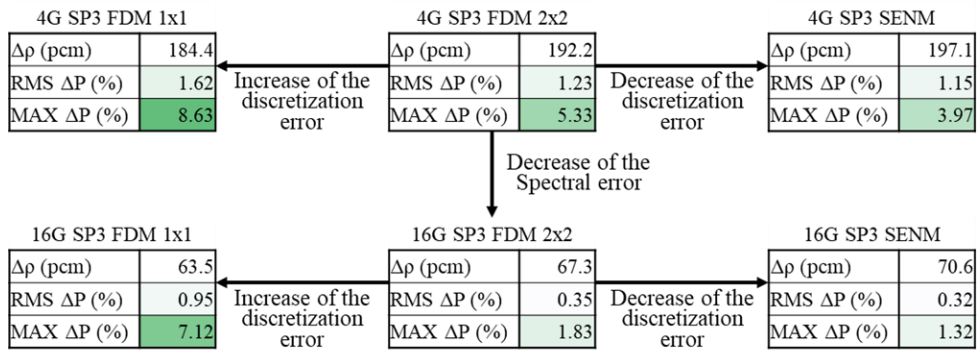


Figure 4.2. Consistent error reduction of the SP₃ calculations for the KAIST 1A ARI

From the tables and figures, it is first noted the diffusion results are not improved by the use of more energy groups. As shown in **Table 4.2** and **Figure 4.1**, the $\Delta\rho$ and RMS/MAX pin ΔP errors for the diffusion SENM obtained from the ARI core are 93 pcm and 0.7%/3.2% for 4G, -42 pcm and 1.1%/4.3% for 8G, and -88 pcm and 1.3%/4.9% for 16G. Furthermore, better spatial discretization does not consistently reduce the error. In case of the 4G diffusion, the $\Delta\rho$ of the SENM is 93 pcm, which are higher than 79 pcm for the 1x1 FDM.

On the contrary, the use of more energy groups gives smaller errors for SP₃. As shown in **Table 4.2** and **Figure 4.2**, the $\Delta\rho$ and RMS/MAX pin ΔP errors of SP₃ SENM obtained from the same ARI core are 197 pcm and 1.2%/4.0% for 4G, 112 pcm and 0.7%/3.3% for 8G, and 71 pcm and 0.3%/1.3% for 16G. Refinement of the meshes improves the SP₃ results as well. The RMS/MAX pin ΔP errors of the 8G calculations are 1.4%/9.7% for 1x1 FDM and 0.8%/5.1% for 2x2 FDM.

Figure 4.3 shows the radial pin ΔP distributions obtained by the different solvers and energy groups. It is clear that the pin ΔP errors considerably are decreased and localized to the assembly boundaries by using more energy groups and elaborated discretization methods in the SP₃ calculations, whereas the errors are large and globally appear in the diffusion cases regardless of the number of energy groups. It would be worthwhile to note that the pin ΔP distributions of SP₃ are similar with the spectral error distributions given in **Figure 2.14**, and the RMS/MAX ΔP errors are

close to the total spectral errors given in **Table 2.4**. In the 8 and 16G cases, the RMS/MAX relative pin ΔP errors originating from the total spectral error were about 0.7%/4.7% and 0.3%/1.5%, and the relative errors of the SP₃ SENM are 0.5%/2.0% and 0.3%/2.0%. It implies that SP₃ SENM successfully reproduces the core fluxes with the SA SPH factors so that only the spectral error in the PHXSs remain. On the other hand, the diffusion solvers and the SP₃ 1x1 FDM yielded considerably large errors due to the transport and discretization errors.

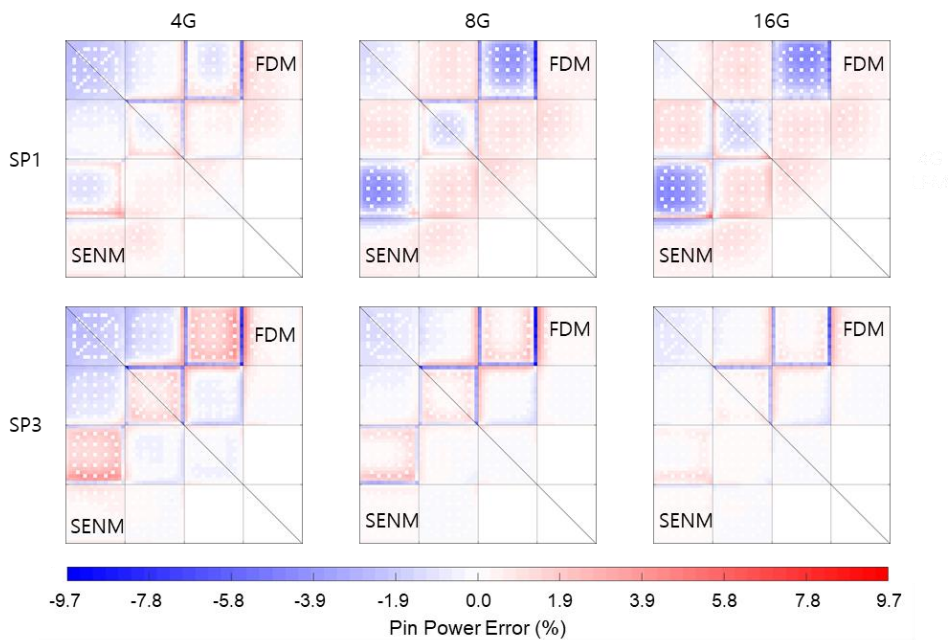


Figure 4.3. Pin power error (%) distributions for the KAIST 1A ARI core

In that the SP₃ SENM calculation results are sufficiently accurate, the SP₅ SENM solver failed to yield a notable improvement. In case of the 8G ARI core calculation, the $\Delta\rho$ and RMS/MAX pin ΔP errors are 112 pcm and 0.7%/3.3% for SP₃ SENM and 111 pcm and 0.7%/3.2% for SP₅ SENM. The results are reasonable because the SP₃ SENM errors are already close to the total spectral errors.

The marginal difference between the SP₃ and SP₅ clearly indicate that a spectral

leakage correction is required for further improvement. Therefore, the diffusion and SP₃ calculations were performed with the FDM and SENM solvers and the results were compare with the nTRACER reference. Note that the SPH factors are normalized by the ADF, and the FDM results are based on a mesh per pin. The results are for the ARO core are presented in **Table 4.3** and **Figure 4.4**.

Table 4.3. Results of the KAIST 1A ARO core calculations without and with the pinwise LFM (Ref. k-eff: 1.132102)

Grp.	Solver		$\Delta\rho$ (pcm)	Pin ΔP (%)	
				RMS	MAX
4G	SP ₁	FDM	73.5	1.42	10.90
		SENM	72.6	0.66	3.86
	LFM	FDM	35.4	0.64	4.99
		SENM	39.8	0.90	3.51
	SP ₃	FDM	91.0	1.90	14.35
		SENM	89.6	0.98	6.92
	LFM	FDM	38.7	1.08	8.64
		SENM	43.1	0.44	1.88
8G	SP ₁	FDM	47.5	1.39	11.38
		SENM	47.5	0.58	4.28
	LFM	FDM	-13.7	0.73	4.85
		SENM	-13.2	0.74	3.29
	SP ₃	FDM	74.1	1.87	14.75
		SENM	73.7	0.90	7.31
	LFM	FDM	8.8	1.17	8.91
		SENM	9.3	0.21	1.10
16G	SP ₁	FDM	28.6	1.08	7.97
		SENM	24.1	0.43	1.09
	LFM	FDM	-18.7	0.96	6.28
		SENM	-22.0	0.64	2.19
	SP ₃	FDM	59.0	1.58	11.70
		SENM	54.3	0.50	3.35
	LFM	FDM	7.3	1.42	10.13
		SENM	3.9	0.36	1.68

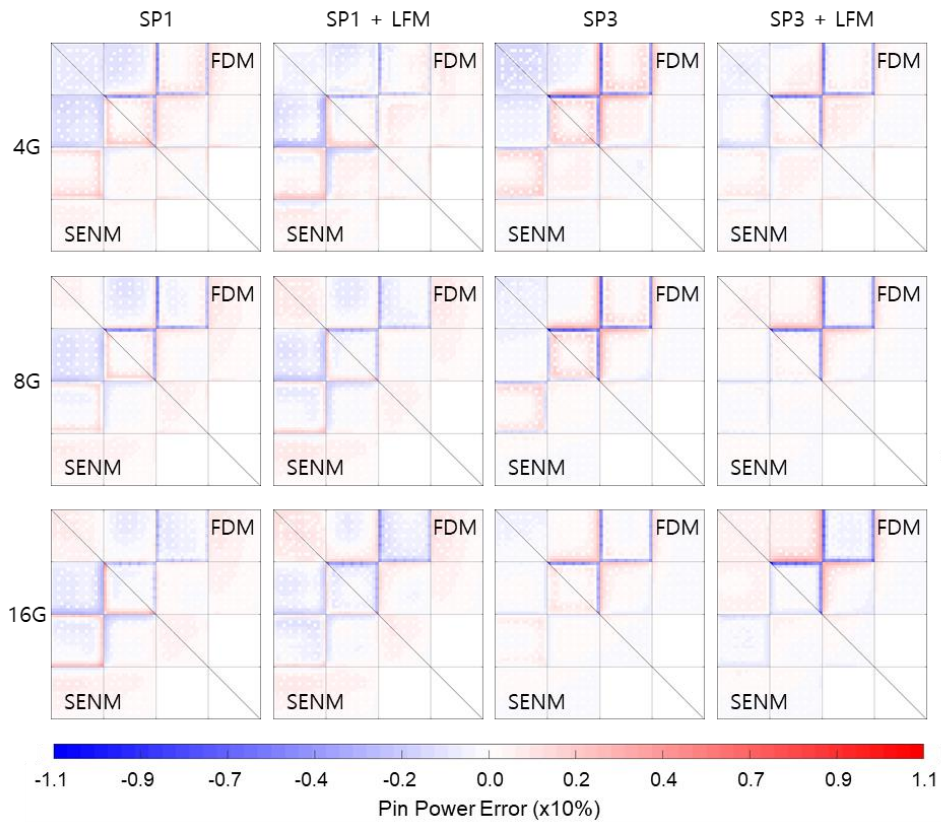


Figure 4.4. Radial pin power error (%) distributions for the KAIST 1A ARO core obtained by different solvers without and with the pinwise LFM

From **Table 4.3** and **Figure 4.4**, it is clearly noted that the pinwise LFM should be coupled with the optimal solution method to accurately reproduce the reference solutions. In case of the 8G diffusion calculations, for example, the RMS/MAX pin ΔP errors are 1.4%/11.4% for the FDM and 0.6%/4.3% for the SENM. Those are decreased to 0.7%/4.9% for the FDM and 0.7%/3.3% for the SENM, by applying the pinwise LFM. The remaining errors are still notable since the diffusion involves significantly large transport error which increases the inconsistency of the SA based SPH factors in the core. It is worthwhile to note that the 8G diffusion calculation results corrected by the LFM are similar with the results presented in **Table 2.17** and **Figure 2.34**, which are based on the core PHXSs and the SA SPH factors. It means that the errors originate from the inconsistent SPH factors.

In case of the 8G SP₃ calculations, on the other hand, the RMS/MAX pin ΔP errors are 1.9%/14.8% for the FDM and 0.9%/7.3% for the SENM, and those are decreased to 1.2%/8.9% for the FDM and 0.2%/1.1% for the SENM by applying the LFM. It is quite obvious that the remarkably large errors of the SP₃ FDM originate from the discretization error. For the SP₃ calculations, the errors are also close to the results in **Table 2.17** and **Figure 2.34**. It indicates that the solution improvement of the SP₃ SENM over the diffusion and the SP₃ FDM results from the less inconsistent SPH factors obtained by the optimal solver and the spectral error is successfully corrected by the LFM. In conclusion, the high-fidelity pinwise TSCC strategy based on the optimal solver and the leakage correction is validated for the small core.

4.2. AP1000 PWR Initial Core

The AP1000 PWR first core is loaded with 157 FAs of 17x17 lattices containing 264 fuel rods, 24 guide tubes (GTs) and 1 instrument tube (IT), with a power rating of 3400 MWth. The assemblies are grouped into Region 1 – 5 according to U-235 enrichment ranging from 0.74 (natural U) to 4.80%. Region 1, 2 and 3 FAs have radially uniform fuel enrichment while Region 4 and 5 FAs have enrichment zoning. Region 4 and 5 FAs are also equipped with two types of BAs: IFBA and WABA, which are a ZrB₂ coating on the pellets of selected fuel rods and an insert with an internal hole filled with coolant. The FA specifications are summarized in **Table 4.4**. In the table, *Total*, *IFBA*, and *WABA* indicate the number of FAs loaded in the core, IFBA fuel pins per assembly, and WABA inserts per assembly per type. Note that the WABA inserts are axially asymmetric, and designated by the long (L), intermediate (I), and short (S) WABA according to the height of Al₂O₃-B₄C absorber bearing part, as shown in **Figure 4.5**. *U-235 mid-zone* and *U-235 blanket* indicate the fuel enrichment for the mid-zone and axial blanket region of each fuel pin. The axial blanket is un-poisoned lower enriched region at the top and bottom of the fuel rods, except for the 0.74 and 1.58% fuels.

Table 4.4. Fuel assembly specifications of the AP1000 PWR initial core

Reg. #	Total #	U-235 mid-zone (%)	U-235 blanket (%)	IFBA	WABA
1	16	0.74			
2	49	1.58			
3	28	3.20	1.58		
4	36	3.40 / 3.80 / 4.20	3.20	68	8L + 4S
5A	8	4.00 / 4.40 / 4.80	3.20	88	4I
5B	4	4.00 / 4.40 / 4.80	3.20	124	
5C	16	4.00 / 4.40 / 4.80	3.20	124	8I

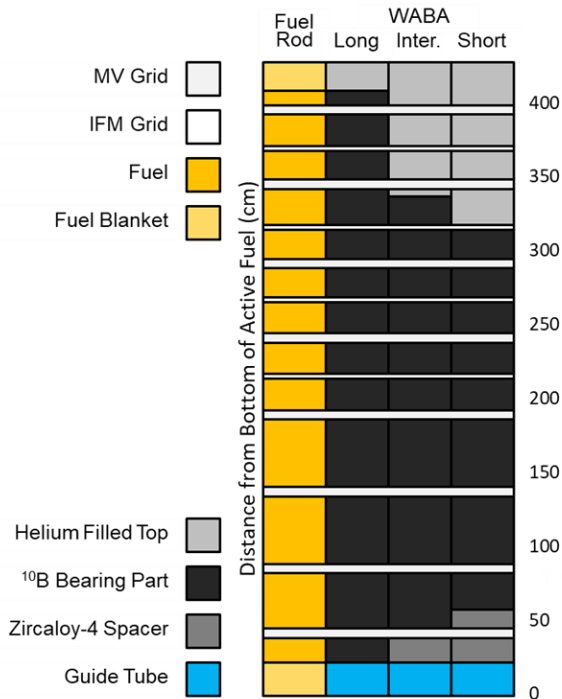


Figure 4.5. Heterogeneous axial configurations of the AP1000 PWR initial core

The AP1000 PWR first core is designed to utilize two different types of rod cluster control assemblies (RCCAs). Black RCCAs employ the typical Ag-In-Cd (AIC) mixture while Gray RCCAs employ tungsten which is to minimize the impact on the

power distribution. The tungsten absorber is applied for MA, MB, MC, and MD RCCAs. The core loading pattern and RCCA map are shown in **Figure 4.6** with the specification of Region 4 FA forming the CB pattern of the core inner part.

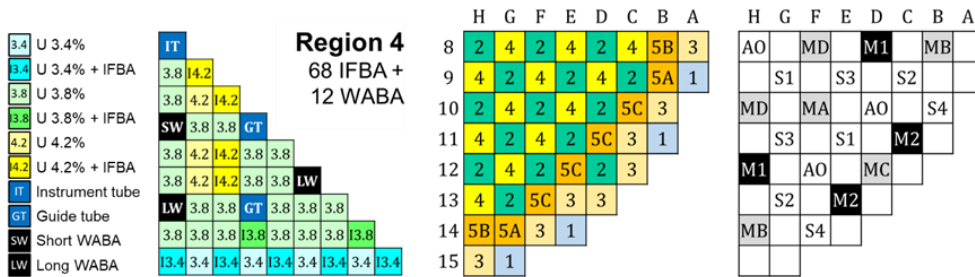


Figure 4.6. Region 4 FA specification (left), core loading pattern (center), and the RCCA map (right) of the AP1000 PWR initial core

The AP1000 PWR initial core is a highly adequate test problem in that the core is not only radially but also axially heterogeneous. For the radial direction, the wide range of fuel enrichment, the IFBA pin-cells loaded along the assembly boundaries, and a number of WABA inserts render a remarkably large heterogeneity. Resultantly, the spectral error is notably large, as shown in **Figure 4.7**. Note that the spectral error for each energy group case is quantified by following the procedure described in **Chapter 2.2**. Even for the 8G, the MAX relative pin ΔP due to the total spectral error is about 2.0% and it appears at the core inner part where the pin power is high. Thus, the applicability of the pinwise LFM for the large commercial core can be examined, as well as the accuracy of the lower order solvers.

For the axial direction, on the other hand, the axially asymmetric configuration of WABA results in unusual axial power distribution shapes. The examples are given in **Figure 4.8**. Compared to Region 5B without WABA, the axial power profiles of Region 4, 5A, and 5C are skew to the top at the HZP state and those are distorted again by the T/H effect at the HFP. In addition to the difficulty, it should be noted that the solution agreements in the axial direction is solely determined by the solver because the SPH factors are obtained from the 2D configurations. Therefore, the

accuracy of the axial flux solver and the T/H solver can be thoroughly analyzed, and the results obtained from this core can be generalized for typical PWRs.

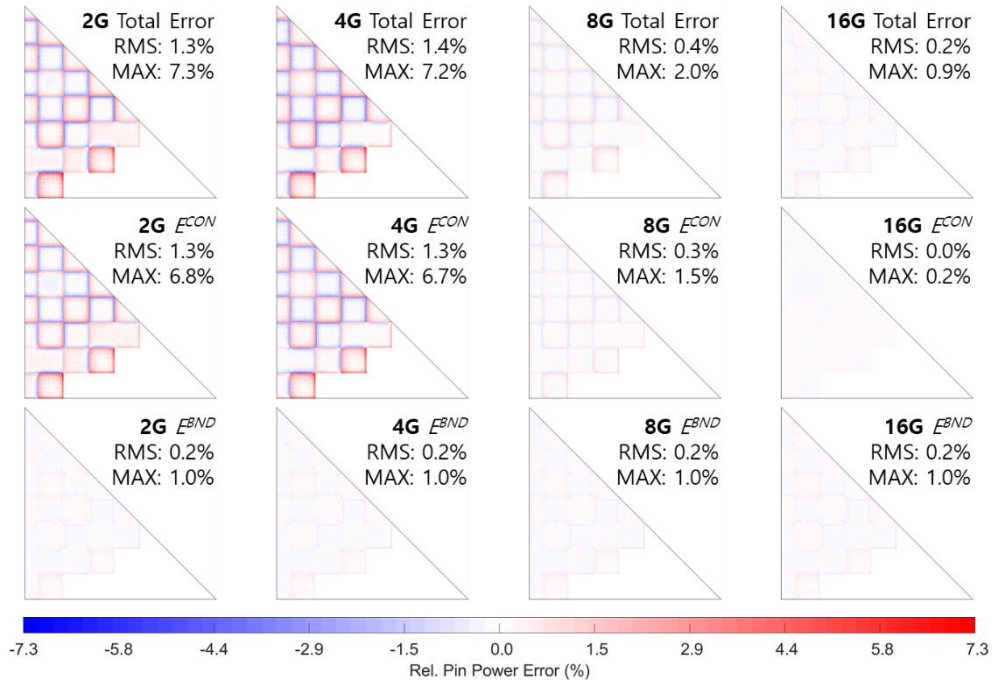


Figure 4.7. Relative pin power error (%) distributions for the AP1000 PWR 2D HZP core due to the total spectral error (top), group condensation error (middle), and boundary spectral error (bottom)

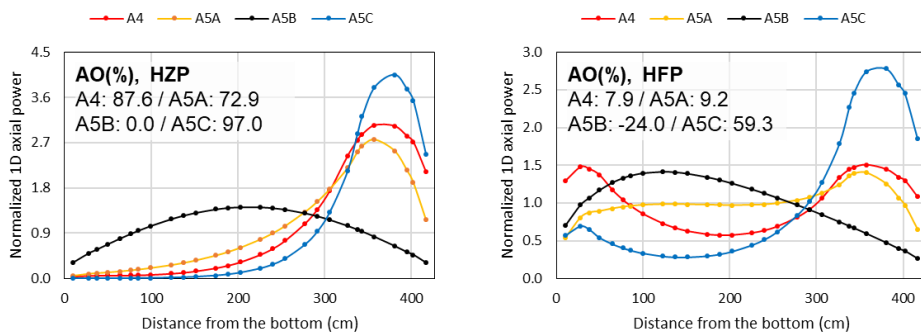


Figure 4.8. Radially averaged axial 1D power distributions of the AP1000 PWR assemblies at the HZP (left) and the HFP (right) states

4.2.1. Results of the 2D HZP core calculations

For the AP1000 PWR 2D HZP ARO core at the initial steady state, the diffusion and SP₃ calculation were performed with the FDM and SENM solvers. Note that the rodDED core calculations were also performed but no notable difference in the results were observed. The results are presented in **Table 4.5** and **Figure 4.9**.

Table 4.5. Results of the AP1000 PWR 2D HZP ARO core calculations without and with the pinwise LFM (Ref. k-eff: 1.000014)

Grp.	Solver		$\Delta\rho$ (pcm)	Pin ΔP (%)	
				RMS	MAX
4G	SP ₁	FDM	23.3	1.53	5.92
		SENM	28.6	1.07	4.56
	SP ₁	FDM	2.8	0.58	1.72
		LFM	SENM	5.0	0.84
	SP ₃	FDM	44.8	2.19	7.74
		SENM	49.4	1.73	6.16
	SP ₃	FDM	26.3	0.68	2.72
		LFM	SENM	27.0	0.42
8G	SP ₁	FDM	-30.1	1.08	2.93
		SENM	-23.9	0.70	1.60
	SP ₁	FDM	-32.7	1.04	2.30
		LFM	SENM	-25.7	1.11
	SP ₃	FDM	0.3	1.47	5.07
		SENM	6.0	0.83	2.90
	SP ₃	FDM	-3.4	0.87	3.04
		LFM	SENM	3.0	0.31
16G	SP ₁	FDM	-36.9	1.03	2.51
		SENM	-29.9	0.85	1.91
	SP ₁	FDM	-42.6	1.18	2.50
		LFM	SENM	-34.9	1.18
	SP ₃	FDM	-7.5	1.23	4.20
		SENM	-1.1	0.60	2.05
	SP ₃	FDM	-13.8	1.01	3.26
		LFM	SENM	-6.9	0.42

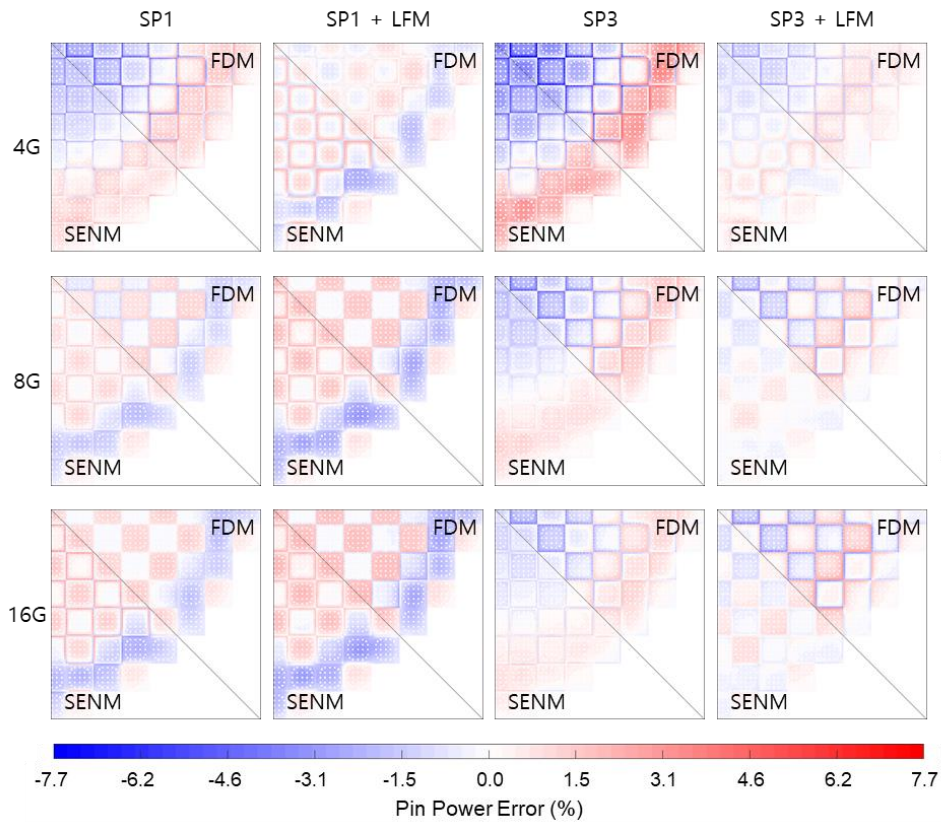


Figure 4.9. Radial pin power error (%) distributions for the AP1000 PWR 2D HZP ARO core obtained by different solvers

It is noted in **Table 4.5** that the diffusion results are not monotonously improved by the use of more energy groups. The $\Delta\rho$ and RMS/MAX pin ΔP errors of the diffusion SENM are 29 pcm and 1.1%/4.6% for the 4G, -24 pcm and 0.7%/1.6% for the 8G, and -30 pcm and 0.9%/1.9% for the 16G. Although the use of the SENM solver instead of the FDM slightly improved the results, the errors are still large. On the contrary, the SP₃ results are clearly improved with more energy groups. The $\Delta\rho$ and RMS/MAX pin $\Delta\rho$ error of SP₃ SENM are 49 pcm and 1.7%/6.2% for the 4G, 6 pcm and 0.8%/2.9% for the 8G, and -1 pcm and 0.6%/2.1% for 16G. The better discretization also reduces the error. For 8 and 16G cases, the MAX pin ΔP errors are 5.1% and 4.2% for 1x1 FDM and 2.9% and 2.1% for SENM. **Figure 4.9** shows that the pin ΔP errors are reduced and localized with more energy groups and the

better discretization in the SP_3 whereas the pattern of the pin ΔP distribution only changes without magnitude reduction in the diffusion.

The solution improvement yielded by the LFM is remarkable. In case of the SP_3 SENM calculations, the RMS/MAX pin ΔP errors are decreased from 1.7%/6.2% to 0.4%/1.1% for the 4G and from 0.8%/2.9% to 0.3%/0.9% for the 8G. The SP_3 FDM results are also improved but the remaining errors are still large in that the coarse mesh FDM solver involves large discretization error. In contrast, the errors are rather increased with the diffusion solver. In case of the diffusion SENM calculation, the RMS/MAX pin ΔP errors are increased from 0.7%/1.6% to 1.1%/2.7% for the 8G and from 0.9%/1.9% to 1.2%/2.7% for the 16G, because the error cancellation is weakened as the spectral error is reduced.

Noting that the core calculation results are consistent with the results obtained from the KAIST 1A problems, the core depletion calculations were performed. In order to estimate the errors during Cycle 1 depletion which originate from the use of different depletion libraries, the SA depletion calculations were performed first with the VANGARD code and the results were compared with the nTRACER reference. **Figure 4.10** and **Figure 4.11** presents the depletion results for the Region 2 and 4 FAs up to 30GWD/tHM. Region 2 represents the un-poisoned FAs with the uniform fuel enrichment and Region 4 represent the heterogeneous FAs which involve the BAs and the enrichment zoning. Although the results presented in the figures are yielded by the SP_3 SENM solver based on the 16G PHXSs, it should be noted that the results obtained by different solvers and based on the different energy groups are essentially similar in that the SA based SPH factors can capture the errors associated with the solution method and the group condensation.

Regardless of the FA configuration, the depletion results are satisfactory in that the $\Delta\rho$ error due to the depletion library does not exceed 30 pcm up to 20 GWD/tHM of the FA burnup. Note that the good agreements are consistent with the SA depletion results in Ref. [18]. Based on the results, the core depletions were performed.

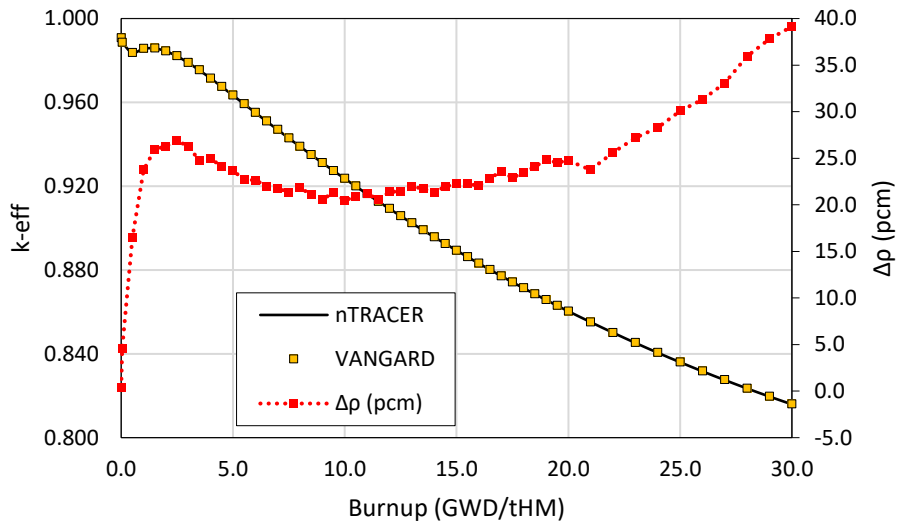


Figure 4.10. Depletion results for the AP1000 Region 2 FA

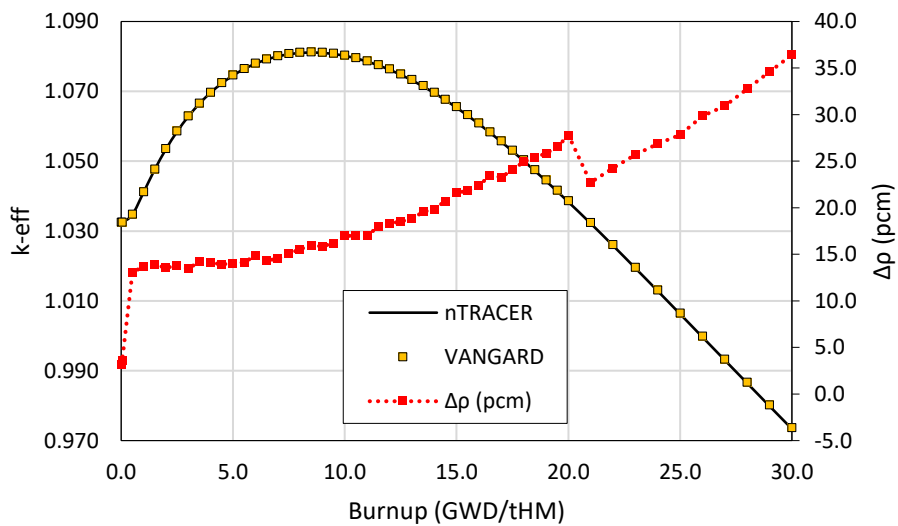


Figure 4.11. Depletion results of the AP1000 Region 4 FA

The core depletion results obtained with the SP₃ SENM solver are summarized in **Figure 4.12** and **Figure 4.13**. Note that the similar behaviors of the $\Delta\rho$ and MAX pin ΔP errors depending on the burnup are yielded by different solvers, such as the diffusion SENM. The results clearly reveal the good agreements of the SP₃ SENM

solver and demonstrate that the pinwise LFM is applicable for the depletion. In case of the 4G, for example, the MAX pin ΔP is decreased from 5.1% to 1.2% so that comparable to 1.3% for the 16G, and the Δp is also reduced. **Figure 4.14** shows that the pinwise LFM successfully corrects the pin ΔP error during the depletion.

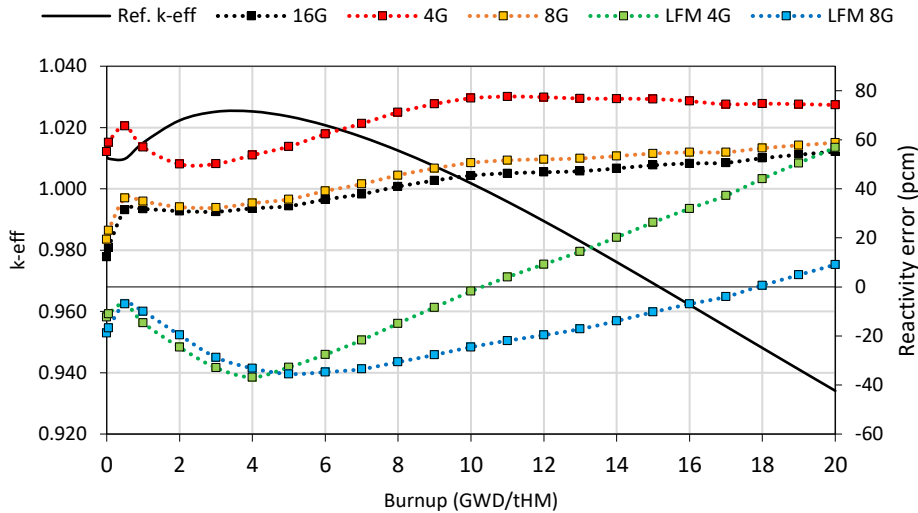


Figure 4.12. The k-eff curve and the reactivity error (pcm) for the AP1000 PWR 2D HZP ARO core depletions obtained with the SP₃ SENM solver

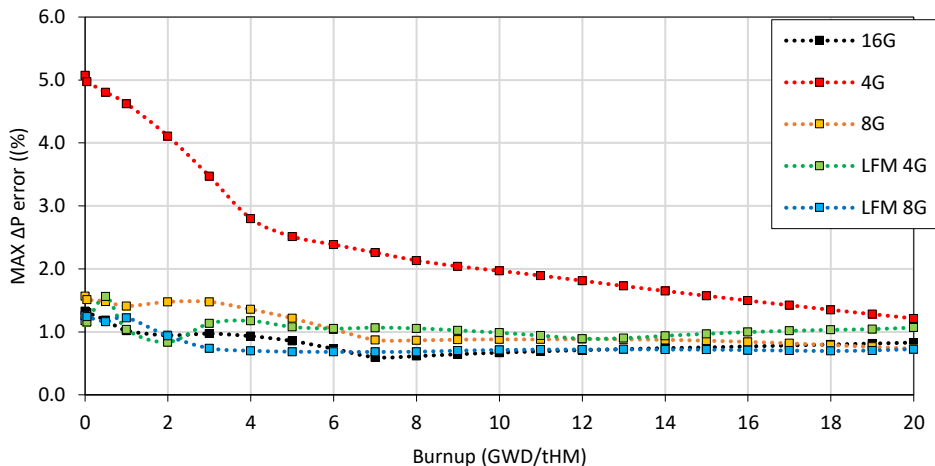


Figure 4.13. The MAX pin ΔP errors (%) for the AP1000 PWR 2D HZP ARO core depletions obtained with the SP₃ SENM solver

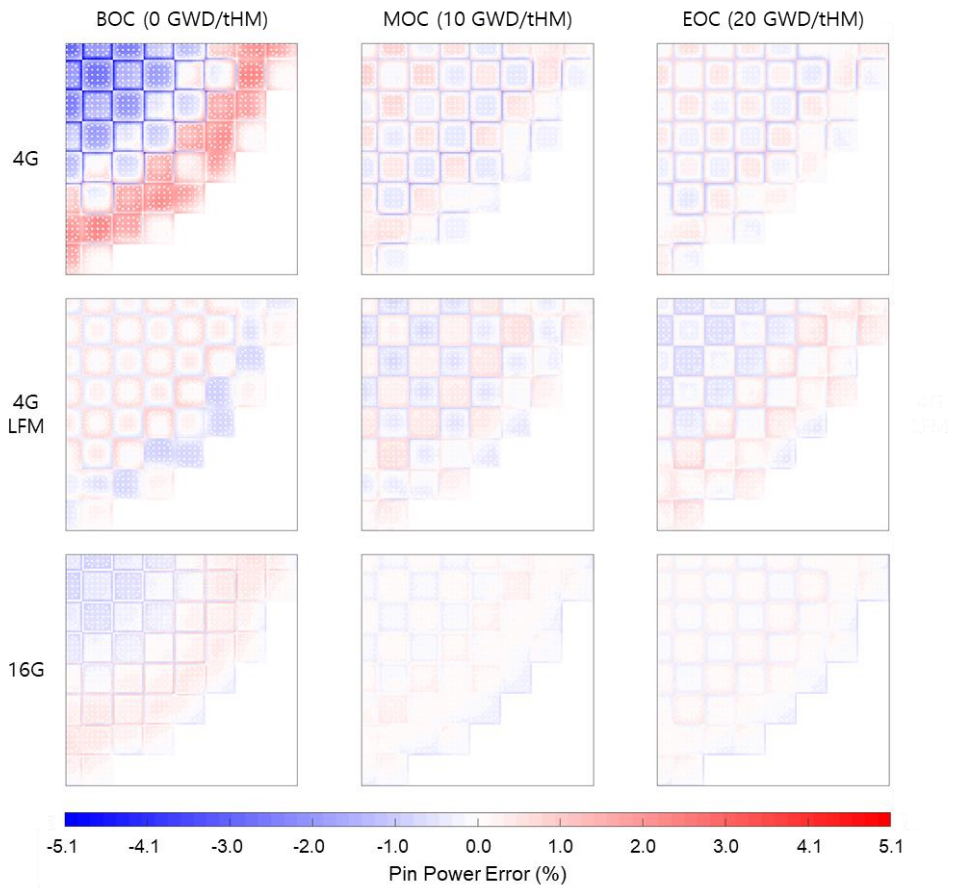


Figure 4.14. Radial pin power error (%) distributions for the AP1000 PWR 2D HZP ARO core depletions obtained with the SP₃ SENM solver

4.2.2. Results of the 3D single assembly calculations

The error analysis for the 3D SAs revealed that the pin ΔP due to the spectral error introduced by the PHXSs based on the 2D configurations does not exceed 0.7%, even with the 4G. It is also noted that the radial pin ΔP error is less than about 0.1% regardless of the solver and the number of energy group, since the 2D SA based SPH factors can successfully capture the errors in the radial direction. Therefore, the 3D FA problems are highly adequate for examination of the axial flux solver and the T/H solver. In this regard, the test calculations were performed first for the 3D HZP FAs with the diffusion and SP₃ solvers.

Table 4.6. Results of the AP1000 Region 4 3D HZP FA calculations

Grp.	Solver	$\Delta\rho$ (pcm)	2D Pin ΔP (%)		Axial ΔP (%)		
			RMS	MAX	RMS	MAX	
4G	SP ₁	CM FDM	-51.4	0.03	0.08	3.32	10.72
		FM FDM	-44.2	0.03	0.07	2.77	8.69
		SENM	-20.1	0.01	0.05	1.60	5.25
	SP ₃	CM FDM	-31.4	0.02	0.05	1.97	6.75
		FM FDM	-24.5	0.01	0.04	1.44	5.28
		SENM	-3.0	0.01	0.03	0.41	1.70
8G	SP ₁	CM FDM	-45.6	0.03	0.07	3.29	11.40
		FM FDM	-37.7	0.02	0.06	2.68	9.21
		SENM	-9.4	0.01	0.05	1.30	4.91
	SP ₃	CM FDM	-15.1	0.01	0.02	1.23	4.15
		FM FDM	-7.4	0.00	0.01	0.64	2.51
		SENM	17.9	0.02	0.04	0.80	2.26
16G	SP ₁	CM FDM	-53.2	0.04	0.09	3.76	12.84
		FM FDM	-45.3	0.03	0.08	3.14	10.63
		SENM	-13.7	0.01	0.05	1.47	5.41
	SP ₃	CM FDM	-23.4	0.01	0.04	1.74	5.75
		FM FDM	-15.7	0.01	0.03	1.14	3.99
		SENM	12.9	0.01	0.04	0.64	1.96

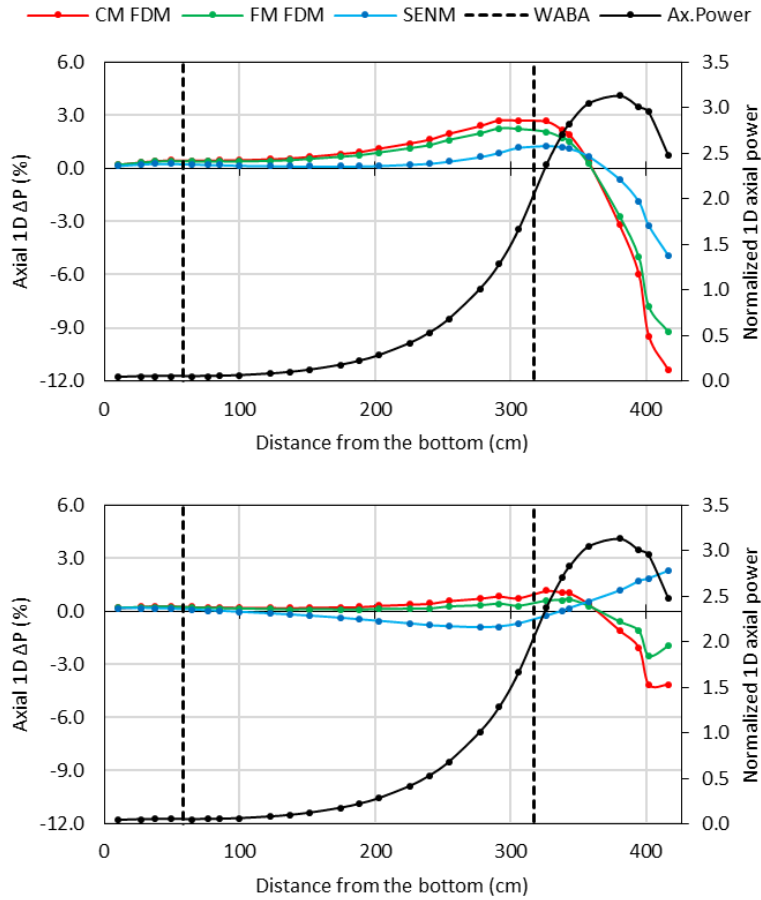


Figure 4.15. Axial 1D power and ΔP (%) distributions of the HZP Region 4 FA with the diffusion (top) and SP_3 (bottom) FDM and SENM solvers

The results for the Region 4 HZP FA are summarized in **Table 4.6**. The diffusion is denoted by SP_1 for convenience, and *CM FDM* and *FM FDM* indicate that the axial FDM mesh sizes are 2cm and 1cm, respectively. The axial transverse leakage expansion scheme [18] is used for the FDM calculations in order to reduce the errors associated with the use of coarse axial planes. The table presents the 4, 8, and 16G results and the radial ΔP errors as well to confirm that the number of energy groups slightly affects the SA calculation results and the radial pin ΔP is sufficiently small to neglect. **Figure 4.15** presents the axial pin power and ΔP distributions obtained by the 8G calculations for Region 4.

From the table and figure, it is noted that the sufficiently high order solver is needed to obtain the accurate results for the axially heterogeneous problem. In case of the 8G calculations, the RMS/MAX axial ΔP errors are 0.8%/2.3% for the SP₃ SENM, and increased to 1.2%/4.2% for the CM SP₃ FDM due to the discretization error and to 1.3%/4.9% for the FM diffusion due to the transport error. The errors are the largest for the CM diffusion FDM, which yielded 3.3%/11.4%, because the two errors are both severe. Note that the solvers yielded no notable difference for the FAs without WABA. It means that a very low order solver can yield acceptable results for typical reactor core problems.

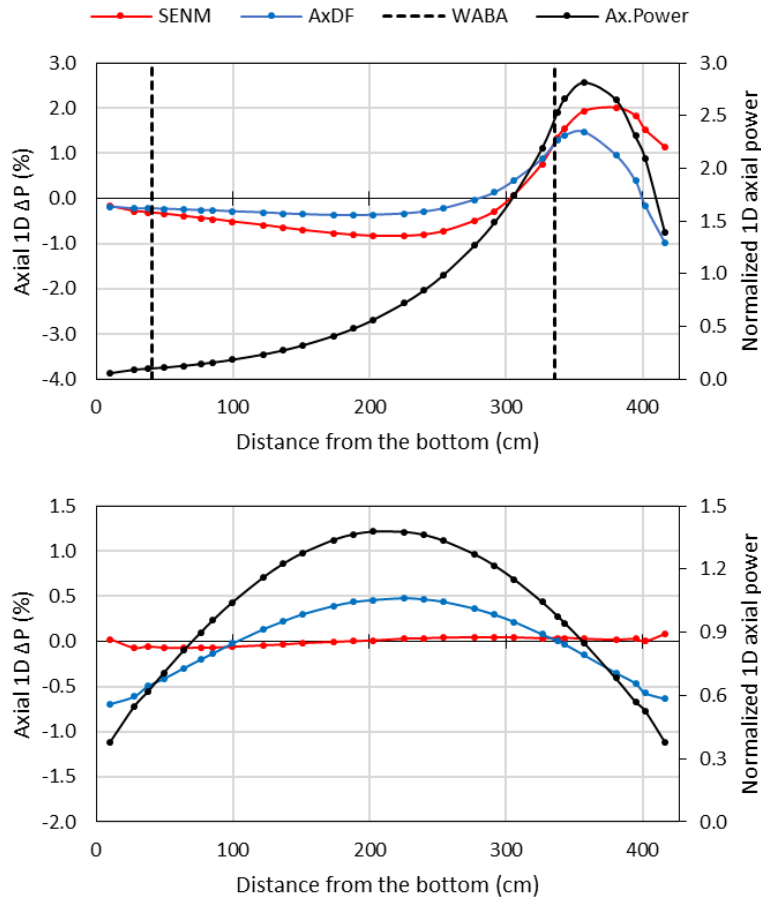


Figure 4.16. Effect of the axial reflector discontinuity factor on the axial ΔP error for the HZP Region 5A (top) and Region 5B (bottom) FAs

Through the test calculations, the need for axial reflector DF (RDF) is also noted. For the FAs which have cosine shaped axial power profile, the diffusion calculation results with and without RDFs are just slightly different, as noted in Ref. [25]. For the FAs with unusual axial power profiles, on the other hand, RDF quite notably affects the axial power and its effect is more significant with the SP₃ solver. The 8G SP₃ SENM calculation results for Region 5A and 5B presented in **Figure 4.16** are the example. The RMS/MAX axial ΔP errors are decreased from 1.0%/2.0% to 0.6%/1.5% for Region 5A, while the errors are slightly increased from 0.0%/0.1% to 0.4%/0.7% for Region 5B. In that the additional computing cost for the use of the axial RDF is nearly zero while the improvement of the solution agreements are consistently yielded, employment of the RDF is determined.

The 3D HFP FA calculation were then performed to examine the T/H solver. The axial power distributions of the AP1000 FAs are significantly changed by the power level, as shown in **Figure 4.17**, the T/H effect should be properly considered to yield the accurate results under the operating condition. Compared to the assemblywise core calculation, the pinwise flow channel can be employed for the PHMGCs so that the non-uniform moderator temperature effect can be explicitly considered, but the temperature profile within the fuel pellet is still remained as an issue. For this reason, three formulas to determine the effective fuel temperature, namely the NEA [31], CEA [32], and Studsvik [33] formulas, were examined. The SP₃ SENM solver was employed with the 16G PHXSs to minimize the errors other than the T/H.

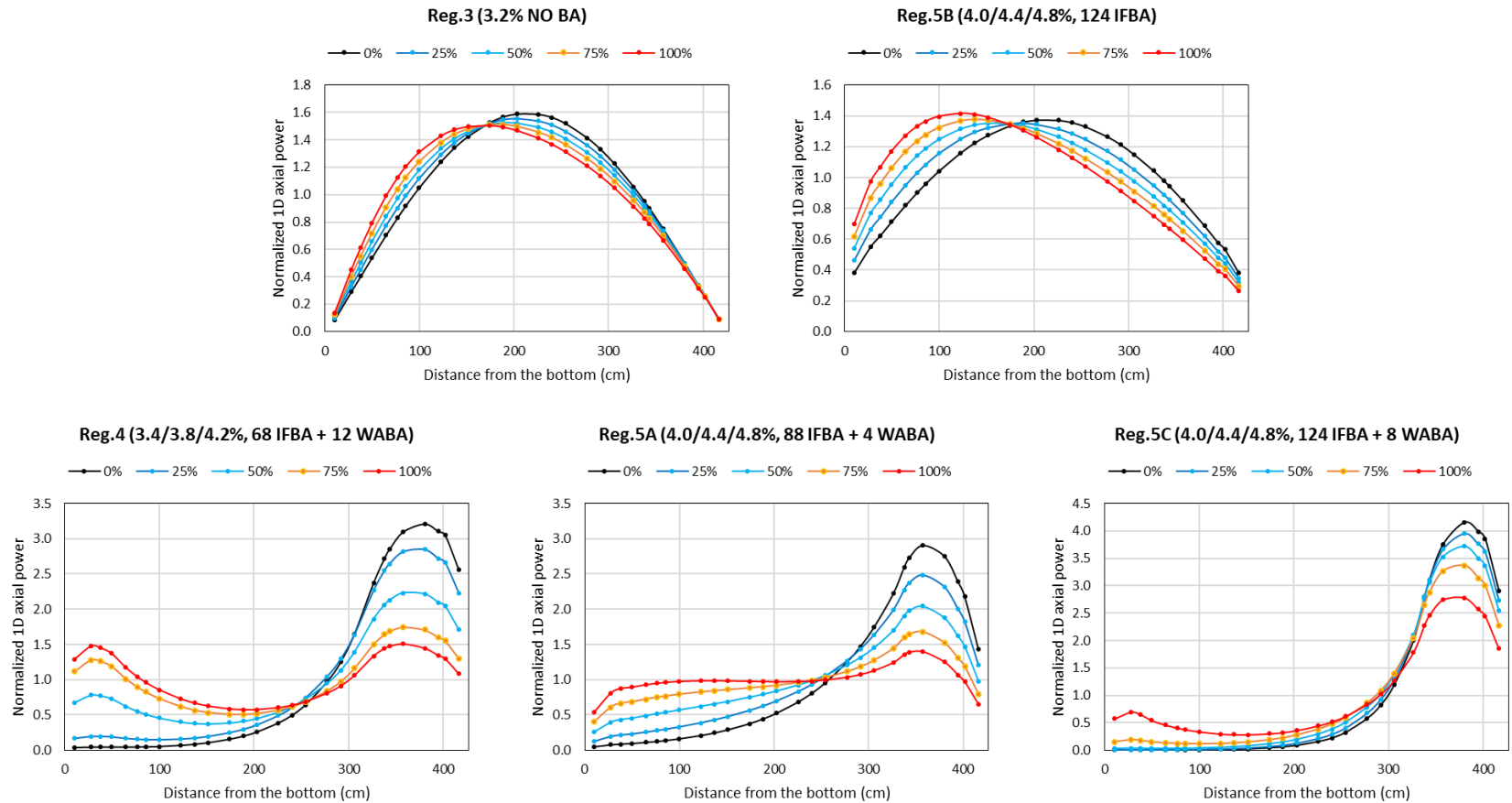


Figure 4.17. Axial 1D power distributions at the different power levels

The NEA formula had been used in VANGARD. It determines the effective fuel temperature (T_{eff}) by a weighted sum of the pellet centerline temperature (T_{center}) and the surface temperature (T_{surface}) as:

$$T_{\text{eff}} = (1 - \omega)T_{\text{center}} + \omega T_{\text{surface}}, \quad (4.1)$$

where the weighting factor 0.7 is given. It is the simplest scheme but known that the accuracy is marginal. On the other hand, the Studsvik formula used in SPHINCS employs the volume weighted average fuel temperature (T_{average}) with T_{surface} as:

$$T_{\text{eff}} = \omega T_{\text{average}} + (1 - \omega)T_{\text{surface}}. \quad (4.2)$$

The weighting factor called *Studsvik factor* is to be empirically determined. For the examination of the formulas in this chapter, trial value 0.92 suggested by Grandi [33] was employed and then the optimal value was selected by a further investigation. In that the variation of T_{average} is not as severe as T_{center} , it is known that the Studsvik formula yields more accurate results.

In addition to the two formulas which have been normally used at SNURPL, the CEA formula is examined. It determines the effective fuel temperature using T_{average} , T_{center} , and T_{surface} without an empirical weighting factor as follow.

$$T_{\text{eff}} = T_{\text{average}} + \frac{1}{18}(T_{\text{center}} - T_{\text{surface}}). \quad (4.3)$$

Figure 4.18 shows the Δp errors obtained from the Region 3 and 4 FAs. The results based on the three formulas are denoted by *NEA*, *CEA*, and *Studsvik*. From the figure, it is first noted that the Δp errors for the NEA rapidly increases as the power level increases, up to 162 pcm for Region 3 and 156 pcm for Region 4, while the errors for the Studsvik are only 30 pcm for Region 3 and 12 pcm for Region 4 at the HFP state. The CEA results are notably better than the NEA but not as much accurate as

the Studsvik, even though the Studsvik factor 0.92 is not the optimal. The $\Delta\rho$ errors for the CEA at the HFP state are 49 pcm for Region 3 and 32 pcm for Region 4.

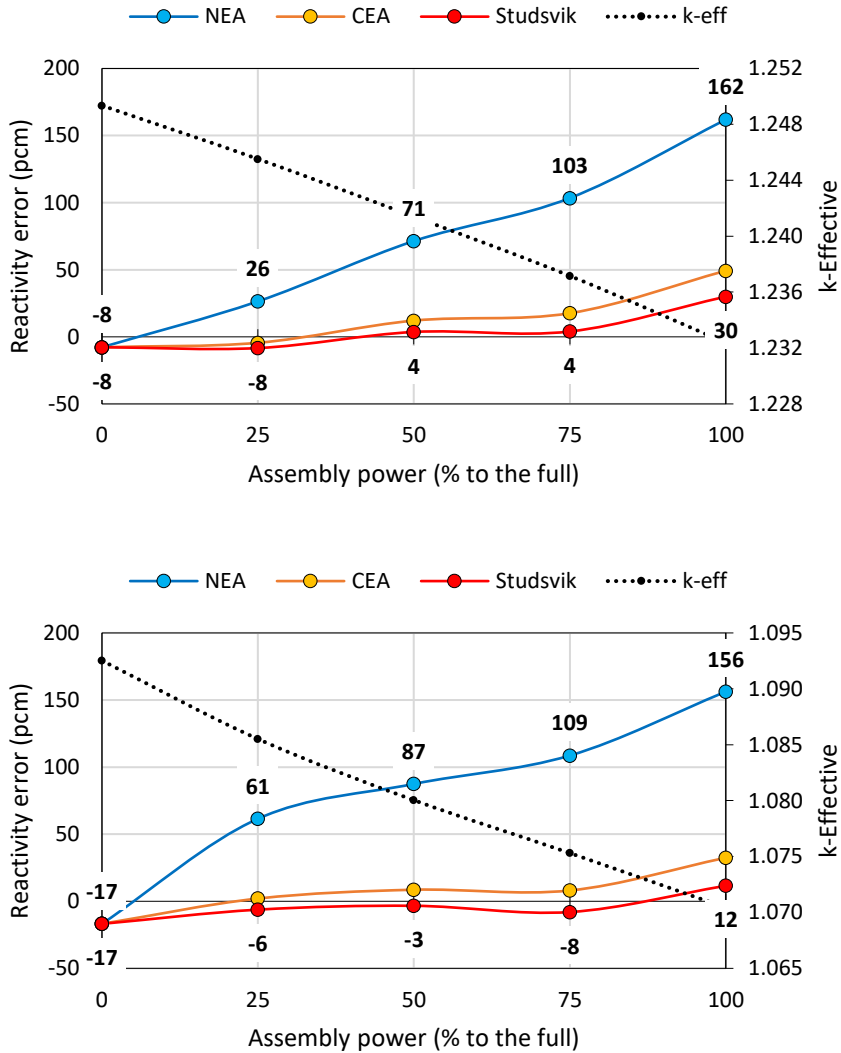


Figure 4.18. Reactivity error (pcm) obtained from Region 3 (top) and 4 (bottom) FAs at different power levels with the three formulas

The axial ΔP corresponding to **Figure 4.18** are presented in **Figure 4.19**. The errors for the NEA severely increases as the power level increases, so the RMS/MAX axial ΔP errors at the HFP state are 1.0%/1.8% for Region 3 and 3.7%/7.4% for

Region 4. On the contrary, the errors for the Studsvik are notably smaller than those. The RMS/MAX axial ΔP errors at the HFP state are 0.7%/1.2% for Region 3 and 1.6%/4.0% for Region 4. The CEA results are highly similar with the Studsvik results so that those are not included in the figure. Based on such results observed from other FAs as well, the Studsvik formula is adopted for VANGARD.

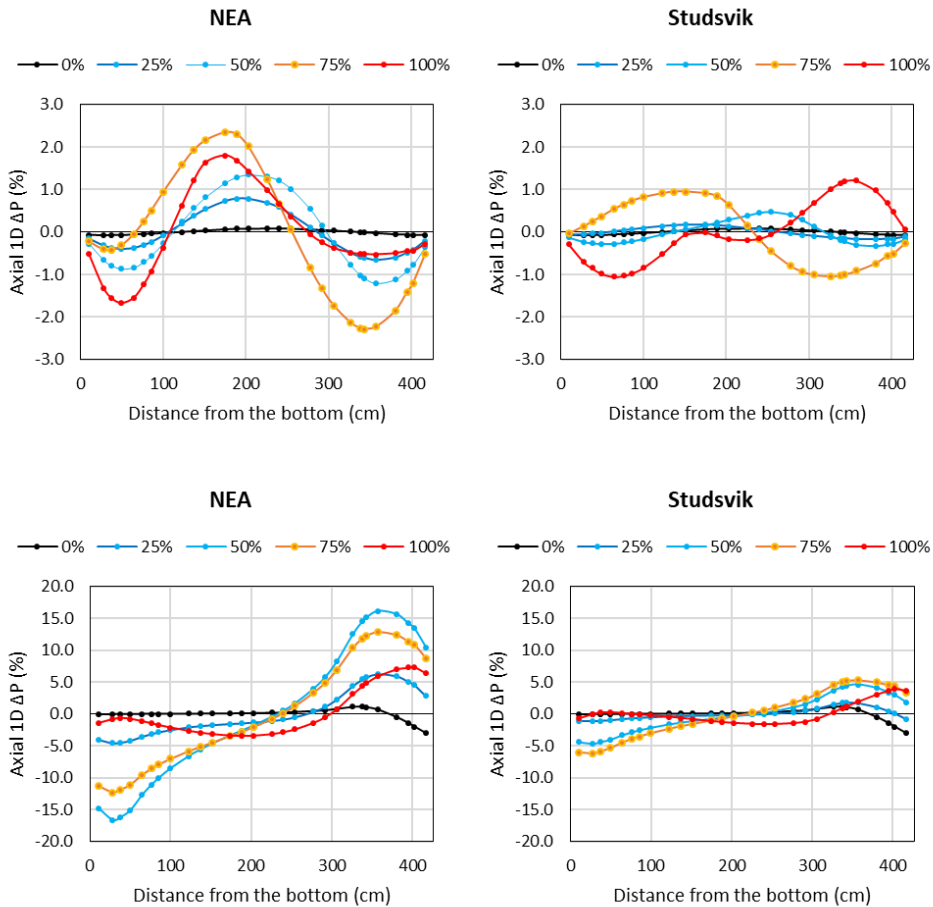


Figure 4.19. Axial ΔP (%) obtained from Region 3 (top) and 4 (bottom) FAs at different power levels with NEA (left) and Studsvik (right) formulas

The optimal Studsvik factor is then determined. By employing the FA calculation results summarized in **Table 4.7**, the core Δp errors are estimated as:

$$\text{RMS } \Delta\rho_{\text{Core}} = \sqrt{\frac{1}{N_{\text{Asy,Total}}} \sum_{\text{AsyType}} N_{\text{iAsy}} (\Delta\rho_{\text{iAsy}})^2}. \quad (4.4)$$

The number of FAs per type are summarized in **Table 4.4**. The absolute $\Delta\rho$ errors for each FAs and the core are presented in **Figure 4.20**. In that the $\Delta\rho$ error is smallest with 0.97, it is selected for the following core T/H calculations.

Table 4.7. Reactivity errors (pcm) obtained with different Studsvik factors

Factor	Reg.2	Reg.3	Reg.4	Reg.5A	Reg.5B	Reg.5C
0.90	31.3	36.1	33.2	59.8	71.7	50.5
0.92	19.9	26.6	22.9	51.0	62.9	36.3
0.95	3.0	12.3	7.6	37.9	49.7	15.5
0.96	-2.7	7.5	2.5	33.5	45.3	8.6
0.97	-8.3	2.8	-2.5	29.1	40.9	1.8
0.98	-13.9	-1.9	-7.6	24.8	36.6	-5.2
0.99	-19.6	-6.6	-12.6	20.4	32.2	-11.8
1.00	-25.2	-11.3	-17.7	16.1	27.9	-18.7

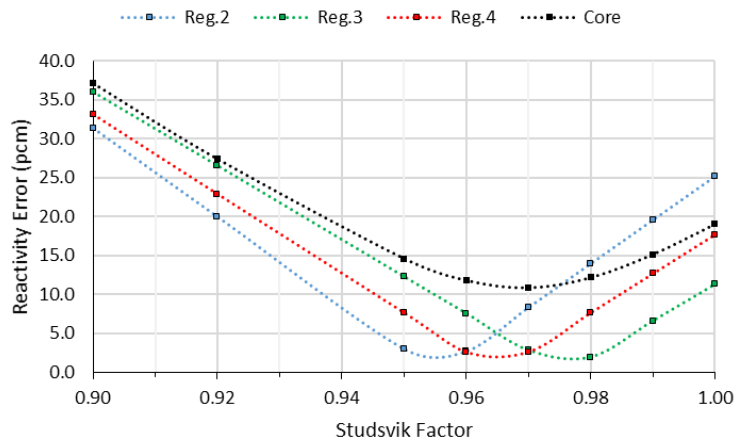


Figure 4.20. Reactivity error (pcm) obtained with different Studsvik factors

4.2.3. Results of the 3D mini-core calculations

The 3x3 mini-core is loaded with 5 Region 2 and 4 Region 4 FAs, as shown in **Figure 4.21**, and the control rods are partially inserted, 57.75cm from the top of the active fuel region, in the central Region 2 FA in order to render a more challenging configuration. The calculations were performed first at the HZP state to examine the solvers for 3D problems representing a part of the core and to confirm that the LFM coefficients obtained from the 2D CBs can be applied for the 3D problem. Then the HFP calculations were performed to estimate that the pinwise LFM is applicable for the operating core calculations, as a preliminary step before the full core.

Region 2 w/o BA	Region 4 68 IFBA + 12 WABA	Region 2 w/o BA
Region 4 68 IFBA + 12 WABA	Region 2 w/o BA Rodded	Region 4 68 IFBA + 12 WABA
Region 2 w/o BA	Region 4 68 IFBA + 12 WABA	Region 2 w/o BA

Figure 4.21. Radial configuration of the 3x3 mini-core

The HZP calculation results are summarized in **Table 4.8**. It is noted that the SP₃ SENM calculation with sufficiently refined energy groups yielded good agreements while the diffusion solvers and the SP₃ FDM solver yielded relatively unsatisfactory results. In case of the 8G calculations, for example, the RMS/MAX pin ΔP errors are 0.1%/0.5% for the SP₃ SENM, and those are followed by 0.4%/0.7% for the diffusion SENM, 0.5%/1.3% for the diffusion FDM, and 0.6%/1.9% for the SP₃ FDM. In case of the 4G calculations that the spectral error is quite large, on the other hand, the pinwise LFM successfully improved the diffusion and SP₃ SENM results. However, due to the accuracy of the diffusion, the RMS/MAX pin ΔP errors for the diffusion SENM are nearly double of the errors for the SP₃ SENM.

Table 4.8. Results of the 3x3 HZP mini-core calculations

Solver	Grp.	$\Delta\rho$ (pcm)	2D Pin ΔP (%)		1D Axial ΔP (%)	
			RMS	MAX	RMS	MAX
SP1 FDM	4G	-11.7	0.68	2.62	1.03	2.06
	8G	-18.9	0.52	1.25	0.61	1.33
	16G	-18.8	0.47	0.76	0.71	1.40
SP1 SENM	4G	-4.7	0.33	1.68	1.21	2.07
	8G	-12.0	0.35	0.69	0.83	1.74
	16G	-10.8	0.54	1.32	0.75	1.56
SP1 SENM + LFM	4G	0.9	0.50	1.14	0.90	1.87
	8G	-6.4	0.48	0.79	0.83	1.74
	16G	-10.1	0.55	0.88	0.80	1.63
SP3 FDM	4G	-8.6	0.93	3.19	1.04	1.73
	8G	-13.1	0.62	1.90	0.26	0.46
	16G	-13.7	0.48	1.45	0.14	0.38
SP3 SENM	4G	-1.6	0.56	2.05	1.29	2.26
	8G	-6.2	0.12	0.45	0.62	1.16
	16G	-5.7	0.23	0.64	0.45	0.86
SP3 SENM + LFM	4G	5.5	0.23	0.58	0.70	1.34
	8G	-2.0	0.21	0.32	0.39	0.68
	16G	-6.2	0.33	0.54	0.32	0.56

The good agreements of the SP₃ SENM and the solution improvement by the LFM are also shown in **Figure 4.22**. It reveals that the 8G result is already accurate so that the error is nearly unchanged, while the pin ΔP especially noted at the assembly to assembly interface is nearly removed by the LFM for the 4G case.

In addition to the radial pin power, the pinwise LFM also decrease the RMS/MAX axial ΔP errors. In case of the 4G SP₃ SENM calculations, for examples, the errors are decreased from 1.3%/2.3% to 0.7%/1.3%, as shown in **Figure 4.23**. The results presented in the table and figures demonstrate the accuracy of the SP₃ SENM solver and that the 2D base LFM coefficients can be applied for the 3D problem.

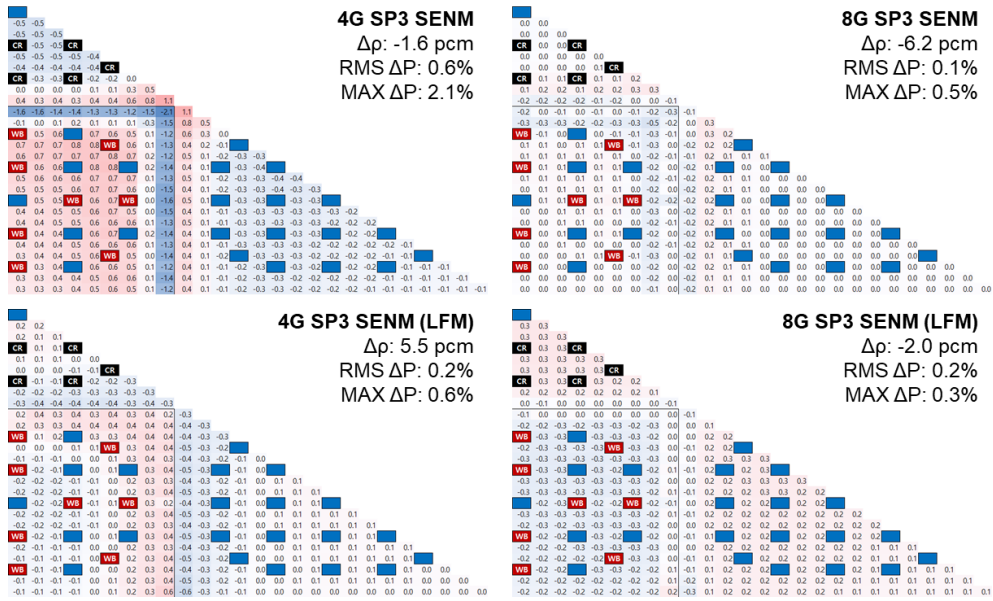


Figure 4.22. Radial pin power error (%) distributions for the 3x3 HZP mini-core obtained by the SP₃ SENM without (top) and with (bottom) the LFM

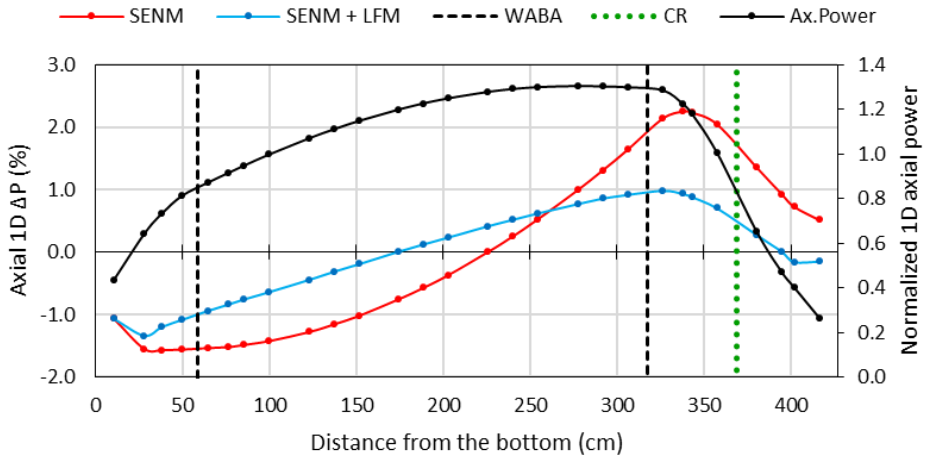


Figure 4.23. Axial 1D power and ΔP (%) distributions obtained from the 3x3 HZP mini-core by the 4G SP₃ SENM without (red) and with (blue) the LFM

The HFP calculations were then performed with the diffusion and SP₃ SENM solvers and the results are summarized in **Table 4.9**. Although the errors are slightly

larger in the HFP case due to the T/H effect, the difference to the HZP is not notable for the radial direction in that the difference of RMS/MAX pin ΔP is merely about 0.1%/0.5%. It is more notable that the RMS/MAX axial ΔP errors are smaller for the HFP than the HZP. In case of the 8G which is also shown in **Figure 4.24**, the errors are 0.6%/1.2% for the HZP and 0.5%/0.8% for the HFP.

Table 4.9. Results of the 3x3 HFP mini-core calculations

Solver	Grp.	$\Delta\rho$ (pcm)	2D Pin ΔP (%)		1D Axial ΔP (%)	
			RMS	MAX	RMS	MAX
SP1 SENM	4G	-8.1	0.40	2.08	0.43	1.13
	8G	-14.6	0.41	1.20	0.57	1.71
	16G	-13.1	0.60	1.48	0.55	1.49
SP3 SENM	4G	-4.7	0.59	2.44	0.47	0.83
	8G	-8.3	0.20	0.72	0.49	0.80
	16G	-7.5	0.31	0.91	0.51	0.81

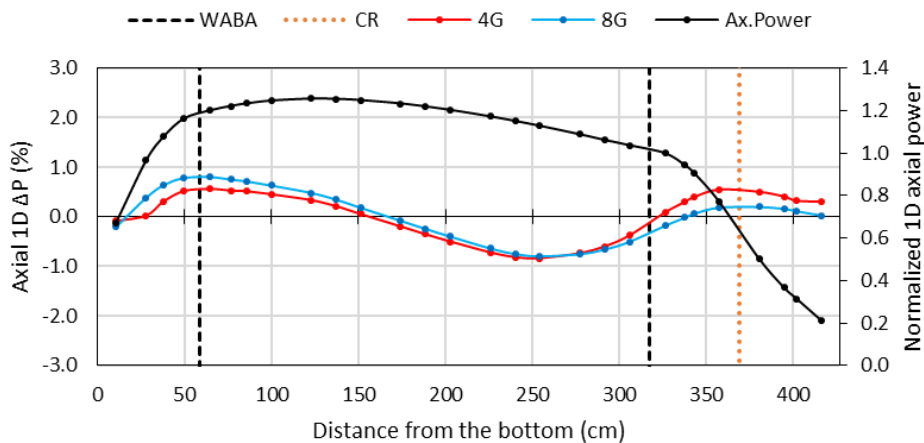


Figure 4.24. Axial 1D power and ΔP (%) distributions obtained from the 3x3 HFP mini-core by the 4G SP₃ SENM without (red) and with (blue) the LFM

For this case, the pinwise LFM was applied and satisfactory results were obtained. **Figure 4.25** shows the example. The $\Delta\rho$ and RMS/MAX pin ΔP errors of the 4G SP₃

SENM are decreased from -9 pcm and 0.6%/2.4% to -4 pcm and 0.3%/0.9%. The results clearly reveal that the pinwise LFM can successfully correct the spectral error even though the T/H effect is involved in the target problem.

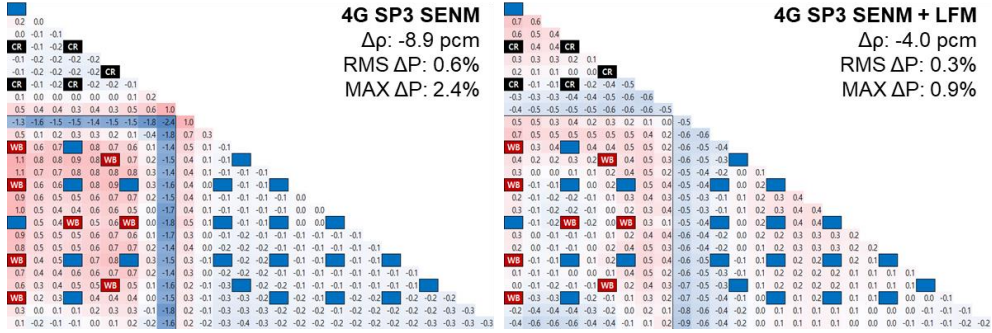


Figure 4.25. Radial pin power error (%) distributions for the 3x3 HZP mini-core obtained by the SP₃ SENM without (left) and with (right) the LFM

4.2.4. Results of the 3D HZP and HFP core calculations

The 3D HZP core calculations were performed to confirm that the results for the full core are consistent with the 3x3 mini-core calculation results. Various rodded configurations were selected as the target for extensive analysis, and it turned out that the dependency of the errors to the solvers and the number of energy groups is highly similar regardless of the core state. As an example, the results for the core with partially inserted AO bank are summarized in **Table 4.10**.

It is noted first that the agreements of the SP₃ SENM is generally good if the number of energy group is sufficient or the pinwise LFM is applied. The RMS/MAX pin $\Delta\rho$ errors are 1.6% for the 4G, 0.5%/1.8% for the 8G, and 0.4%/1.3% for the 16G, and those are decreased to 0.4%/1.3%, 0.3%/0.7% and 0.4%/0.8%, respectively, by the pinwise LFM. The SP₃ FDM results are worse than the SP₃ SENM due to the remarkably large discretization error involved in the FDM.

In contrast, the diffusion solvers are significantly affected by the transport error

so that the use of more accurate PHXSs cannot yield consistent error reduction. For example, the RMS/MAX pin ΔP errors of the diffusion SENM are 1.0%/4.3% for the 4G, 0.6%/1.4% for the 8G, and 0.9%/2.6% for the 16G, and those are changed to 0.7%/1.9%, 0.9%/2.2%, and 1.0%/2.3%, respectively, by the pinwise LFM. The results clearly reveal the need for the accurate solver.

Table 4.10. Results for the AP1000 PWR 3D HZP core with partially inserted AO bank

Solver	Grp.	$\Delta\rho$ (pcm)	2D Pin ΔP (%)		1D Axial ΔP (%)	
			RMS	MAX	RMS	MAX
SP1 FDM	4G	24.8	1.39	5.82	1.27	3.13
	8G	-12.4	0.65	1.69	0.89	1.88
	16G	-20.3	0.64	1.28	1.00	2.23
SP1 SENM	4G	28.3	1.02	4.30	1.12	2.79
	8G	-10.8	0.55	1.38	0.96	2.09
	16G	-16.8	0.86	2.56	0.89	1.77
SP1 SENM + LFM	4G	4.2	0.73	1.85	1.06	2.38
	8G	-12.7	0.91	2.22	1.05	2.07
	16G	-18.6	1.00	2.27	1.04	1.88
SP3 FDM	4G	44.4	2.03	7.64	1.06	2.32
	8G	15.6	1.04	4.14	0.21	0.60
	16G	6.7	0.74	3.04	0.37	0.95
SP3 SENM	4G	46.7	1.62	5.84	0.98	2.10
	8G	16.1	0.53	1.77	0.26	0.79
	16G	9.3	0.39	1.31	0.17	0.45
SP3 SENM + LFM	4G	22.7	0.43	1.27	0.67	1.72
	8G	10.3	0.29	0.70	0.45	0.89
	16G	4.1	0.41	0.84	0.44	0.69

The radial pin ΔP distributions presented in **Figure 4.26** should be also noted. In case of the SP₃ calculations, the pin ΔP is consistently decreased by the use of more elaborated discretization method and accurate PHXSs. In contrast, the pin ΔP is not monotonously decreased but the distributions are changed.

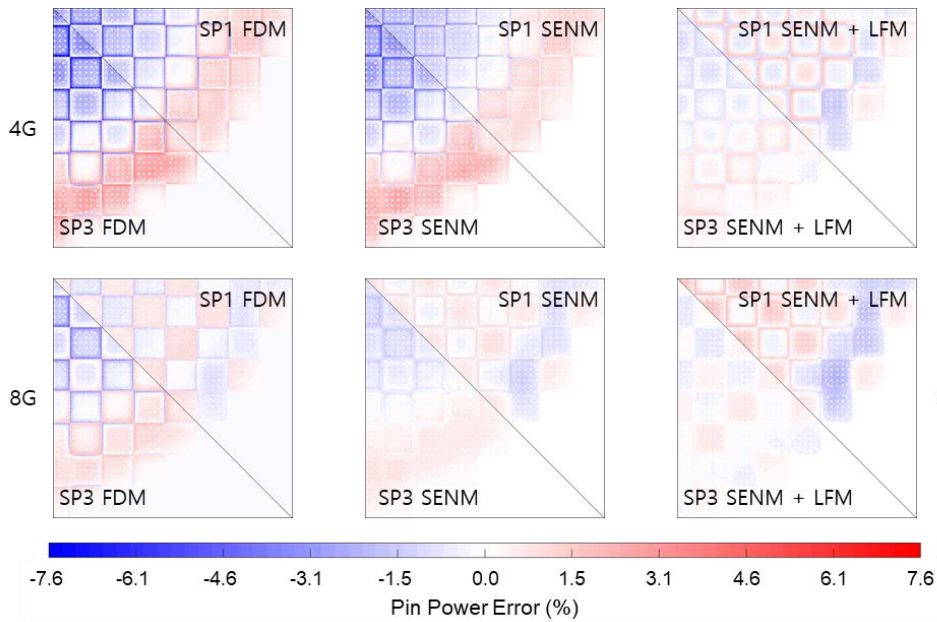


Figure 4.26. Radial pin power error (%) distributions for the AP1000 PWR 3D HZP core with partially inserted AO bank

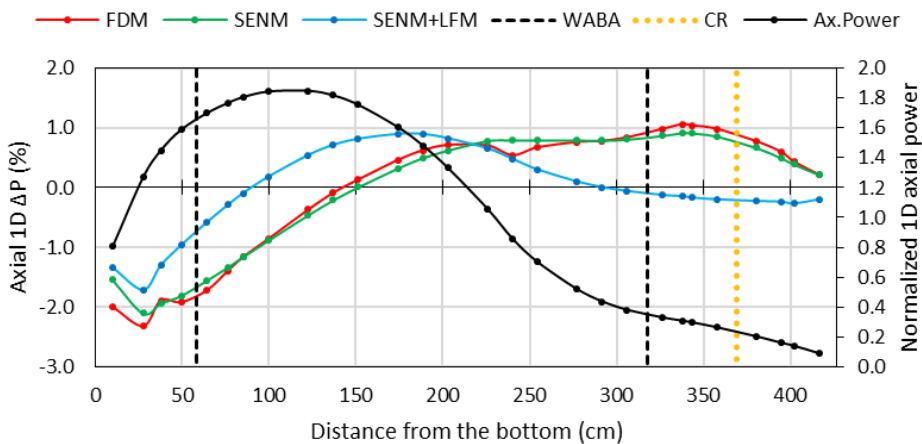


Figure 4.27. Axial 1D power shape and ΔP error (%) distributions obtained by the 4G SP₃ calculations for the AP1000 PWR 3D HZP core with partially inserted AO bank

It is worthwhile to note that the axial ΔP errors are less affected by the solver and the number of energy groups, compared to the radial pin ΔP errors. The results shown in **Figure 4.27** are the example. Even the LFM is applied for the 4G calculation, the

axial ΔP distribution is only shifted to the bottom.

Through the 3D HZP core calculations, it is also revealed that the computing cost for the use of more elaborated solver is not too significant. For this partially rodged core, the computing time yielded by 20 Intel Xeon E5-2630v4 2.20GHz CPU cores is summarized in **Table 4.11**. From the table, it is first noted that the total computing time of the SENM solver is comparable to the FDM due to the coarse mesh finite difference (CMFD) acceleration normally used for the core calculation. Although the computing time is nearly doubled by employing the SP₃ theory and the additional time for the pinwise LFM is quite significant, the results are still comparable to the computing time presented in the previous work by Cho [18]. Furthermore, it should be noted that a previous study with VANGARD yielded more than 20 times speedup of the SP₃ SENM calculation by the acceleration with a consumer grade GPU [26], due to inherent parallelism of the nodal kernel. Considering that the computing performance of the GPU is being rapidly improved in these days, the computing time will not render a problem for the use of the SP₃ SENM solver in the follow-up study which will fully employ the GPU acceleration capability.

Table 4.11. Computing time (sec) comparisons for the AP1000 PWR 3D HZP core with partially inserted AO bank

Solver	4G	8G	16G
SP1 FDM	25.2	66.0	133.6
SP1 SENM	30.8	63.9	173.2
SP3 FDM	50.2	150.1	457.7
SP3 SENM	56.8	120.3	307.5
SP3 SENM + LFM	130.5	158.7	402.6

Following the calculations for the cores with the fixed T/H condition, the branch conditions were then involved. The isothermal temperature coefficient (ITC) and the boron worth (BW) were determined as the partial derivatives of the reactivity to the temperature variation from 555K to 575K and the boron concentration change from

1271 ppm to 1321 ppm, respectively. **Table 4.12** presents the results. *Diffusion*, *SP3*, and *SP3 + LFM* indicate that the results were obtained by the diffusion and SP₃ SENM calculations and the pinwise LFM was applied with the SP₃ SENM. Note that the pinwise LFM is not applied for the 16G due to the marginal difference observed from the HZP core calculations. The results are satisfactory regardless of the energy groups and solvers since ITC and BW indicate the rate of change.

In this regard, the critical boron concentration (CBC) at the HZP and HFP states presented in **Table 4.13** is more meaningful. From the table, it is clearly noted that the SP₃ SENM solver yielded good results for the core without and with the T/H feedback if the number of energy groups is sufficient or the LFM is applied.

Table 4.12. ITC and boron worth (BW) of the AP1000 PWR 3D HZP ARO core

Case		Diffusion			SP3			SP3 + LFM	
		4G	8G	16G	4G	8G	16G	4G	8G
ITC	$\Delta\text{pcm/K}$	0.1	0.1	0.1	-0.1	-0.2	-0.2	0.1	0.0
	Error (%)	-2.4	-2.9	-2.8	3.1	5.1	5.1	-2.9	1.0
BW	ΔWorth	0.0	0.0	0.0	0.0	0.0	0.0	0.0	0.0
	Error (%)	-0.1	0.1	0.1	-0.3	-0.1	-0.1	-0.1	0.1

Table 4.13. Critical boron concentration of the AP1000 PWR 3D ARO core

State		Diffusion			SP3			SP3 + LFM	
		4G	8G	16G	4G	8G	16G	4G	8G
HZP	Δppm	2.3	-3.2	-3.9	5.4	1.1	0.3	1.4	-0.7
	Error (%)	0.2	-0.2	-0.3	0.4	0.1	0.0	0.1	-0.1
HFP	Δppm	5.6	0.7	0.0	7.9	4.0	3.2	4.3	2.7
	Error (%)	0.5	0.1	0.0	0.7	0.3	0.3	0.4	0.2

Finally, the 3D HFP core calculations were performed. The results of the diffusion and SP₃ SENM calculations without and with the LFM for the core with partially

inserted AO bank are summarized in **Table 4.14**. The radial pin ΔP distributions are presented in **Figure 4.28** and the axial ΔP of the 4G SP₃ SENM calculations are shown in **Figure 4.29**. Compared to the HZP counterparts, the errors are slightly increased by the T/H effect. For example, the RMS/MAX pin ΔP errors of the 16G SP₃ SENM are 0.4%/1.3% for the HZP and 0.5%/1.9% for the HFP. However, the observations from the HZP calculations are still valid. In case of the SP₃ SENM, the RMS/MAX pin ΔP errors are 1.4%/5.4% for the 4G and 0.6%/2.2% for the 8G, and those are decreased to 0.5%/1.8% and 0.4%/1.4% by the LFM. On the other hand, in case of the diffusion SENM, the errors are rather increased from 0.6%/1.5% to 0.8%/2.1% by applying the LFM for the 8G.

In conclusion, validity of the core calculation strategy employing the accurate solver and the pinwise LFM is successfully demonstrated for the initial core. The agreement of the SP₃ SENM calculation is generally good and the LFM coefficient set based on the 2D 2x2 CBs at the base condition effectively reduces the spectral error even for the highly heterogeneous 3D HFP cores.

Table 4.14. Results for the AP1000 PWR 3D HFP core with partially inserted AO bank

Solver	Grp.	Δp	2D Pin ΔP (%)		1D Axial ΔP (%)	
		(pcm)	RMS	MAX	RMS	MAX
SP1 SENM	4G	33.0	0.94	4.31	0.76	1.90
	8G	-8.7	0.57	1.54	0.86	2.00
	16G	-16.2	0.81	2.19	0.76	1.80
SP1 SENM + LFM	4G	1.8	0.76	1.95	0.83	2.13
	8G	-14.1	0.81	2.14	0.95	2.23
SP3 SENM	4G	51.3	1.38	5.43	0.55	1.20
	8G	17.9	0.59	2.15	0.53	1.00
	16G	9.6	0.53	1.88	0.43	0.76
SP3 SENM + LFM	4G	21.3	0.54	1.80	0.62	1.57
	8G	9.6	0.43	1.44	0.61	1.27

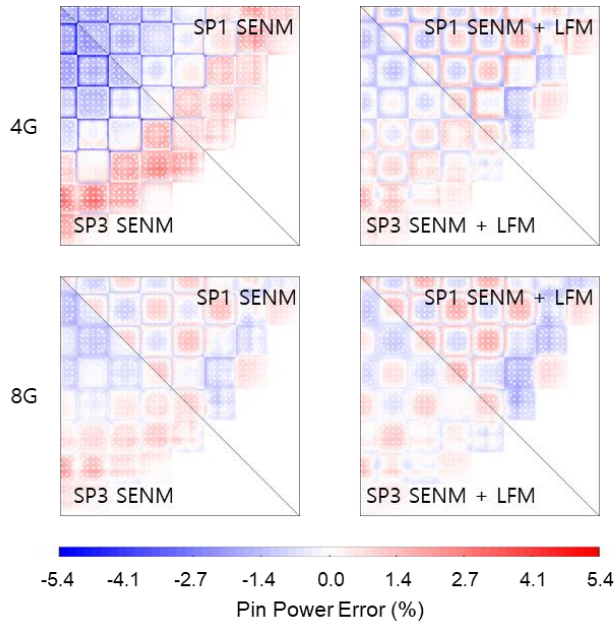


Figure 4.28. Radial pin power error (%) distributions for the AP1000 PWR 3D HFP rodded core with partially inserted AO bank

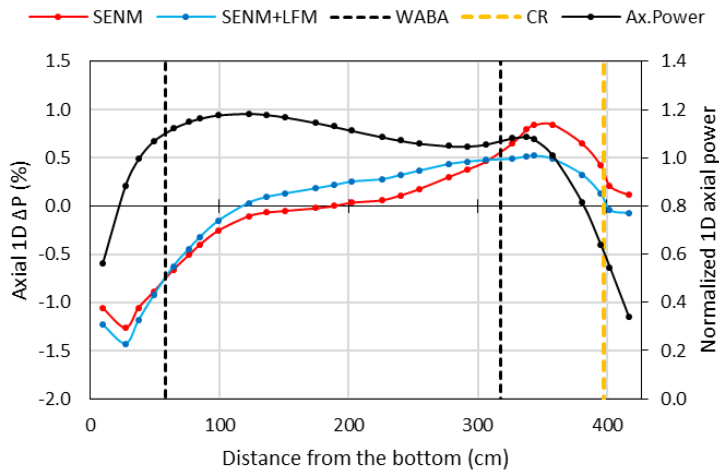


Figure 4.29. Axial 1D power shape and ΔP error (%) distributions obtained by the 4G SP_3 calculations for the AP1000 PWR 3D HFP core with partially inserted AO bank

4.2.5. Results of the 3D HFP core depletions

The Cycle 1 core depletion calculations were performed for the 3D HFP ARO core with the CBC search. The SP₃ SENM solver was employed to assess the accuracy of the solver in the depletion, as well as the pinwise LFM was applied for the 4 and 8G to confirm the applicability of the method for the operating core conditions. The CBC curve and the errors are presented in **Figure 4.30**, and the MAX pin and axial ΔP error changes to the burnup are shown in **Figure 4.31** and **Figure 4.32**. The 4G results without and with the LFM and the 16G result are given in **Table 4.15**.

The results reveal the good agreements of the SP₃ SENM for the core depletion and the solution improvement by the pinwise LFM. It is worthwhile to note that the 4G result with the LFM is even comparable to the 16G result. For example, the boron concentration error and the RMS/MAX pin ΔP errors at the beginning of the cycle (BOC) are 6.3 ppm and 1.3%/5.1% for the 4G and 1.6 ppm and 0.5%/1.9% for the 16G, but the notable errors for the 4G are decreased to -2.9 ppm and 0.4%/1.6% by the LFM and those are maintained during the depletion.

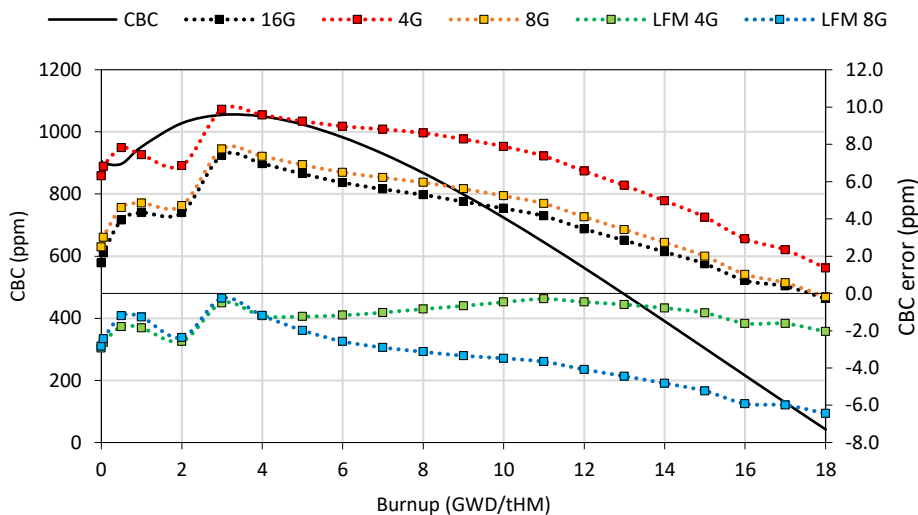


Figure 4.30. The CBC curve and the errors (ppm) for the AP1000 PWR 3D HFP ARO core depletions obtained with the SP₃ SENM solver

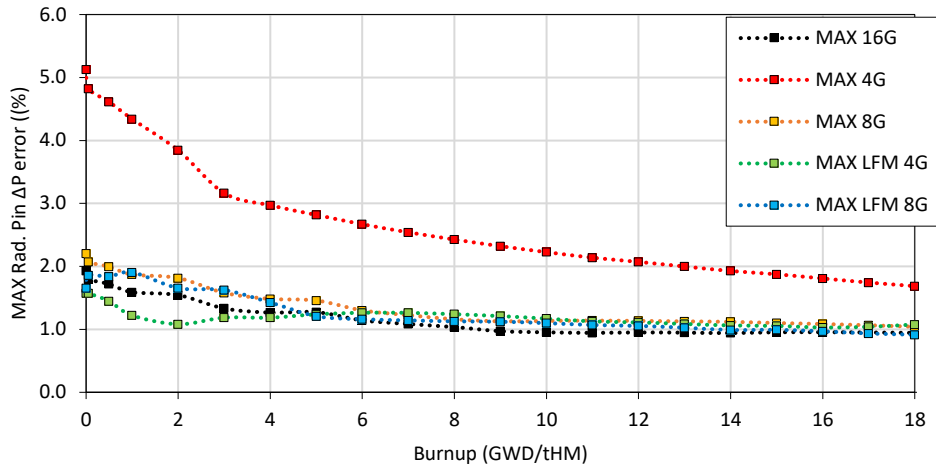


Figure 4.31. The MAX pin ΔP errors (%) for the AP1000 PWR 3D HFP ARO core depletions obtained with the SP₃ SENM solver

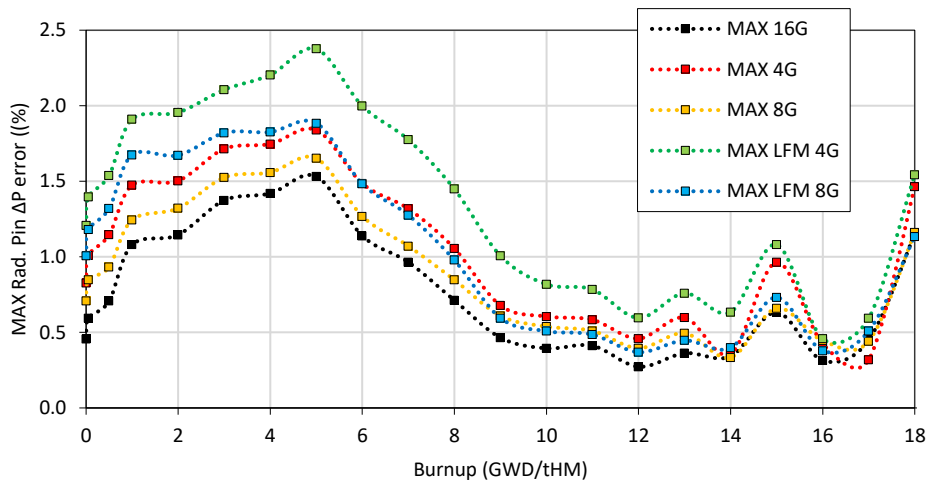


Figure 4.32. The MAX axial ΔP errors (%) for the AP1000 PWR 3D HFP ARO core depletions obtained with the SP₃ SENM solver

Although the MAX axial ΔP is increased by the LFM, but the magnitude is smaller than that of the pin ΔP . Therefore, it can be concluded that the applicability of the pinwise LFM to the operating core is successfully demonstrated.

Table 4.15. Results of the AP1000 PWR 3D HFPARO core depletions obtained with the SP₃ SENM solver

GWD /tHM	CBC, ppm	16G						4G						4G + LFM			
		Δ ppm	2D Pin Δ P (%)		1D Axial Δ P (%)		Δ ppm	2D Pin Δ P (%)		1D Axial Δ P (%)		Δ ppm	2D Pin Δ P (%)		1D Axial Δ P (%)		
			RMS	MAX	RMS	MAX		RMS	MAX	RMS	MAX		RMS	MAX	RMS	MAX	
0	905.2	1.6	0.51	1.93	0.36	0.83	6.3	1.32	5.13	0.36	0.83	-2.9	0.43	1.57	0.66	1.21	
0.05	896.4	2.2	0.46	1.80	0.42	1.01	6.8	1.24	4.82	0.42	1.01	-2.6	0.43	1.57	0.68	1.40	
0.5	893.3	3.9	0.43	1.72	0.48	1.15	7.8	1.16	4.61	0.48	1.15	-1.8	0.39	1.45	0.69	1.54	
1	947.7	4.3	0.39	1.59	0.65	1.47	7.4	1.08	4.34	0.65	1.47	-1.9	0.37	1.22	0.84	1.91	
2	1023.5	4.3	0.35	1.54	0.70	1.50	6.9	0.95	3.84	0.70	1.50	-2.6	0.34	1.08	0.89	1.96	
3	1047.4	7.4	0.29	1.33	0.81	1.71	9.9	0.77	3.16	0.81	1.71	-0.5	0.37	1.19	1.00	2.11	
4	1043.0	7.0	0.26	1.27	0.85	1.75	9.6	0.68	2.97	0.85	1.75	-1.2	0.37	1.19	1.10	2.20	
5	1017.4	6.4	0.25	1.27	0.94	1.84	9.2	0.63	2.82	0.94	1.84	-1.2	0.37	1.24	1.24	2.38	
6	976.5	5.9	0.23	1.14	0.67	1.48	9.0	0.58	2.67	0.67	1.48	-1.2	0.39	1.26	0.93	2.00	
7	924.1	5.6	0.22	1.08	0.58	1.32	8.8	0.56	2.54	0.58	1.32	-1.0	0.39	1.26	0.78	1.77	
8	862.5	5.3	0.22	1.04	0.42	1.06	8.6	0.55	2.43	0.42	1.06	-0.8	0.39	1.24	0.57	1.45	
9	793.8	4.9	0.22	0.97	0.25	0.68	8.3	0.54	2.32	0.25	0.68	-0.7	0.39	1.21	0.35	1.01	
10	719.4	4.6	0.23	0.95	0.22	0.60	7.9	0.54	2.23	0.22	0.60	-0.5	0.38	1.17	0.27	0.82	
11	640.6	4.2	0.23	0.94	0.23	0.58	7.4	0.53	2.14	0.23	0.58	-0.3	0.37	1.13	0.26	0.78	
12	558.7	3.5	0.23	0.95	0.17	0.46	6.6	0.52	2.07	0.17	0.46	-0.5	0.37	1.11	0.22	0.60	
13	474.3	2.8	0.24	0.95	0.28	0.60	5.8	0.51	2.00	0.28	0.60	-0.6	0.36	1.09	0.28	0.76	
14	388.3	2.2	0.24	0.94	0.13	0.36	5.0	0.50	1.93	0.13	0.36	-0.8	0.35	1.06	0.23	0.63	
15	301.6	1.6	0.24	0.95	0.55	0.96	4.1	0.49	1.87	0.55	0.96	-1.0	0.35	1.05	0.50	1.08	
16	214.9	0.7	0.24	0.95	0.25	0.43	2.9	0.48	1.81	0.25	0.43	-1.6	0.34	1.03	0.24	0.46	
17	128.1	0.4	0.24	0.95	0.15	0.32	2.3	0.47	1.74	0.15	0.32	-1.6	0.34	1.04	0.25	0.59	
18	42.5	-0.3	0.24	0.94	0.85	1.46	1.4	0.46	1.69	0.85	1.46	-2.0	0.34	1.08	0.80	1.54	

4.3. APR1400 PWR Initial Core

The Advanced Power Reactor (APR) 1400 PWR initial core designed to yield about 4000 MWth power has 241 FAs loaded in 17x17 core array. The FAs having 16x16 lattice feature with 236 fuel rods and 5 GTs are categorized into three types, A, B and C, by enrichment of the fuel. The fuel rods except for the lowest one have lower enriched top and bottom axial blanket. The B and C type FAs are subdivided by loading pattern of the fuel rods and the number of Gd pins. Those also have enrichment zoning which is formed by placing lower enriched fuel pins near the guide tubes and inter-assembly water gap between the neighboring assemblies. The core loading pattern and control element assembly (CEA) maps are presented in **Figure 4.33** with the specification of C3 FA.

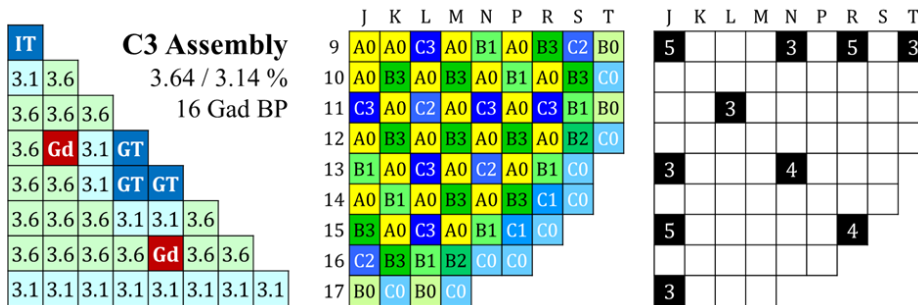


Figure 4.33. C3 FA (left) and core loading pattern (center) and the control element assembly (CEA) map (right) of the APR1400 PWR initial core

The goal of the APR1400 PWR initial core calculations aims to confirm that the observations from the previous chapters are valid for another large reactor core. For a beginning, significance of the spectral error was estimated and the results are shown in **Figure 4.34**. In that the core is less heterogeneous than KAIST 1A and AP1000, the effect of the spectral error to the pin power is notably smaller and it is remarkably decreased as more energy groups are used. From the figure, it should be noted that the MAX pin ΔP error for the 8G, 1.5% for the total error and 1.8% for the boundary spectral error, appear at the core outermost pin-cells. If the outermost

pin-cells with low power are not included, the errors drop to 0.6%. Therefore, it can be estimated that the core calculation results employing the 8 or more energy group would be marginally changed by the pinwise LFM.

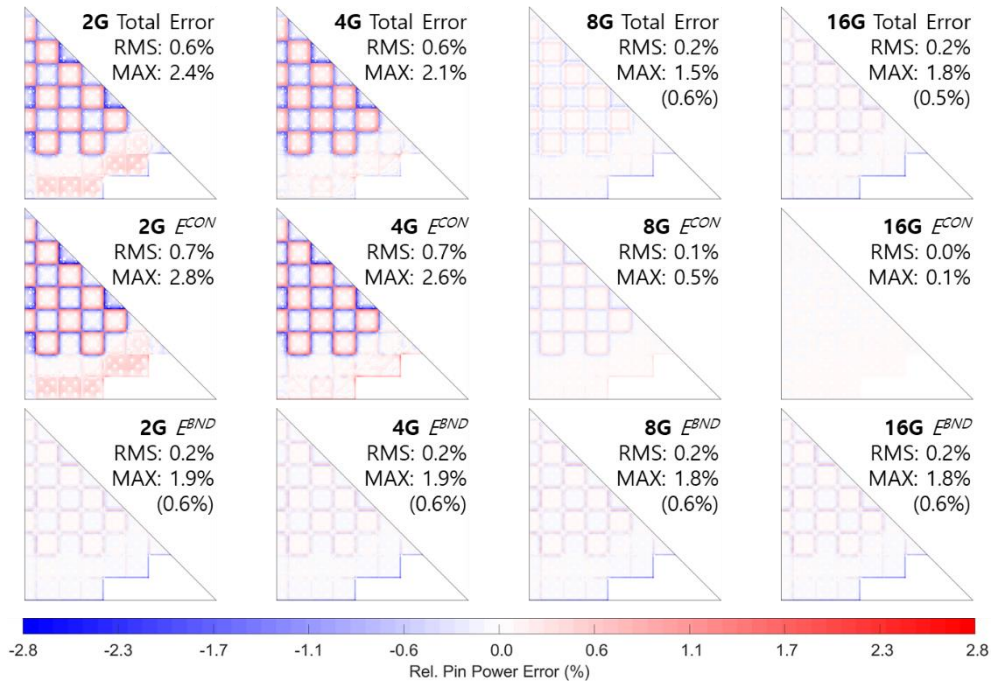


Figure 4.34. Relative pin power error (%) distributions for the APR1400 PWR 2D HZP core due to the total spectral error (top), group condensation error (middle), and boundary spectral error (bottom)

The 3D HZP ARO core calculations were performed the first for the core with the diffusion and SP₃ SENM solvers. The results are summarized in **Table 4.16**, and the pin ΔP distributions obtained by the 4G calculations are presented in **Figure 4.35**. The diffusion results are denoted as SP1 for convenience. From the table, it is first noted that the agreements of the SP₃ SENM are better than the diffusion for the 8 and 16G and the 8G results are somewhat similar with the 16G in that the spectral error is sufficiently small with the 8G as noted in **Figure 4.34**. It is also noted that the notably large RMS/MAX pin ΔP errors are successfully reduced by the pinwise LFM. In case of the SP₃, for example, the errors are decreased from 1.7%/3.6% to

0.4%/1.3%. For the 8G SP₃ SENM, on the other hand, the RMS/MAX pin ΔP are merely changed from 0.5%/1.7% to 0.4%/1.6%. Since the 3D HZP ARO core results are consistent with the AP1000 counterpart, the branch conditions are introduced.

Table 4.16. Results for the APR1400 PWR 3D HZP ARO core

Solver	#.G	$\Delta\rho$ (pcm)	2D Pin ΔP (%)		1D Plane ΔP (%)	
			RMS	MAX	RMS	MAX
SP1 SENM	4G	-0.6	1.06	2.33	0.28	0.54
	8G	6.3	0.85	2.59	0.15	0.29
	16G	6.0	1.09	3.21	0.15	0.27
SP1 SENM + LFM	4G	-11.2	0.90	2.79	0.28	0.54
	8G	-9.9	1.07	3.17	0.19	0.41
SP3 SENM	4G	2.3	1.65	3.57	0.24	0.50
	8G	9.9	0.52	1.67	0.08	0.20
	16G	9.0	0.52	2.20	0.08	0.18
SP3 SENM + LFM	4G	-7.2	0.40	1.28	0.23	0.49
	8G	-4.9	0.37	1.60	0.12	0.31

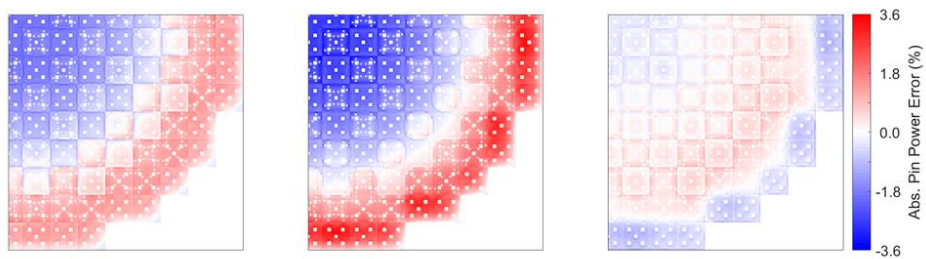


Figure 4.35. Radial pin power error (%) distributions for the APR1400 PWR 3D HZP ARO core obtained by the 4G diffusion (left) and SP₃ (center) SENM and SP₃ SENM + LFM (right) calculations

The ITC and BW presented in **Table 4.17** are determined as the partial derivatives of the reactivity to the core temperature variation from 565K to 585K and the boron concentration change from 1165 ppm to 1215 ppm. The calculations were performed with the diffusion and SP₃ SENM solvers denoted by *SP1* and *SP3*, and the LFM

was additionally applied with the SP₃ SENM. The table shows that the agreements of the solvers are generally good and the pinwise LFM functions well with the branch conditions. The CBC calculation results at the HZP and HFP states, which are given in **Table 4.18**, are also satisfactory and consistent with the AP1000 results.

Table 4.17. ITC and boron worth (BW) of the APR1400 PWR 3D HZP core

Case		SP1			SP3			SP3 + LFM	
		4G	8G	16G	4G	8G	16G	4G	8G
ITC	$\Delta\text{pcm/K}$	0.3	0.4	0.4	0.1	0.2	0.1	0.6	0.2
-12.4	Error (%)	-2.4	-3.6	-3.3	-0.9	-1.4	-1.1	-4.5	-2.0
BW	ΔWorth	0.0	0.0	0.0	0.0	0.0	0.0	0.0	0.0
-11.0	Error (%)	-0.2	0.1	0.1	-0.3	-0.1	0.0	0.1	0.1

Table 4.18. Critical boron concentration of the APR1400 PWR 3D core

State		SP1			SP3			SP3 + LFM	
		4G	8G	16G	4G	8G	16G	4G	8G
HZP	Δppm	0.8	0.3	0.1	1.5	1.3	1.0	-0.8	-0.9
1189.7	Error (%)	0.1	0.0	0.0	0.1	0.1	0.1	-0.1	-0.1
HFP	Δppm	3.6	4.4	4.2	3.7	4.6	4.3	4.4	4.5
1090.8	Error (%)	0.3	0.4	0.4	0.3	0.4	0.4	0.4	0.4

Lastly, the 3D HFP ARO core calculations were performed. The results are given in **Table 4.19**, and the pin ΔP distributions for the 4G calculations are presented in **Figure 4.36**. From the table and figure, it is clearly noted that the results consistent with the HZP counterparts are obtained, although the magnitude is slightly increased by the T/H effect. Furthermore, the LFM coefficient set based on the 2C 2x2 CB at the base condition succeed to correct the spectral error for the operating 3D core.

Table 4.19. Results for the APR1400 PWR 3D HFP ARO core

Solver	Grp.	$\Delta\rho$ (pcm)	2D Pin ΔP (%)		1D Plane ΔP (%)	
			RMS	MAX	RMS	MAX
SP1 SENM	4G	35.5	0.82	2.01	0.48	0.95
	8G	48.8	0.77	2.62	0.55	0.93
	16G	46.2	0.95	3.20	0.55	0.93
SP1 SENM + LFM	4G	59.3	0.80	2.25	0.74	1.35
	8G	39.7	0.86	2.36	0.67	1.15
SP3 SENM	4G	35.4	1.15	2.83	0.40	0.77
	8G	49.0	0.53	1.73	0.34	0.57
	16G	46.0	0.60	2.28	0.34	0.57
SP3 SENM + LFM	4G	58.2	0.45	1.52	0.62	1.18
	8G	41.6	0.43	1.80	0.47	0.85

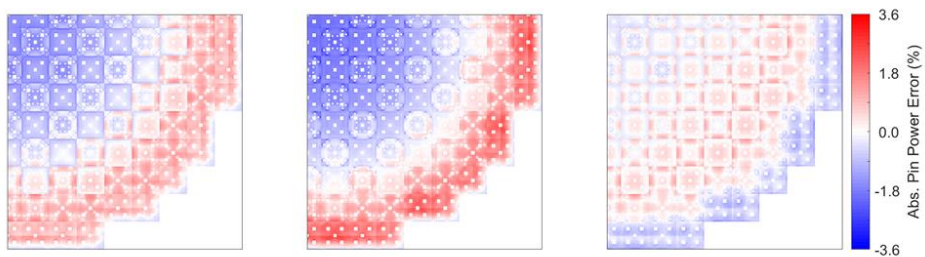


Figure 4.36. Radial pin power error (%) distributions for the APR1400 PWR 3D HFP ARO core obtained by the 4G diffusion (left) and SP₃ (center) SENM and SP₃ SENM + LFM (right) calculations

Based on the APR1400 PWR core calculation results in addition to the other results presented in this chapter, it can be finally concluded that the high-fidelity pinwise TSCC strategy is successfully demonstrated.

Chapter 5. Summary and Conclusions

For the high-fidelity TSCC, the optimal solution method is selected through the systematic error analysis and the pinwise LFM is developed. Based on the general TSCC procedure, it is identified first in this work that the spatial homogenization error, group condensation error, transport error, and discretization error are the major error sources involved in PHMGC that are corrected by the SPH factors. Since the SPH factors simultaneously correct the transport and discretization errors, even a very low order solution method such as a CM diffusion FDM solver can yield acceptable core calculation results. It is beneficial for the practicality, however, correction of the two errors which are sensitive to the core environment using a single set of the SPH factors is not desirable. If the core environment deviates more from the reference condition where the SPH factors are obtained, the errors would increase. In this regard, a proper lower order solver which can minimize the degree correction for the two error sources as much as practically possible is defined as the optimal solution method. It is estimated that the inconsistency of the SA based SPH factors in the core can be mitigated by using the optimal solver.

For selection of the solver, the errors determined by the transport approximations including the diffusion, SP_N , and S_N are investigated, and the effect of the sub pin-cell mesh size is observed. Various core benchmark problems are employed for the analysis. The observations to be noted are as follows. First of all, the diffusion calculations involve severe transport error, but it is effectively reduced by the SP_3 . However, compared to the difference between the diffusion and the SP_3 calculation results, the solution improvement by the SP_5 calculation is marginal. In case of the 8G KAIST 1A ARO core calculation without the SPH factor, for example, the SP_5 shows only about 20 pcm of the $\Delta\rho$ and within 0.1% of the RMS pin ΔP differences to the SP_3 . Therefore, it determined that the used of the higher order SP_N method is inappropriate. Secondly, the discretization error is significant even in a case that the pin pitch is only 1.26cm. For the same ARO core, more than 8x8 meshes per pin are required for the SP_N FDM calculation to reduce the MAX pin ΔP within 1%. Since

the core calculation using very fine mesh is not practical, employment of the SENM solver is determined. The accuracy of SENM taking a pin-cell as a mesh is close to the 8x8 FDM in that the hyperbolic functions and Legendre polynomials are adopted as the basis functions. Thirdly, the diffusion and SP_N calculations involve notable error cancellation between the transport and discretization errors. It is the reason that the coarse mesh diffusion FDM solver can yield seemingly good results. Thus, the two errors should be simultaneously corrected for the accurate core calculation. Lastly, the S_N method is inappropriate for PHMGC with the SPH factors. In contrast to the SP_N calculations that the SPH factors in the thermal energy range have large effect on the results, the SPH factors in the fast energy range significantly affect the S_N calculation results. Because the pinwise distribution of the fast range SPH factors for the S_N solver is sensitive to the assembly BC, it is hard to obtain the proper SPH factors using the SA configurations.

Based on the analysis, the SP_3 SENM solver is selected as the optimal. For the 8G KAIST 1A ARO core calculation, the RMS and MAX pin ΔP errors due to the SA based SPH factor are only 0.2% and 1.1% with the SP_3 SENM solver. It is far smaller than 0.7% and 4.6% of the diffusion FDM and 1.1% and 8.5% of the SP_3 FDM. Note that each pin-cell is taken as a mesh. Following that, it is shown that the SP_3 SENM solver does not render excessive computing cost through the 3D commercial PWR core calculations. For the AP1000 PWR HZP core with partially inserted CRs, for example, the computing time of the 8G calculations with 20 CPU cores is 66 seconds (s) with the coarse mesh diffusion FDM and 120 s with the SP_3 SENM. The results show that the additional computing cost for the accurate solution method is not too excessive. For the computing time, in addition, it should be noted that a previous study with VANGARD yielded more than 20 times speedup of the SP_3 SENM calculation by the acceleration with a consumer grade GPU. It is because of the inherent parallelism of the nodal kernel.

The error analysis rendered the need for a leakage correction as well. In the core calculation, the leakage at each assembly boundary exists due to neighboring nodes. However, the MG PHXSs are normally obtained from SA configurations with all

reflective BC so that the PHXSs cannot involve the leakage effect. Furthermore, the group condensation error within assembly is corrected by the SA based SPH factors but the error at the assembly boundaries is not. It is the reason that the spectral error appear in the core calculation results. For typical reactor cores such as the APR1400 PWR, the effect of the spectral error is relatively small, and it is rapidly decreased as more energy groups are used. For heterogeneous core problems such as the AP1000 PWR and the KAIST 1A benchmark, in contrast, the MAX relative pin $\Delta\rho$ due to the spectral error is about 2.0% and 4.8% even with the 8G.

For this reason, development of the pinwise LFM for the correction of MG PHXSs is determined. Since the spectral error is proportional to the leakage, the PHXSs are functionalized to the 3G LTRRs representing the fast, intermediate, and thermal energy ranges. The 3G LTRRs are independent to the actual number of energy groups used for the core calculation in that the groupwise LTRRs can be functionalized to the 3G LTRRs. Validation of the pinwise LFM is performed first for the HZP core calculations and the results are satisfactory. For the 8G KAIST 1A ARO core calculation, for example, about 74 pcm of the $\Delta\rho$ and 7.3% of the MAX pin $\Delta\rho$ are obtained with the SP₃ SENM only, but the errors are dropped to 9 pcm and 1.1% by the LFM. Motivated by this, the range of application is extended to various core states employing the following two approaches. For the HFP calculations, deviation of the PHXSs due to T/H, leakage, and their cross effect are systematically analyzed to confirm that the cross effect is smaller than the others, and then the use of the LFM coefficients obtained from the base condition is determined. For the depletion, the coefficients are tabulated to the burnup exposure likewise the MG PHXSs. The approaches are validated by the HFP core calculations for AP1000 and APR1400 and the cycle 1 depletions for AP1000. The results successfully reveal the applicability of the pinwise LFM for the practical core calculations. Although the computing time is about 30% increase by the LFM iteration, the cost is not too demanding, and it will be reduced by the GPU acceleration in follow-up studies.

In this work, the high-fidelity TSCC is facilitated by employing the SP₃ SENM solver as the optimal lower order solution method and the pinwise LFM as a leakage

correction method. Because the inconsistency of the SA based SPH factor is reduced by the SP_3 SENM solver and the spectral error of the MG PHXS is corrected by the pinwise LFM, the heterogeneous reference solution can be accurately reproduced. It is the value of the work. The PHMGC results based on the strategy are less affected by the error cancellation, therefore, the accurate results can be obtained regardless of the difficulty of the problems. In addition, the study becomes a cornerstone of the VANGARD development to make the code capable for the high-fidelity pinwise TSCC. Recently, advanced core design and enforced safety regulations increase the need for accurate core calculation. In this regard, it is expected that the systematic error analysis and the approach to the leakage correction method can also provide a guideline for potential users and developers of the advanced TSCC codes.

References

- [1] J. Rhodes, K. Smith and D. Lee, "CASMO-5 Development and Applications," in *Proceedings of PHYSOR2006*, Vancouver, BC, Canada, 2006.
- [2] T. Bahadir, S.-O. Lindahl and S. P. Palmtag, "SIMULATE-4 Multigroup Nodal Code with Microscopic Depletion Model," in *Proceedings of M&C2005*, Palais des Papes, Avignon, France, 2005.
- [3] T. Bahadir and S. Lindahl, "Studsvik's Next Generation Nodal Code SIMULATE-5," in *Advances in Nuclear Fuel Management IV (ANFM 2009)*, Hilton Head Island, South Carolina, USA, 2009.
- [4] H. G. Joo, J. Y. Cho, K. S. Kim, C. C. Lee and S. Q. Zee, "Methods and Performance of a Three-Dimensional Whole-Core Transport Code DeCART," in *Proceedings of PHYSOR2004*, Chicago, Illinois, USA, 2004.
- [5] B. O. Cho, H. G. Joo, J. Y. Cho, J. S. Song and S. Q. Zee, "MASTER-3.0: Multi-purpose Analyzer for Static and Transient Effects of Reactors," KAERI/TR-2061, Korea, 2002.
- [6] Y. S. Jung, C. B. Shim, C. H. Lim and H. G. Joo, "Practical numerical reactor employing direct whole core neutron transport and subchannel thermal/hydraulic solvers," *Annals of Nuclear Energy*, vol. 62, pp. 357-374, 2013.
- [7] J. H. Jeong, "Establishment of nTRACER-RENU S Linkage System and Nuclear Core Design for Submarine Application," Master Thesis, Seoul National University, 2018.
- [8] J. I. Yoon, C. H. Lim, H. S. Hong and H. H. Cho, "Development of the High-Performance Pin-by-Pin Calculation Code with Planar Parallelization," in *Transactions of ANS*, Orlando, Florida, USA, 2018.
- [9] M. Tatsumi and A. Yamamoto, "Advanced PWR Core Calculation Based on Multi-group Nodal-transport Method in Three-dimensional Pin-by-Pin Geometry," *Journal of Nuclear Science and Technology*, vol. 40, no. 6, pp. 376-387, 2003.
- [10] U. Rohde, S. Kliem, U. Grundmann, S. Baier, Y. Bilodid, S. Duerigen, E. Fridman, A. Gommlich, A. Grahn, L. Holt, Y. Kozmenkov and S. Mittag, "The reactor dynamics code DYN3D – models, validation and applications," *Progress in Nuclear Energy*, vol. 89, pp. 170-190, 2016.
- [11] Y. Li, W. Yang, H. Wu and L. Cao, "A three-dimensional PWR-core pin-by-pin analysis code NECP-Bamboo2.0," *Annals of Nuclear Energy*, vol. 144, 2020.
- [12] C. H. Lee and T. J. Downar, "A Hybrid Nodal Diffusion/SP3 Method Using One-Node Coarse-Mesh Finite Difference Formulation," *Nuclear Science and Engineering*, vol. 146, pp. 176-187, 2004.
- [13] T. Kozlowski, Y. Xu, T. J. Downar and D. Lee, "Cell Homogenization Method for Pin-by-Pin Neutron Transport Calculations," *Nuclear Science and Engineering*, vol. 169, pp. 1-18, 2011.
- [14] A. Yamamoto, T. Sakamoto and T. Endo, "Discontinuity Factors for Simplified P3 Theory," *Nuclear Science and Engineering*, vol. 183, pp. 39-51, 2016.

- [15] A. Hébert, "A Consistent Technique for the Pin-by-Pin Homogenization of a Pressurized Water Reactor Assembly," *Nuclear Science and Engineering*, vol. 113, pp. 227-238, 1993.
- [16] A. Yamamoto, M. Tatsumi, Y. Kitamura and Y. Yamane, "Improvement of the SPH Method for Pin-by-Pin Core Calculations," *Journal of Nuclear Science and Technology*, vol. 41, no. 12, pp. 1155-1165, 2004.
- [17] J. Yoon, H. C. Lee, H. G. Joo and H. S. Kim, "High performance 3D pin-by-pin neutron diffusion calculation based on 2D/1D decoupling method for accurate pin power estimation," *Nuclear Engineering and Technology*, 2021.
- [18] H. H. Cho, "Development of Pinwise SP3 Based Fast Core Transient Analysis Methodology and the SPHINCS Code," PhD Thesis, Seoul National University, 2021.
- [19] H. Hong and H. G. Joo, "Source Expansion Nodal Kernel for Multi-Group Pin-by-Pin SP3 Core Calculation," in *KNS 2020 Spring*, Jeju, Korea, 2020.
- [20] H. Hong and H. G. Joo, "Leakage Feedback Method for Spectral Correction in Pin-Homogenized Multi-Group Core Calculations," in *Proceedings of M&C 2019*, Portland, Oregon, USA, 2019.
- [21] "Benchmark on Deterministic Transport Calculations Without Spatial Homogenization (MOX Fuel Assembly 3-D Extension Case)," NEA/NSC/DOC(2005)16, OECD NEA, 2005.
- [22] H. Z. Cho, "Benchmark Problem 1A," KAIST/NurapT, 2000. [Online]. Available: <https://nurapt.kaist.ac.kr/benchmark>.
- [23] F. Franceschini, A. Godfrey, J. Kulesza and R. Oelrich, "Westinghouse VERA Test Stand – Zero Power Physics Test Simulations for the AP1000® PWR," CASL-U-2014-0012-000, Consortium for Advanced Simulation of LWRs, Rev. 1, 2014.
- [24] "APR1400 DESIGN CONTROL DOCUMENT TIER 2 CHAPTER 4 REACTOR," APR1400-K-X-FS-14002-NP REVISION 0, KEPCO and KHNP, 2014.
- [25] Y. S. Ban, "Development of Advanced Leakage Feedback Method for Two-step Core Analyses," PhD Thesis, Seoul National University, 2018.
- [26] S. Jeon, N. Choi and H. G. Joo, "Feasibility of Fast Pinwise Core Simulation Using GPUs," in *Transactions of the KNS Virtual Autumn Meeting*, 2020.
- [27] M. Tatsumi and A. Yamamoto, "A Study on Effects of Pin Cell Homogenization in an Actual Reactor Core Geometry," in *Proceedings of PHYSOR2000*, Pittsburgh, Pennsylvania, USA, 2000.
- [28] K. Tada, A. Yamamoto, Y. Yamane and Y. Kitamura, "Applicability of the Diffusion and Simplified P3 Theories for Pin-by-Pin Geometry of BWR," *Journal of Nuclear Science and Technology*, vol. 45, no. 10, pp. 997-1008, 2008.
- [29] D. Litskevich and B. Merk, "SP3 Solution versus Diffusion Solution in Pin-by-Pin Calculations and Conclusions Concerning Advanced Methods," *Journal of Computational and Theoretical Transport*, vol. 43, pp. 214-239, 2014.
- [30] H. Hong and H. G. Joo, "Thorough analyses and resolution of various errors

- in pin-homogenized multigroup core calculation," *Annals of Nuclear Energy*, vol. 163, 2021.
- [31] T. Kozlowski and T. J. Downar, "The PWR MOX/UO₂ Core Transient Benchmark, Final Report," NEA/NSC/DOC(2006)20, 2006.
- [32] D. Bernard, A. Calame and J-M. Palau, "LWR-UOX Doppler Reactivity Coefficient: Best Estimate Plus (nuclear and atomic sources of) Uncertainties," in *Proceedings of M&C2017*, Jeju, Korea, 2017.
- [33] G. Grandi, K. Smith, Z. Xu and J. Rhodes, "Effect of CASMO-5 cross-section data and Doppler temperature definitions on LWR reactivity initiated accidents," in *Proceedings of PHYSOR2010*, Pittsburgh, Pennsylvania, USA, 2010.
- [34] M. Hursin, T. J. Downar, J. I. Yoon and H. G. Joo, "Assessment of Assembly Homogenized Two-step Core Dynamic Calculations using Direct Whole Core Transport Solutions," *Annals of Nuclear Energy*, vol. 87, pp. 356-365, 2016.
- [35] C. Beckert and U. Grundmann, "Development and verification of a nodal approach for solving the multigroup SP3 equations," *Annals of Nuclear Energy*, vol. 35, pp. 75-86, 2008.
- [36] T. Fujita, T. Endo and A. Yamamoto, "A new technique for spectral interference correction on pin-by-pin BWR core analysis," *Journal of Nuclear Science and Technology*, vol. 51, no. 6, pp. 783-797, 2014.
- [37] H. Yu, J. Kim and Y. Kim, "Pinwise Diffusion Solution of Partially MOX-Loaded PWRs with the GPS (GET PLUS SPH) Method," *Nuclear Science and Engineering*, vol. 193, no. 11, pp. 1238-1254, 2019.
- [38] N. Choi, H. Park, H. G. Lee, S. Jae, S. Jeon and H. G. Joo, "Recent capability and performance enhancements of the whole-core transport code nTRACER," in *Proceedings of PHYSOR2020*, Cambridge, United Kingdom, 2020.
- [39] "Hierarchical Data Format," Wikipedia, [Online]. Available: https://en.wikipedia.org/wiki/Hierarchical_Data_Format. [Accessed 20 6 2021].
- [40] 홍현식, "봉단위 노심 계산을 위한 균정수 생산 방법론," SNURPL-TR-057(19), 서울대학교 원자로물리연구실, 2019.
- [41] U. Grundmann and S. Mittag, "Super-homogenisation factors in pinwise calculations by the reactor dynamics code DYN3D," *Annals of Nuclear Energy*, vol. 38, pp. 2111-2119, 2011.
- [42] G. Chiba, M. Tsuji, K. Sugiyama and T. Narabayashi, "A note on application of superhomogénéisation factors to integro-differential neutron transport equations," *Journal of Nuclear Science and Technology*, vol. 49, no. 2, pp. 272-280, 2012.
- [43] A. T. Godfrey, "VERA Core Physics Benchmark Progression Problem Specifications, Revision 4," CASL-U-2012-0131-003, CASL, 2014.
- [44] S. Choi, K. S. Smith, H. Kim, T. Tak and D. Lee, "On the diffusion coefficient calculation in two-step light water reactor core analysis," *Journal of Nuclear Science and Technology*, vol. 54, no. 6, pp. 705-715, 2017.
- [45] H. Hong and H. G. Joo, "Analysis of Errors from Various Origins in Pin-Homogenized Multi-Group Calculation," in *KNS 2020 Spring*, Jeju, Korea,

2020.

- [46] T. Fujita, K. Tada, T. Endo, A. Yamamoto, S. Kosaka, G. Hirano and K. Nozaki, "An optimization approach to establish an appropriate energy group structure for BWR pin-by-pin core analysis," *Journal of Nuclear Science and Technology*, vol. 49, no. 7, pp. 689-707, 2012.
- [47] A. Hébert, "High order diamond differencing schemes," *Annals of Nuclear Energy*, vol. 33, pp. 1479-1488, 2006.
- [48] N. Choi, "Development of GPU-Based Deterministic and Probabilistic Direct Whole-core Calculation Systems," PhD Thesis, Seoul National University, 2021.
- [49] R. Chambon, "Specifications and User Guide for NAP: module in DRAGON/DONJON VERSION 5 (Pin Power Reconstruction module)," IGE-345, Ecole Polytechnique de Montreal, 2014.
- [50] T. Downar, Y. Xu, V. Seker and N. Hudson, "PARCS v3.0 U.S. NRC Core Neutronics Simulator Theory Manual," UM-NERS-09-0001, USA, 2009.
- [51] J. I. Yoon and H. G. Joo, "Two-Level Coarse Mesh Finite Difference Formulation with Multigroup Source Expansion Nodal Kernels," *Journal of Nuclear Science and Technology*, vol. 45, no. 7, pp. 668-682, 2008.
- [52] H. J. Jeong, "Alternating Direction One-Dimensional Source Expansion Nodal Method for Whole Core Simplified P3 Calculation," Master Thesis, Seoul National University, 2013.
- [53] Y. S. Ban and H. G. Joo, "The Rationale of Leakage Parameters adopted in Leakage Feedback Method," in *KNS 2018 Autumn*, Yeosu, Korea, 2018.
- [54] H. Hong and H. G. Joo, "Leakage Feedback Method for Pin-by-Pin Core Calculation," in *KNS 2019 Spring*, Jeju, Korea, 2019.
- [55] T. Fujita, T. Endo and A. Yamamoto, "Application of correction technique using leakage index combined with SPH or discontinuity factors for energy collapsing on pin-by-pin BWR core analysis," *Journal of Nuclear Science and Technology*, vol. 52, no. 3, pp. 355-370, 2015.
- [56] R. Sanchez, "Assembly homogenization techniques for core calculations," *Progress in Nuclear Energy*, vol. 51, pp. 14-31, 2009.

초 록

집합체 단위 소수군정수를 이용하는 전통적인 2단계 노심 계산 방법은 상용 노심 핵설계에 널리 사용되어 왔다. 해당 방법은 계산 자원 소요가 극히 적은 장점이 있으나, 집합체 단위 소수군정수가 실제 노심 환경을 정확히 반영하기 어려우므로 비균질성이 높은 노심에서 반응도 및 출력 분포에 상당한 오차를 보인다. 이에 선행 연구에서 Yoon은 봉단위 다군군정수를 채택하고 봉단위 균질화 및 확산법 기반 소격 격자 유한차분(FDM) 계산의 오차를 SPH인자로 보정하여 계산 정확도를 성공적으로 향상시켰다. 한편 Cho는 단순화된 P_3 (SP_3) 이론 기반의 FDM 해법을 도입함으로써 봉단위 SP_3 노심 계산의 가능성을 보였다.

선행연구에 사용된 확산법 및 SP_3 이론 기반 FDM 해법은 일반적 노심 문제에 대해서는 계산 정확도가 높으나, 비균질성이 높은 3.5세대 상용 노심 및 혼합산화물(MOX) 연료가 장전된 소형 노심 등에서는 오차가 현저하다. 이에 본 연구에서는 봉단위 다군 노심 계산에서의 주요 오차 요인을 체계적으로 분석함으로써 최적의 중성자속 해법을 선정하고, 봉단위 다군군정수에 누설 보정을 적용함으로써 고신뢰도 2단계 봉단위 노심 계산을 실현하는 것을 목표로 설정하였다.

본 연구에서는 우선 봉단위 균질화 된 군정수를 단일 집합체 기반 SPH 인자와 함께 노심 계산에 사용함으로써 인한 오차를 다양한 노심 벤치마크 문제를 활용하여 분석하였다. 이는 봉단위 2단계 계산에서 SPH인자가 필수적임을 확인하고, 적절한 저차 수송 근사와 공간 차분 방법을 적용하면 단일 집합체 기반 SPH인자를 노심에 사용함에 기인하는 오차가 감소함을 보이기 위함이다. 이로써 첫째, 핀셀 내부 구조 정보의 손실로 인한 반응률 오차, 즉 균질화 오차가 전체 군정수 오차 가운데 영향이 가장 크며 이는 SPH인자로 보정 가능함을 확인하였다. 다음으로 단순화된 P_N (SP_N) 및 S_N 수송 근사 방법을 다양한 공간 차분 방법과 조합한

중성자속 해법을 시험하였다. 이로써 확산법 기반 계산 결과의 양호한 겹보기 오차는 현저한 오차 상쇄에서 비롯된 것이며, SP_5 계산 결과는 SP_3 결과와 유의미한 차이가 없고, S_N 계산 결과는 단일 집합체 기반 SPH인자가 고 에너지 영역에서 노심 환경을 적절히 반영하지 못하여 오차가 극심함을 확인하였다. 이에 따라 본 연구에서는 SP_3 이론 기반 선원확장노달법(SENM)을 최적의 해법으로 선정했다. 비균질성이 현저한 KAIST 1A ARO 문제에 대한 8군 계산에서, 단일 집합체 기반 SPH인자로 인한 붕출력 최대 오차는 SP_3 SENM이 1.1%로, 확산법 및 SP_3 이론 기반 FDM 계산의 4.6%, 8.5%에 비해 현저히 낮았다.

또한 단일 집합체 기반 봉단위 다군 균정수의 스펙트럴 오차에 대해서도 분석을 수행하였다. 스펙트럴 오차는 봉단위 균정수 생산 시의 집합체 경계 조건이 실제 노심 환경과 불일치함에서 기인하는 경계조건 오차와, 균축약에 사용된 중성자 스펙트럼과 실제 노심 스펙트럼의 차이로 인한 균축약 오차에 기인한다. 에너지군 수에 따른 민감도 검사 결과 약 8개 에너지군을 사용하면 스펙트럼 오차에 의한 붕출력 오차의 제공 평균을 1.0% 미만으로 억제 가능하다. 그러나 대단히 비균질한 노심에서는 8군 이상을 사용해도 붕출력 최대 오차가 현저하여 봉단위 누설 궤환 보정법(LFM)의 도입이 결정됐다. LFM은 균정수를 누설 인자에 대해 함수화하는 방법으로, 스펙트럴 오차가 누설 효과에 기인함을 근거로 한다.

SP_3 SENM 해법의 정확도와 봉단위 LFM의 적용성은 단일 집합체 기반 봉단위 균정수와 SPH인자를 사용한 2단계 노심 계산으로 검증하였다. nTRACER 직접 전노심 계산 결과를 참조해로 활용했으며, 동일 코드를 균정수 생산에 사용함으로써 코드 간 비교의 일관성을 유지했다. 확산법 및 SP_3 기반 소격 격자 FDM 계산에 SPHINCS 코드를, SENM 계산에 VANGARD 코드를 사용했다. SP_3 SENM 계산 결과는 참조해와 잘 일치했으며 LFM을 적용함으로써 정확도가 더 향상되었다. KAIST 1A ARO 문제에서, 확산법 및 SP_3 기반 FDM 계산은 8군 균정수를 사용하여도 각각 48, 74 pcm의 반응도 오차와 11.4%, 14.8%의 붕출력 최대 오차를

보인 반면, SP₃ SENM의 오차는 74 pcm, 7.3%로, LFM을 적용하면 이는 9 pcm, 1.1%로 감소했다. 반면 FDM 해법은 그 정확도가 낮기 때문에 LFM 적용에 따른 오차 감소가 상대적으로 적었다. 한편 3.5세대 상용 노심인 AP1000 PWR 문제를 이용, 3차원 고온전출력 노심 연소 등의 다양한 조건에서 LFM의 적용성을 입증했다. SP₃ SENM 해법과 LFM의 실용성도 확인했는데, 제어봉이 부분 삽입된 고온영출력 3차원 노심에 대하여 20개 CPU 코어로 8군 계산을 수행하면 반경 방향 봉출력 최대 오차와 총 계산 시간은 확산법 기반 FDM이 1.7%, 66초인 데 비해 SP₃ SENM은 LFM 적용 전 1.8%, 120초, 적용 후 0.7%, 159초로, 정확한 노심 계산에 소요되는 자원은 과도하지 않다. 아울러 SP₃ SENM 해법의 계산 시간과 관련, VANGARD 코드에 대한 선행연구에서는 노달 계산의 병렬화가 용이함에 착안하여 상용 GPU 기반 가속으로 약 20배 이상의 속도향상을 달성한 바 있음을 주지할 필요가 있다.

본 연구를 통해 SP₃ SENM 해법과 봉단위 LFM을 적용함으로써 단일 집합체 기반으로 생산된 봉단위 균정수와 SPH인자를 이용하더라도 전 노심 직접 계산 참조해를 정확히 재생산할 수 있음을 확인했다. 최적의 중성자속 해법과 누설 보정에 기반한 2단계 노심 계산은, 오차 상쇄에 의존하지 않음으로써 노심의 비균질성이 높더라도 정확한 해를 생산할 수 있다는 점에서 선행 연구와 차별화되는 가치가 있다. 이러한 성과는 VANGARD 코드 개발에 충실히 반영되어 고신뢰도 노심 계산 능력의 바탕이 되었다. 또한 신형 노심 설계 및 안전 규제 강화 등으로 인해 고신뢰도 2단계 노심 계산에 대한 수요가 증가하고 있는 바, 본 연구는 봉단위 코드 사용자 및 개발자들을 위한 참고자료가 될 것이다.

주요어 : VANGARD, SP_N, 선원확장노달법, 봉단위 2단계 노심 해석, 봉단위 누설 계환 보정

학번 : 2015-22949